EZH2-H3K27me3 mediated KRT14 upregulation promotes TNBC peritoneal metastasis

Ayushi Verma[1], Akhilesh Singh[1], Manish Pratap Singh[1], Mushtaq Ahmad Nengroo[1], Krishan Kumar Saini[1,2], Saumya Ranjan Satrusal[1,2], Muqtada Ali Khan[1], Priyank Chaturvedi[1], Abhipsa Sinha[1], Sanjeev Meena[1], Anup Kumar Singh[1], Dipak Datta[1,2,*]

Authors' Affiliation:
[1]Division of Cancer Biology, CSIR-Central Drug Research Institute (CDRI), Lucknow 226031, India
[2]Academy of Scientific and Innovative Research, Ghaziabad, Uttar Pradesh, 201002, India.

Short Title: *H3K27me3 promotes TNBC metastasis*

Key Words: EZH2, H3K27me3, Cytokeratin 14, TNBC, Metastasis

* Corresponding Author:
Dipak Datta, Division of Cancer Biology, CSIR-CDRI, B.S. 10/1, Sector 10, Jankipuram Extension, Sitapur Road, Lucknow-226031, India, Tel: 91-522-2772450 (Extn-4347/48), Fax: 91-522-2771941, E-mail: dipak.datta@cdri.res.in

Abstract:

Triple-Negative Breast Cancer (TNBC) has a poor prognosis and adverse clinical outcomes among all breast cancer subtypes as there is no available targeted therapy. Overexpression of Enhancer of zeste homolog 2 (EZH2) has been shown to correlate with TNBC's poor prognosis, but the contribution of EZH2 catalytic (H3K27me3) versus non-catalytic EZH2 (NC-EZH2) function in TNBC progression remains elusive. We reveal that selective hyper-activation of functional EZH2 (H3K27me3) over NC-EZH2 alters TNBC metastatic landscape and fosters its peritoneal metastasis, particularly splenic. Instead of H3K27me3-mediated repression of gene expression; here, it promotes *KRT14* transcription by attenuating binding of repressor Sp1 to its promoter. Further, KRT14 loss significantly reduces TNBC migration, invasion, and peritoneal metastasis. Consistently, human TNBC metastasis displays positive correlation between H3K27me3 and KRT14 levels. Finally, EZH2 knockdown or H3K27me3 inhibition by EPZ6438 reduces TNBC peritoneal metastasis. Altogether, our preclinical findings suggest a rationale for targeting TNBC with EZH2 inhibitors.

Introduction

According to global cancer statistics, breast cancer is the most common malignancy worldwide in women, having 2.09 million new cases diagnosed in 2018 with 0.6 million deaths [1]. Among different breast cancer subtypes, basal-like breast cancer is often clinically defined as Triple-Negative Breast Cancer (TNBC), which lacks immunohistochemistry (IHC) expression of Estrogen receptor (ER), progesterone receptor (PR), and human epidermal growth factor receptor 2 (her2/neu) according to College of American Pathologist (CAP)/ASCO guidelines [2]. It involves patients of young age and is associated with high grade, poor prognosis tumors [3]. TNBC poses a serious threat to clinicians due to the enormous heterogeneity of the disease and the absence of well-established molecular targets [4]. Indeed, the 90% mortality of breast cancer, including TNBC, is associated with metastasis [5, 6, 7, 8]. Underpinning the molecular cues for TNBC metastasis and its therapeutic intervention are the hotspots of current cancer research. The concept of epigenetic reprogramming is admired as a driving force for distant organ metastasis. Importantly, Breast cancer molecular subtypes have been identified with unique chromatin architecture with diverse methylation patterns [9, 10]. However, how epigenetic mechanisms exclusively regulate subtype-specific distinct transcriptional nexus still remains elusive. Epigenetic modulator Enhancer of Zeste homolog 2 (EZH2), a catalytic subunit of Polycomb Repressive Complex 2 (PRC2), promotes target genes suppression by tri-methylation of lysine 27 of histone H3 (H3K27me3) [11]. Previously, we have shown the classical gene silencing function of EZH2 where death receptors are epigenetically suppressed in cancer stem cells [12]. Notably, aberrant EZH2 expression has been associated with diverse cancers concerning both oncogenic and tumor suppression functions [13]. Besides its canonical function as a transcriptional repressor, EZH2 protein has recently been shown to perform H3K27me3 independent functions [14, 15, 16, 17, 18]. In support of non-canonical functions, studies have shown a hidden, partially disordered transactivation domain (TAD) in EZH2, which directly binds to the transcriptional coactivator p300 and promotes oncogenesis [17, 18]. However, Mittal's group has performed the bioinformatics analysis of epigenetic-associated genes in breast cancer patients, which characterized overexpression of EZH2 catalytic function as a predominant carrier in TNBC metastasis with poor overall survival [19].

Expression of basal cytokeratins like CK5/6, CK14 and CK17 are hallmark features of TNBC [4]. Interestingly, cytokeratins serve more than mere epithelial cell markers and several recent studies have provided evidence for active keratin involvement in cancer cell invasion and metastasis [20]. *Kevin et al.,* in their diligent studies, showed that polyclonal breast cancer metastases arise from the collective dissemination of keratin 14-expressing tumor cell clusters [21]. Regulation of cytokeratin expression and their functional consequences, particularly in basal-like breast cancer metastasis, is not precise yet.

In this work, we show the differential role of EZH2 catalytic (elevated H3K27me3 or H3K27me3High) versus non-catalytic EZH2 (NC-EZH2) function in the context of TNBC progression. Interestingly, we detect that elevated H3K27me3 but not its NC-EZH2 protein overexpression results in robust increase of TNBC peritoneal metastasis. Transcriptome analysis of H3K27me3High TNBC cells lead to the discovery that *KRT14* is a target of H3K27me3. Instead of H3K27me3 mediated classical transcriptional repression, we find H3K27me3 promotes *KRT14* gene expression by altering the recruitment pattern of its transcription factor Sp1. Our sequential *in-vivo* imaging experiments clearly demonstrate that KRT14 is a critical regulator of TNBC splenic metastasis and loss of KRT14 even in H3K27me3High background compromises TNBC peritoneal metastasis. Further, we explore the clinical relevance of our finding in the Breast Cancer (Yau 2010) database where ER, PR, and HER2 negative basal-like breast cancer or TNBC selectively displays a positive correlation between EZH2 and KRT14 expression and H3K27me3 and KRT14 expression are found to be significantly upregulated in human TNBC metastasis as compared to their respective primary tumors. Finally, EZH2 functional loss, either by knockdown

or the treatment of H3K27me3 selective inhibitor EPZ6438, significantly reduces TNBC migration, invasion *in-vitro,* and peritoneal metastasis *in vivo*. In summary, our data indicate that the trimethylation function of EZH2 may drive peritoneal metastasis of TNBC, and targeting the methyltransferase activity of EZH2 could be a good option to prevent TNBC metastasis.

Results

EZH2 functional activation but not its protein overexpression promotes TNBC metastasis

Our studies and recent literature suggest that EZH2 plays a critical role in TNBC pathophysiology [19, 22, 23]. TNBC is a highly heterogeneous group of cancers, where intrinsic subtype analysis suggests approximately 80% of TNBC belongs to basal-like category [4, 24]. The basal-like or basaloid TNBC (B-TNBC) is one of the most aggressive, therapy-resistant, and metastatic tumors [25]. Therefore, we focus our entire studies on basal-like TNBC subtype. Here, we sought to dissect the role of NC-EZH2 versus H3K27me3 in TNBC progression. We have established a 4T-1based animal model that closely mimics basal-like TNBC progression under a preclinical setting [26]. To explore the individual role of NC-EZH2 versus H3K27me3 function, we made 4T-1 stable cells either overexpressing EZH2 catalytically inactive (–ΔSET) or catalytically hyperactive EZH2 (Y641-F) protein (Figure 1A and 1B). Following subcutaneous and orthotopic inoculation of control and genetically modified 4T1 cells into mice, we observe that Y641-F tumor-bearing mice have significantly smaller tumors compared to control tumor-bearing mice, while EZH2 (–ΔSET) tumor-bearing mice have no significant change in the tumor growth compared to control tumor-bearing group (Figure 1C and 1D and Supplementary Figure 1) however, Y641-F tumor bearing mice lost marked body weight compared to control, during tumor progression (Figure 1E). Significant body weight loss in Y641-F tumour-bearing mice prompted us to check the metastasis status of the particular group. To understand the metastatic potential of individual group of cells, we adapted the same system but here we used Luc-tagged 4T-1 cells and investigated their metastatic progression through sequential live animal imaging. As shown in Figure 1F (top and bottom panels) and 1G, Y641-F tumour-bearing mice demonstrate a substantial increase in metastasis compared to control. Therefore, accelerated metastasis may be the reason for the marked weight loss of Y641-F tumour-bearing mice. Altogether, *in-vivo* studies established that H3K27me3 but not NC-EZH2 protein regulates TNBC metastasis. Increased
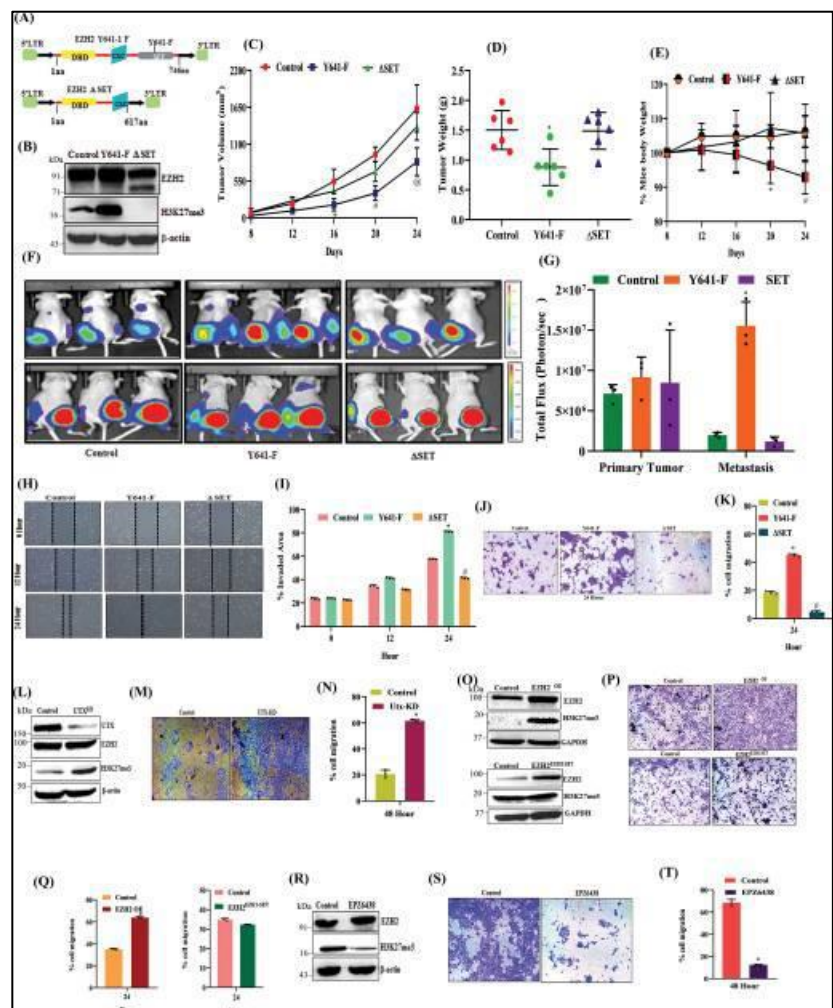

Figure 1

metastasis in Y641-F cells encouraged us to explore further the impact of H3K27me3 on TNBC cell migration and invasion. Here, we performed wound healing and trans-well chamber assay to assess migration and invasion, respectively. In the wound healing assay (Figure 1H and 1I), we detect Y641-F mutant cells have clear higher migratory potential as these cells are found to close the wound more rapidly than wild-type cells. Similarly, in trans-well chamber assay, Y641-F cells also show higher invasive capabilities than that of wild-type cells (Figure 1J and 1K). To further confirm H3K27me3 selective induction of TNBC migration, we made UTX or KDM6A (H3K27me3 specific demethylase[27]) knock down stable cells that display a selective increase of H3K27me3 without altering EZH2 levels as compared to control cells (Figure 1L). When we assessed the migration capabilities of control and UTX KD cells by invasion assay, we observed that UTX KD cells migrate faster than control cells, again confirming H3K27me3 dependent induction of TNBC migration (Figure 1M and 1N). To further rule out the contribution of EZH2 protein in modulating TNBC migration, we took two different strategies. Several studies have shown that the EZH1SET domain has weak enzymatic activity than the EZH2SET domain [28]. We next examined if the domain-swap approach could be useful to analyse the findings linked with NC EZH2[29]. In our first strategy, we made stable TNBC cells having either wild-type EZH2 overexpression or EZH2 overexpression containing the SET domain of EZH1 (hereafter referred to as EZH2$^{EZH1-SET}$) and evaluated their level of EZH2, H3K27me3, and their respective migration capabilities. As shown in Figure 1O, cells bearing EZH2$^{EZH1-SET}$ construct show overexpression of EZH2 at the protein level but H3K27me3 remains unchanged as compared to control and exhibits no change in invasion capabilities of TNBC whereas WT EZH2 overexpression results in increased invasion (Figure 1P and 1Q) suggesting NC EZH2 has no role in TNBC migration induction. In our second strategy, we made use of the FDA approved drug tazemetostat (EPZ6438), a pharmacological inhibitor of EZH2 which selectively inhibits H3K27me3 activity of EZH2 without altering its expression at protein level (Figure 1R). Before assessing its impact on TNBC migration, we checked its cytotoxic impact on TNBC cells and observed that it does not pose any cytotoxic impact on TNBC cells, tested up to 40μM concentration as determined by MTS and colony formation assay (Supplementary Figure 2). Next, we sought to determine the effect of EPZ6438 on TNBC invasion and observed that the selective inhibition of H3K27me3 by EPZ6438 at even a 10 μM dose robustly inhibited TNBC invasion compared to control (Figure 1S and 1T). Altogether, our extensive *in vitro* and *in vivo* experiments clearly suggest that H3K27me3 promotes TNBC migration, invasion, and metastasis.

Catalytically hyperactive EZH2 (elevated H3K27me3) alters the metastatic landscape of TNBC

To further validate the correlation between hyperactivation of H3K27me3 with rapid TNBC metastasis, we adapted three different strategies as described in (Figure 2A). Interestingly, in our uniquely designed three (mix single flank mammary fat pad, mix tail vein, and individual double flank mammary fat pad) strategies, we observe that TNBC metastasis is robustly augmented upon H3K27me3 elevation (Figure 2B and 2C) compared to control. Next, we sought to determine the TNBC metastatic pattern under the influence of increased H3K27me3. Fluorescence imaging analysis of harvested organs from double flank mammary fat pad inoculated (Control versus Y641-F) mice exhibit that control cells tend to metastasize mainly into the lungs, whereas, Y641-F cells tend to significantly metastasize into the spleen and liver (Figure 2D). Representative fluorescent microscopic images and FACS analysis of single cells harvested from different metastatic organs of experimental mice clearly demonstrate the striking alteration of the metastatic pattern observed with induction of H3K27me3 (Figure 2E-2G). To further validate our results *in situ*, we performed H&E staining of Lung, Liver, and Spleen tissues harvested from control and Y641-F tumor-bearing mice and observed that the majority of metastatic foci are localized within the lung of control tumor-bearing mice whereas Y641-F tumor-bearing mice

display predominant liver and spleen metastasis (Figure 2H). Further, we collected peritoneal fluid of both control and Y641-F tumor-bearing mice and cultured it for 48 hours in the presence of 6TG and observed 4T1 colonies only in the case of peritoneal fluid isolated from Y641-F tumor-bearing mice (Figure 2I). Collectively, these series of *in vivo* studies strongly suggest that the enhanced global trimethylation has a significant impact on TNBC peritoneal metastasis.

Transcriptome analysis identified *KRT14* as a target of H3K27me3 in TNBC

Next, we sought to find the correlation between H3K27me3 function and TNBC metastasis at the basal state. We orthotopically inoculated WT 4T-1- Luc cells in the mammary fat pad of female nude mice (Figure 3A). We isolated metastatic cells from different organs following mammary fat pad inoculation and after EZH2 expression analysis; we observed that splenic metastatic cells have the highest expression of global
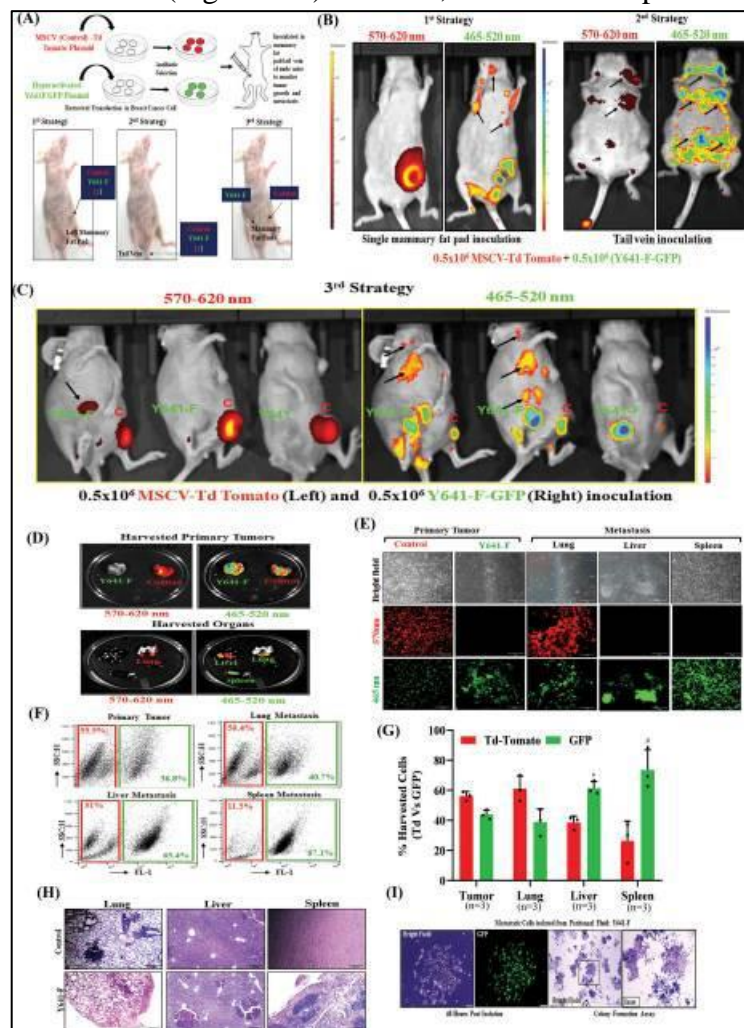

Figure 2

H3K27me3 compared to cells isolated from primary tumors, followed by liver and lung (Figure 3B). Notably, the splenic metastatic cells matched the phenotype with Y641-F cells at the basal state. Further, we inoculated splenic isolated metastatic and primary tumor cells into the mammary fat pad again and evaluated the TNBC progression. As shown in Figure 3C (left panel), live animal imaging data clearly establishes that splenic metastatic cell inoculation results in a visible increase of TNBC peritoneal metastasis compared to the respective control (Figure 3C, right panel). Further, splenic metastatic cell tumour bearing mice die significantly earlier than the control (Figure 3D).

H3K27me3-driven robust changes in TNBC metastatic signature encourage us to identify the mechanistic insight behind the phenotype. We perform differential Transcriptome analysis in control and Y641-F cells to explore this idea. In our transcriptome analysis, a total of 21044 common genes were mapped and found to be differentially expressed in control and Y641-F cells. Volcano plot analysis of the differentially expressed genes (DEGs) with (Log_2FC +1, -1 and $p > 0.05$) criteria revealed 2142 significant DEGs in the Y641-F group compared to the control. Out of 2142 DEGs, 805 genes were significantly upregulated, and 1337 genes were significantly down-regulated (Figure 3E). Gene Set Enrichment Analysis (GSEA) was performed to evaluate the characteristic dynamic pattern between control and Y641-F cells. In gene marker section of the GSEA, the heat map was generated for the top 50 features of each phenotype (control vs Y641-F) (Figure 3F). The heat map displayed 100 top ranked genes (50 top ranked high expression and 50 top ranked low expression) differentially expressed between control and Y641-

F. Correlating with our observed phenotypes *in vitro* and *in vivo*, these top 100 ranked genes were explored in literature to understand their role in cancer cell migration and metastasis. Based on the literature, a total 16 genes were selected according to their association with cell migration and metastasis (Supplementary Table 1). A heat map of these 16 genes were plotted to show the differential expression in control and Y641-F phenotype (Figure 3G). Next, we individually validated the differential expression of the selected genes by the qRT-PCR between control and Y641-F cells. Of note, the expression of *NIFK, ADAMTS1, CCN2, JAG1, SEMA3C, TM4SF1, CYP1B1, KRT14,* and *KRT16* were found to be upregulated (Figure 3H, Left panel), whereas, the expression of *NCAM1, AQP1, BNIP3, CBS, and NDRG1* were down-regulated in Y641-F cells as compared to control cells (Figure 3H, Right panel). Next, to understand the contribution of these
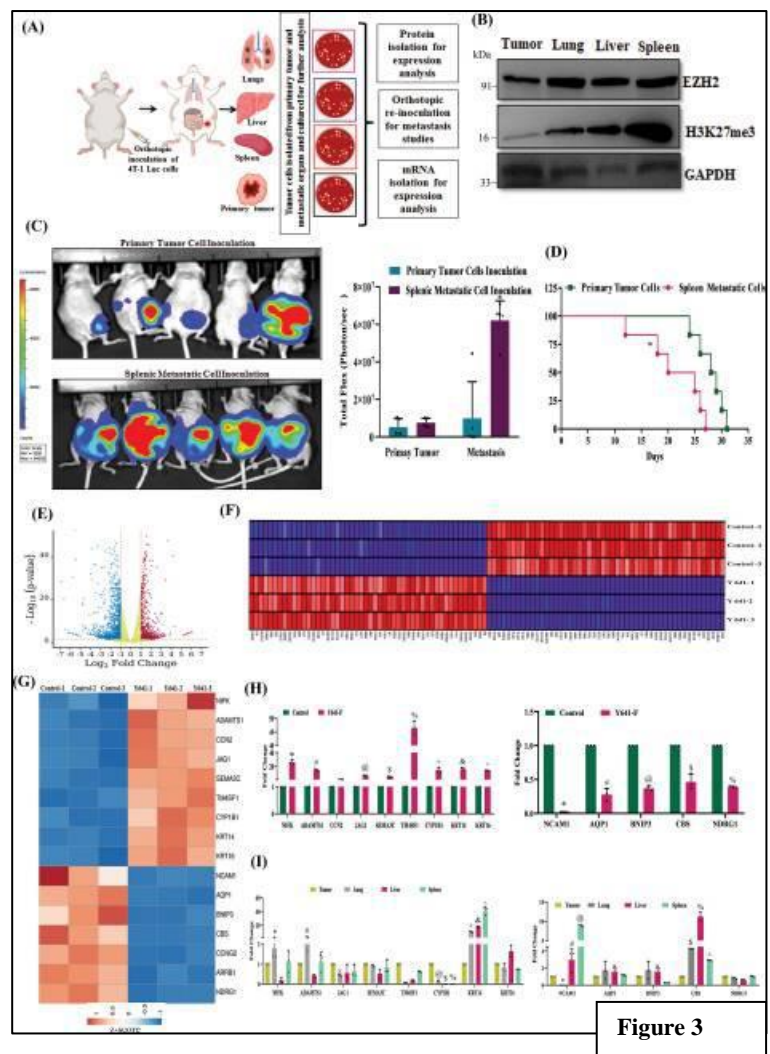

Figure 3

changes in ascertaining peritoneal metastasis in TNBC at basal state (scheme represented in Figure 3A), we examined the mRNA expression of the validated up and downregulated genes in the metastatic cells isolated from the primary tumor, lungs, liver, and spleen. After extensive validation, *KRT14* was found to be the markedly upregulated gene in the cells isolated from lung, liver, and splenic metastasis as compared to primary tumor cells, though the highest robustness was observed in the case of splenic metastasis (Figure 3I, left and right panels). Our previous result suggested that the global H3K27me3 level was robustly high in the metastatic cells isolated from the spleen compared to primary tumor cells (Figure 3B). Similarly, *KRT14* is the only robustly upregulated gene in Y641-F cells compared to control cells *in vitro* (Figure 3H, left panel) and primary tumor versus splenic metastatic cells *in vivo*, following orthotopic inoculation of wild-type cells (Figure 3I, left panel). However, except for *KRT14*, none of the other genes passed through this validation process.

H3K27me3 modulates *KRT14* expression at both the mRNA and protein levels

Seminal work by Lehman *et al.,* demonstrated the importance of *KRT* gene family in classifying TNBC, including *KRT14*[4]. Here, we sought to validate the impact of H3K27me3 on *KRT14* expression regulation. In 4T1 cells, following overexpression of either wild type EZH2 or Y641-F mutant EZH2, we found that KRT14 expression is significantly upregulated in EZH2[OE] and Y641-F cells as compared to controls; however, in EZH2[EZH1 SET] cells, we found no significant change in KRT14 expression at the protein level (Figure 4A-4C) confirming that the H3K27me3 function of EZH2 is one of the crucial factors for *KRT14* upregulation. Moreover, Tazemetostat (EPZ6438) treatment in both control and Y641-F cells resulted in a observable reduction in

KRT14 expression at both the mRNA and protein levels (Figure 4D-4E). Inducible EZH2 gain of function in HCC1806 results in an increase in KRT14 level (Figure 4 F), while functional EZH2 inhibition by EPZ6438 in HCC1806 cells markedly down-regulates the *KRT14* mRNA expression (Figure 4G). Further, we extend our validation experiments in two (HCC1806 and MDAMB468) different basal human TNBC cell lines. Subsequently, we found that the KRT14 protein expression was significantly down-regulated in HCC1806 and MDAMB468 by EPZ6438 treatment. (Figure 4H). The down-regulation of KRT14 was also observed in the EPZ6438 treated HCC1806 cells by confocal microscopy (Figure 3I).
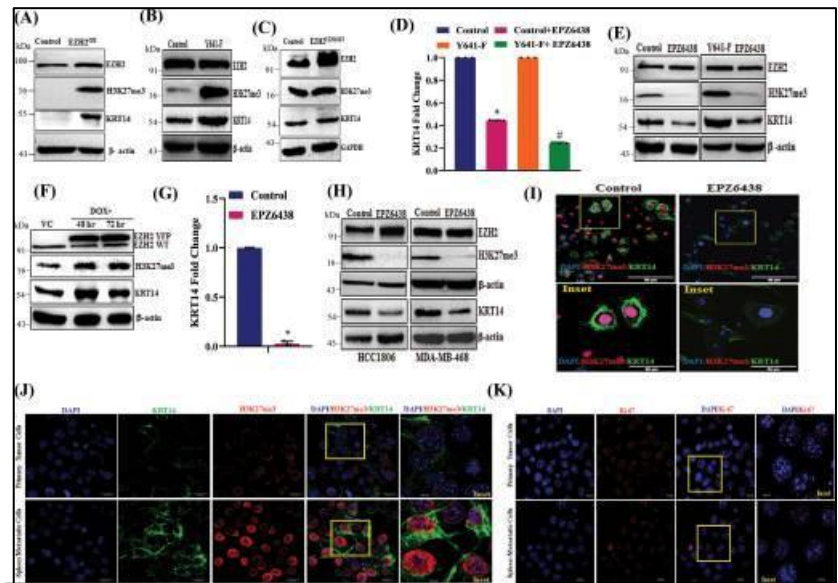

Figure 4

After extensive *in vitro* validation, we sought to determine the correlation between H3K27me3 and KRT14 expression *in vivo* by confocal microscopy in isolated primary tumor cells versus splenic metastatic cells. As shown in Figure 4J, the expression of both H3K27me3 and KRT14 increases in splenic metastatic cells compared to primary tumor cells, confirming the positive correlation between H3K27me3 and KRT14 in TNBC splenic metastasis in a preclinical animal model. However, we did not find any significant alteration in the expression of the proliferation marker (Ki67) between primary tumor cells and splenic metastatic cells, suggesting that an increase in H3K27me3 level only affects TNBC migration but not proliferation (Figure 4K). These results strongly put forward that EZH2 methyltransferase activity enhances KRT14 expression in TNBC cells *in vitro* and *in vivo*.

H3K27me3 enrichment in the *KRT14* promoter is associated with its active transcription

Classically, H3K27me3 mark acts as a transcriptional repressor [30]. However, our data undeniably indicate that it positively regulates KRT14 expression, particularly in basal-like TNBC subtype. To investigate whether H3K27me3 marks directly occupy the *KRT14* promoter that leads to transcription activation, we perform the chromatin immunoprecipitation (ChIP) assay in 4T-1 and HCC1806 cells by using H3K27me3 and P-S5- RNA polymerase II specific antibody. To delineate the enrichment of H3K27me3 marks in the *KRT14* promoter, we design the walking primers in the sliding window of -3000 bases upstream and +2500 bases downstream of Transcription Start Site (TSS) by utilizing the Eukaryotic Promoter Database based on the *KRT14* chromosomal location (Figure 5A). The q-PCR analysis in the walking primer experiments reveals the strong enrichment of H3K27me3 marks upstream of -0.2 kb and -0.5 Kb region in mouse 4T-1 cells, while in human HCC1806 cells, the enrichment of H3K27me3 marks is selectively identified only in -0.2 kb region (Figure 5B and 5C). To determine whether H3K27me3 enrichment in the *KRT14* promoter is associated with transcription activation or repression, we perform the ChIP q-PCR for the transcription initiation specific RNA Pol-II C-terminal domain Ser-5 phosphorylation. Interestingly, the recruitment of p-Pol-II-S5 on the -0.2 kb region of the *KRT14* promoter is observed, indicating the transcriptional activation in both 4T-1 and HCC1806 cells (Figure 5B and 5C). To further confirm the H3K27me3 mediated transcriptional activation of *KRT14*, we compare the H3K27me3 enrichment in the control and

Y641-F cells by ChIP-qPCR. Most likely, the robust H3k27me3 and p-Pol-II-S5 enrichment were found in Y641-F cells in comparison to the control cells (Figure 5D and 5E). Reduction of both H3K27me3 marks and p-Pol-II-S5 is identified in the *KRT14* promoter following EPZ6438 (10μM) treatment in HCC1806 cells, further establishing the authenticity of the earlier observations (Figure 5F). Though the H3K27me3 mark classically acts as a repressor, surprisingly, we find in our case, it promotes *KRT14* gene transcription. Besides its catalytic (H3K27me3) function, EZH2 protein has been shown to transactivate genes in multiple elegant studies [17, 18]. Therefore, we explored the EZH2 recruitment in the *KRT14* gene by utilizing the EZH2 antibody to perform ChIP assay followed by ChIP-qPCR. However, we did not find any EZH2 enrichment in the *KRT14* promoter with respect to H3K27me3 enriched sites that further confirmed the specific involvement of EZH2 catalytic product (H3K27me3) but not EZH2 protein for the positive transcriptional regulation of *KRT14*

Figure 5
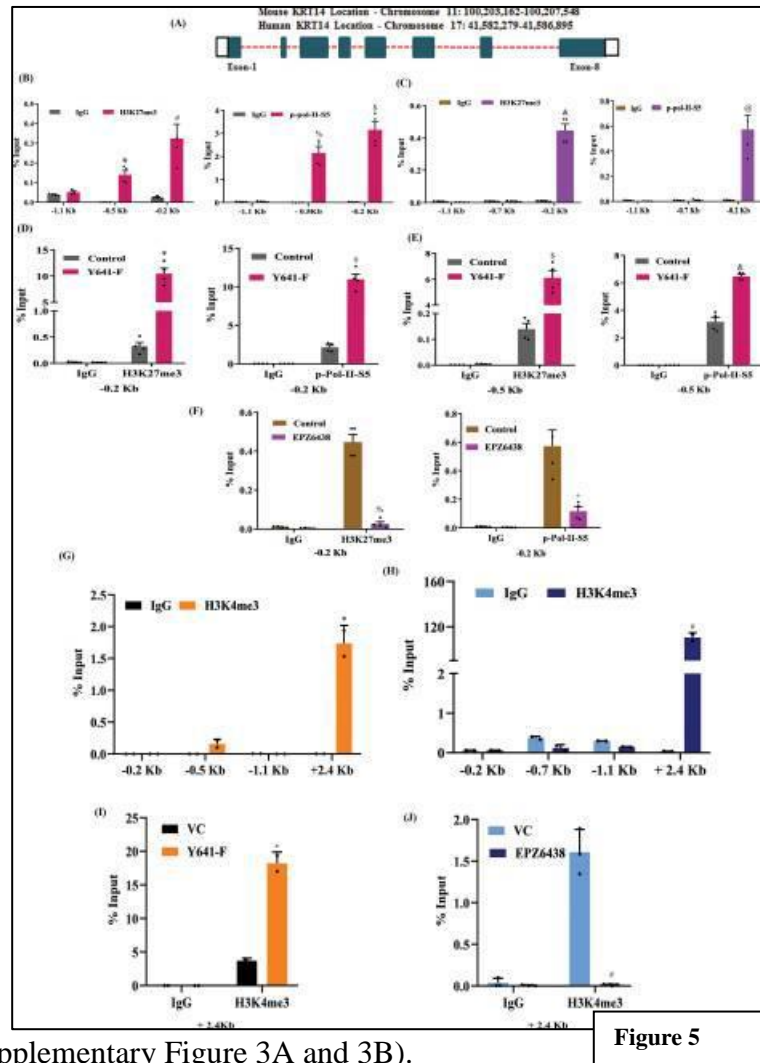
in both 4T-1 and HCC1806 cells (Supplementary Figure 3A and 3B).

As H3K4me3 mark has been associated with transcriptional activation of genes [31], next, we assess its possible involvement in *KRT14* transcriptional upregulation in the presence and absence of increased H3K27me3 state by ChIP-qPCR. We observed the significant H3K4me3 enrichment selectively in the +2.4 kb region from TSS in the *KRT14* gene in both 4T-1 and HCC1806 cells, suggesting the transcriptional progression of *KRT14* (Figure 5G and 5H). Similarly, we found the marked H3K4me3 enrichment in the Y641-F cells in comparison to control 4T1 cells in the same +2.4 Kb region (Figure 5I). Further, we also find a loss of H3K4me3 mark in the +2.4 Kb region of *KRT14* promoter due to the inhibition of H3K27me3 by EPZ6438 (10μM) in HCC1806 cells (Figure 5J). Altogether, these results suggest that though H3K27me3 mark classically acts as a repressor; however, we observe that it promotes *KRT14* gene transcription and the H3K4me3 enrichment in *KRT14* promoter further confirmed its transcriptional activation.

H3K27me3 enhances *KRT14* transcription by attenuating binding of transcriptional repressor SP1 to its promoter

To gain further insight into H3K27me3 mediated *KRT14* transcriptional activation, we search the transcription factors that regulate *KRT14* gene expression through TRRUST online software https://www.grnpedia.org/trrust/ [32]. We found that SP1 acts as a major transcriptional regulator of *KRT14*. The role of SP1 has been highly characterized both as transcriptional activator and repressor [33, 34]. We analyse the presence of putative binding motif of SP1 by employing publicly available transcription factor binding prediction software JASPAR

(http://www.jaspar.genereg.net). The SP1 usually binds to the GC- box of the promoter of the genes and regulates the transcription process. By utilizing the publicly available software Eukaryotic Promoter Database *(epd.vital-it.ch,)* we search the GC-box in the promoter of *KRT14* to confirm the sequence of DNA binding motif of SP1 (Figure 6A and 6B). We have identified the GC- box -116 base upstream of TSS in *KRT14* promoter. To confirm the SP1 involvement in regulating *KRT14* expression at the transcriptional level, we checked the *KRT14* mRNA expression in both HCC1806 and 4T-1 (Y641-F) control and SP1 knock down (KD) cells by performing qRT-PCR. The mRNA results indicate that the SP1 KD enhances the *KRT14* mRNA expression as compared to the control HCC1806 and 4T-1 (Y641-F) cells, respectively (Figure 6C and 6D).

We next examined the expression of SP1 in control and Y641-F 4T-1 cells *via* western blot and observed that the expression of SP1 remained unchanged in the Y641-F cells compared to control (Figure 6E). Furthermore, the western blot data also confirmed the increased KRT14 protein expression in the SP1 knockdown cells compared to control 4T-1 (Y641-F) cells (Figure 6F). After confirming Sp1 knock down in HCC1806 cells (Figure 6G, left panel), we transfected *KRT14* promoter luciferase construct (-1.1 Kb-consisting both proximal and distal region, and -0.5 Kb consisting only proximal region) plasmids in control and SP1 KD HCC1806 cells to confirm the SP1 mediated *KRT14* transcriptional repression. As shown in Figure 6G (right panel), a marked increase in the luciferase activity was observed in both reporter constructs in the SP1 KD cells in comparison to the control suggesting -0.5Kb proximal region (consisting of GC box) is sufficient to inhibit *KRT14* transactivation. Next, we treated the

Figure 6

HCC1806 cells either with vehicle control and two doses (150nM and 300 nM) of SP1 inhibitor Mithramycin, (known to bind GC-rich DNA sequences and attenuate the SP1 binding) and observed mild inhibition of SP1 protein expression (Figure 6H, left panel). To assess the role of SP1 in *KRT14* gene transactivation, we transfected control, and -0.5 Kb *KRT14* promoter-luciferase construct plasmid in HCC1806 cells following vehicle and mithramycin treatments. We found a noticeable increase in the luciferase activity in both the doses of mithramycin as compared to vehicle treatment (Figure 6H, right panel). Together, these findings ossify that SP1 acts as a strong and direct transcriptional repressor for *KRT14*. Interestingly, the H3K27me3 and p-ser-5-Pol-II enrichment have also been recognized in the same region where SP1 binds to *KRT14*. To examine whether H3K27me3 regulates the recruitment of SP1 in the GC-box, we further confirm the binding of SP1 in GC box of *KRT14* promoter. We performed the ChIP q-
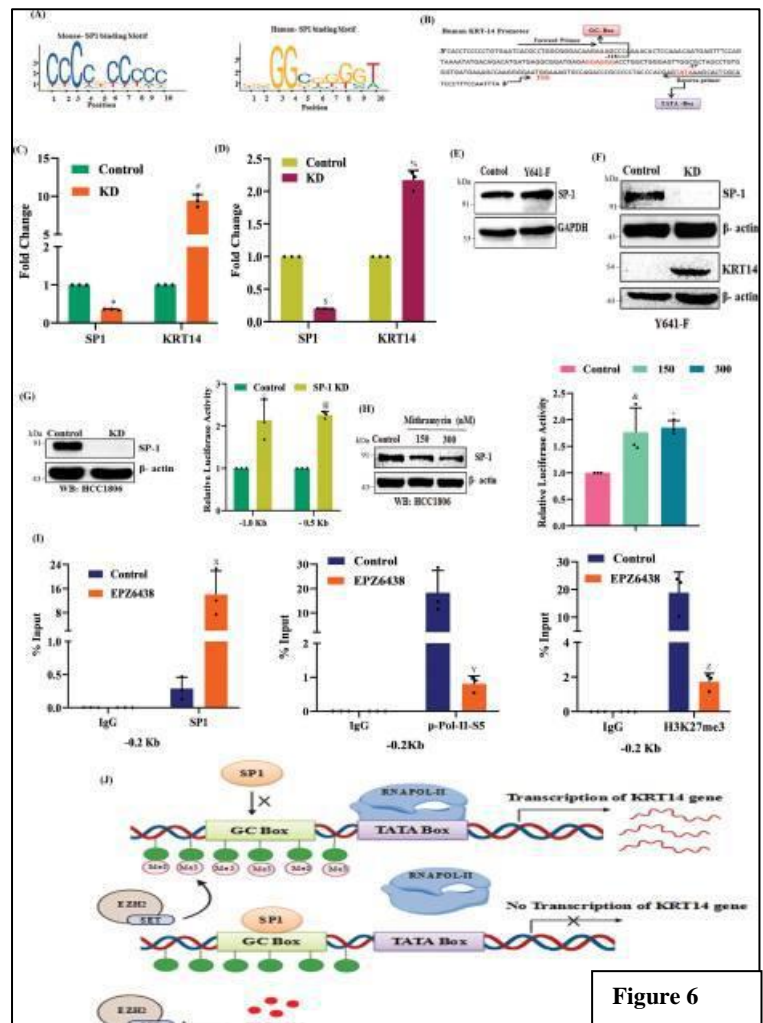
PCR in the SP1 immunoprecipitated DNA in HCC1806 control and EPZ6438 (10μM) treated cells. Here, SP1 recruitment was found to be upregulated in the EPZ6438 treated cells compared to control (Figure 6I, left panel), while the H3K27me3 and p-Pol-II-S5 enrichment in the *KRT14* promoter are downregulated in EPZ6438 treated cells as compared to control cells (Figure 6I, middle and right panels). Overall, these findings suggest that the H3K27me3 may compact the GC box region in *KRT14* promoter to inhibit the SP1 binding in the GC box and permits RNA polymerase-II to initiate the transcription of *KRT14* gene (Figure 6J).

Genetic ablation of *KRT14* impairs splenic metastasis in TNBC

H3K27me3 mediated selective *KRT14* up-regulation in TNBC peritoneal metastasis encouraged us to explore the role of KRT14 in TNBC migration, invasion, and metastasis. First, we knocked down the *KRT14* in 4T-1 (Y641-F) and HCC1806 cells by using the two-specific shRNA against *KRT14* mRNA and validated their efficacy (Figure 7A and 7B). In wound healing assay, we find *KRT14* KD inhibits closure of wound as compared to control (Figure 7C-7F). Similarly, in the trans-well chamber assay, we observe *KRT14* KD cells have lower invasion capabilities than control cells (Figure 7G-7J). To determine the role of KRT14 in TNBC splenic metastasis, we perform the orthotopic single mammary fat pad mixture experiment where (Y641-F) control Td-Tomato$^+$ and (Y641-F) *KRT14* KD GFP$^+$ cells are equally mixed and inoculated in one
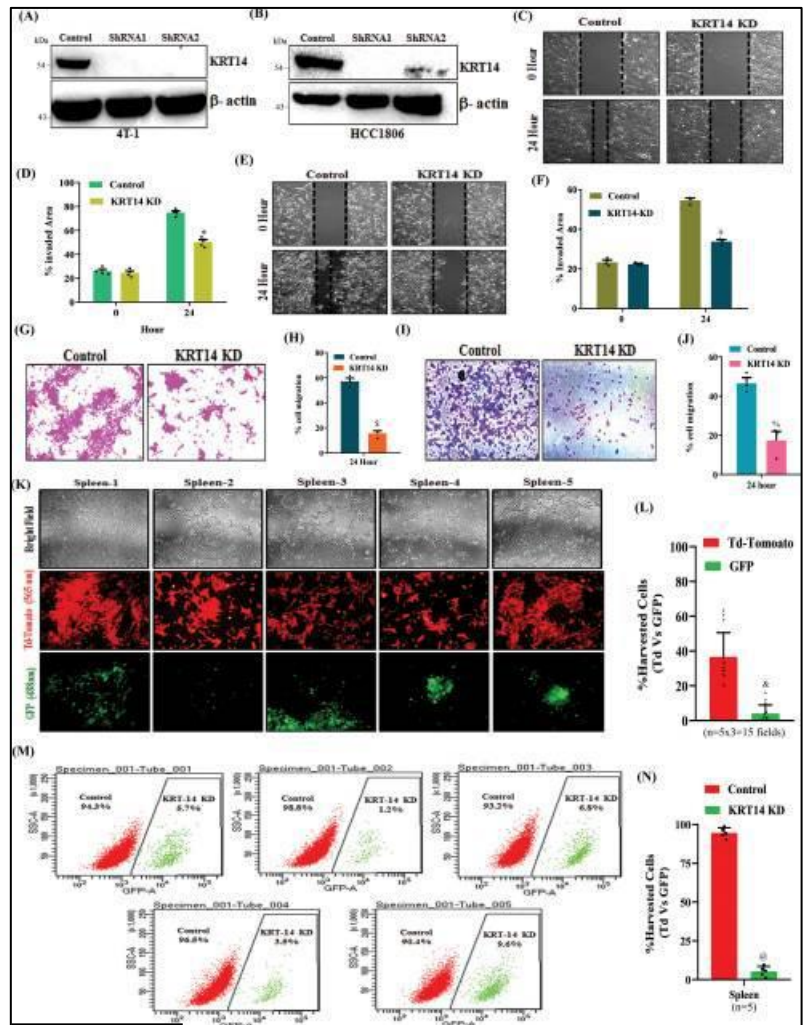

Figure 7

of the mammary fat pads of mice (n=5). After 25 days, we harvested the spleen, isolated the single cells from it, and allowed them to grow for three days with 6-TG selection. As shown in fluorescence microscopy pictures (Figure 7K and 7L), most metastatic cells migrated towards spleen are found to be control Td-Tomato+ cells compared to GFP$^+$ *KRT14* KD cells. Next, cells were trypsinized and analysed by FACS to quantitatively analyse the percentage of Control and *KRT14* KD cells metastasized to spleen. Our FACS analysis clearly suggests that the percentage of migrated metastatic control Td-tomato $^+$ cells is markedly higher in the spleen as compared to metastaticY641-F GFP$^+$ cells (Figure 7M and 7N). Altogether, these studies conclusively demonstrate that loss of KRT14 expression reduces TNBC cell migration and invasion capabilities and markedly hinders TNBC splenic metastasis.

H3K27me3 and KRT14 levels are significantly increased in human TNBC metastasis

To draw a clinical correlation between EZH2 and KRT14 expression, we mined Breast Cancer Yau (2010) dataset from breast cancer patients and observed a high *EZH2* and *KRT14* mRNA expression exclusively in the basal (TNBC) subtype compared to the other breast cancer subtypes (Figure 8A and 8B). Next, we sought to investigate the protein expression correlation between EZH2 and KRT14 in TNBC patient samples from Breast Cancer Gene-Expression Miner v4.8 and discovered the protein expression of EZH2 and KRT14 are positively (p = 0.0018, r = 0.1) correlated with each other (Figure 8C). To address the correlation between EZH2, H3K27me3, and KRT14 expression in human TNBC distant metastasis, parallel sections of TNBC primary tumors and matched metastatic organs (n=10) were stained with antibodies against EZH2, H3K27me3, and KRT14.
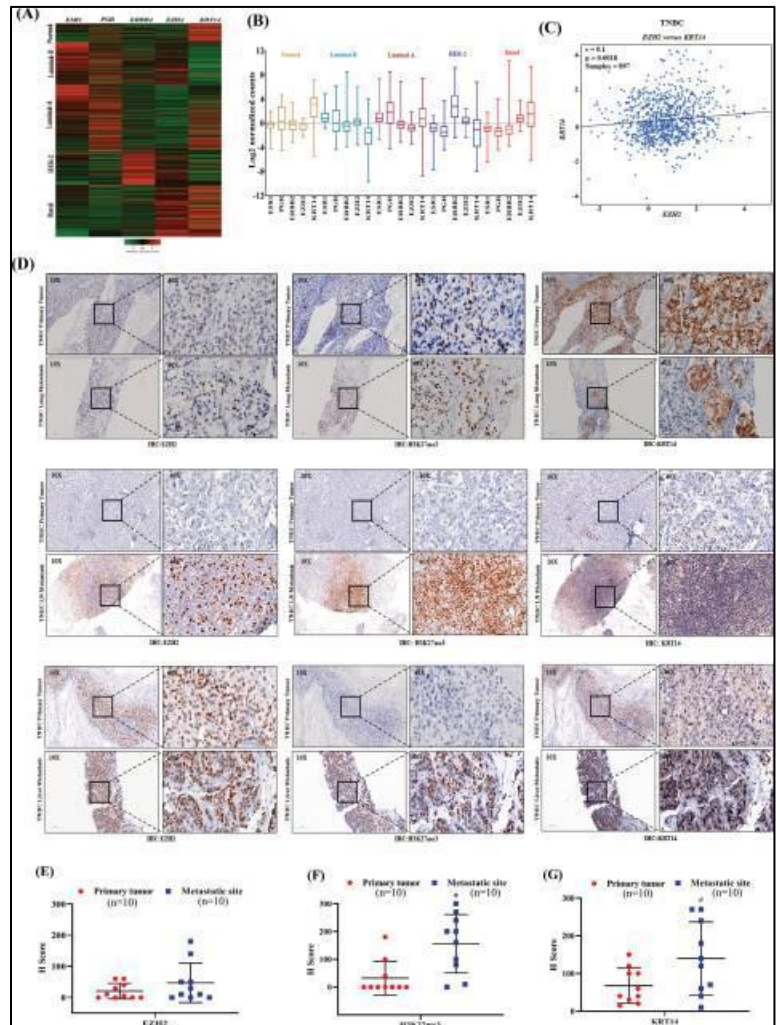

Figure 8

IHC staining of TNBC primary tumors displayed moderate expression of EZH2 and KRT14 but the H3K27me3 level was found to be scanty (Figure 8D-8G). On the other hand, compared with matched primary tumors, respective metastatic counterparts display a visible increase in positive staining for H3K27me3 and KRT14 in most of the TNBC metastatic samples, whereas EZH2 positivity was found to be inconsistent (Figure 8E-8G.). However, TNBC liver metastatic sample exhibits strong positive staining for EZH2, H3K27me3 and KRT14, suggesting that EZH2 is functionally hyperactive in metastatic liver site (Figure 8D, lower panel).

Inhibition of EZH2 impairs TNBC peritoneal metastasis

We wish to explore the clinical relevance of our finding further and finally understand whether EZH2 functional inhibition rescues the *in- vivo* phenotype. In this endeavor, we confirm EZH2 knockdown in 4T-1 cells through immunoblot (Figure 9A). Indeed, EZH2 knockdown cells display less migratory (Figure 9B and 9C) and invasive (Figure 9D and 9E) potential than their respective controls. Further, the serial bioluminescence imaging and analysis of harvested organs from control EZH2 KD tumor-bearing mice reveal that the depletion of EZH2 restricts the peritoneal metastasis as compared to the respective control (Figure 9F-9H). Also, compared to control, EZH2 KD increases mice survival, as shown in Figure 9I. As EZH2 inhibitor EPZ6438 (tazemetostat) recently received FDA approval for sarcoma treatment, we readily evaluated its

potential to inhibit TNBC migration, invasion, and metastasis [35, 36]. As observed in Figure 9J-9M, EPZ6438 treatment results in marked inhibition of TNBC migration and invasion, compared to their respective controls. Consistent with the genetic depletion of EZH2, we observe a visible decrease of peritoneal metastasis following daily oral administration of EPZ6438 (250mg/kg) though primary tumor burden remains same in both control and treatment group (Figure 9N-9P and Supplementary Figure 4). Moreover, EPZ6438 treatment resulted in a marked increase in mice survival as compared to the vehicle-treated group (Figure 9Q).

Overall, our *in vitro*, *in vivo*, and human patient sample data suggest that the EZH2-H3K27me3-KRT14 axis may be one of the critical regulators of TNBC peritoneal metastasis, and FDA approved EZH2 inhibitor EPZ6438 or
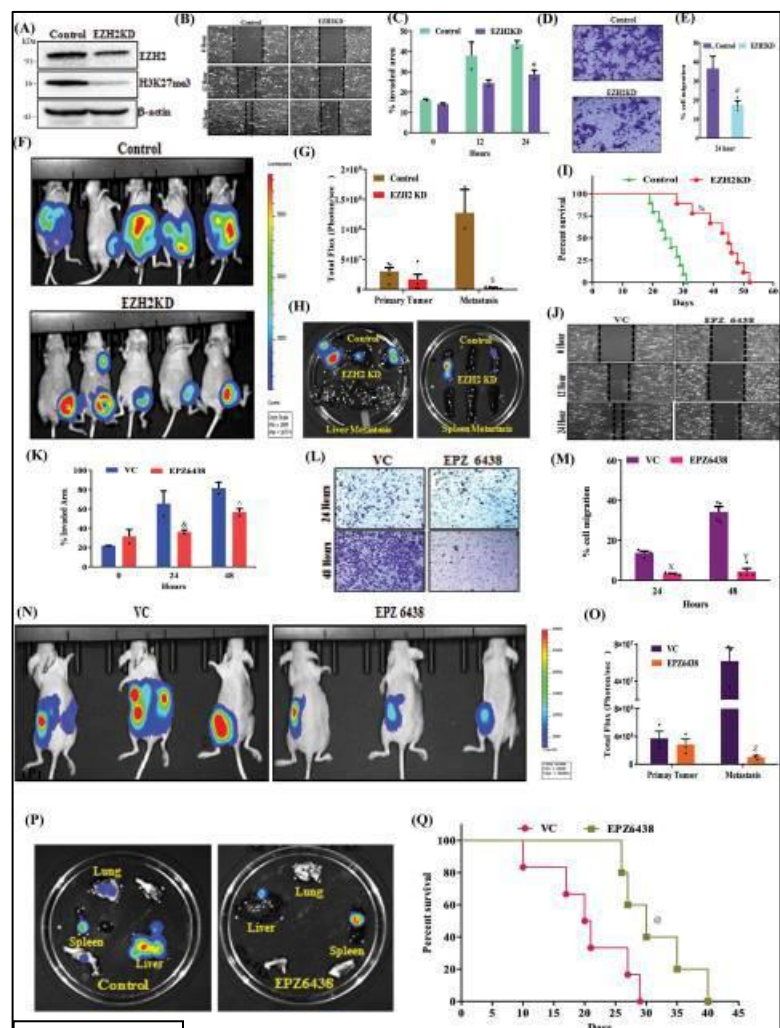

Figure 9

Tazemetostat could be a potential therapeutic option against TNBC progression (Figure 10).

Discussion

In the current study, we set out to dissect H3K27me3 versus NC- EZH2 in basal-like TNBC growth and progression and discover that H3K27me3 is the key to TNBC peritoneal metastasis. Transcriptome analyses and subsequent validation lead us to ascertain KRT14 as a target of H3K27me3. Importantly, we observe an increased H3K27 tri-methylation mark for transcriptional activation of *KRT14* instead of

Figure 10

H3K27me3 mediated classical transcription repression. Loss of EZH2 or KRT14 or H3K27me3 function results in robust inhibition of TNBC peritoneal metastasis, particularly splenic metastasis. The human patient sample data also revealed a positive correlation between H3K27me3 and KRT14 expression in TNBC metastasis including liver metastasis.

Underpinning our observations, recently, Mittal group performed a bioinformatic analysis of 2,000 patients in the breast cancer cohort and identified that TNBC patients had shown the
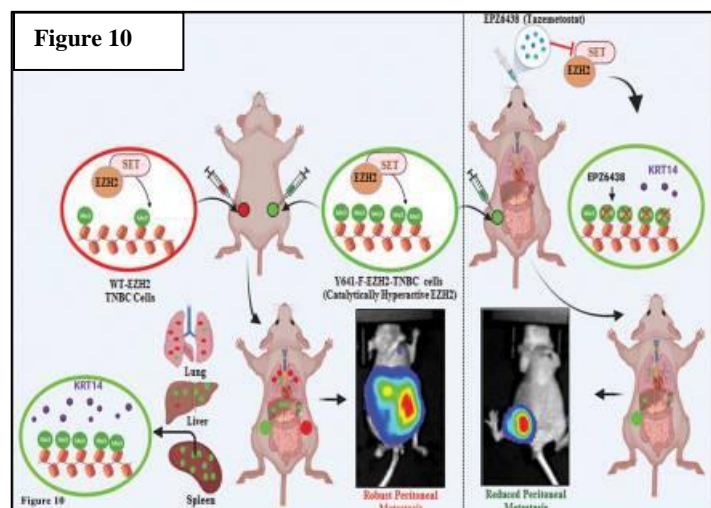
enhanced expression of EZH2 with over all poor survival rate [19]. Moreover, several human tissue microarray studies correlated EZH2 with poor prognosis in TNBC [11, 37, 38]. In support of all the pre-existing information, our analyses further prove that, particularly in basal-like TNBC subtype, which covers 80% of the whole group [4], EZH2 activity is a critical driver for TNBC progression. Moreover, EZH2 overexpression in breast cancer does not always correlate with increased expression of global H3K27me3 [9, 39, 40]. It is inadequately established whether TNBC with distinct levels of EZH2 protein and its catalytic function (H3K27me3) belongs to the same or different biological behaviour. Recently, the Dihua group highlighted EZH2 methytransferase independent role in breast cancer brain metastasis. One of their studies suggest that EZH2 promotes TGFβ signaling to promote breast cancer bone metastasis via activation of integrin β1-FAK signaling[41, 42] following intra-cardiac or tail vein inoculation of breast cancer cell. However, we primarily observe peritoneal and lung metastasis but not brain metastases in our *in vivo* imaging experiments following orthotopic inoculation of EZH2 hyperactive breast cancer cells. These findings again suggest highly context dependent function of EZH2 even in regulating organ specific metastasis of breast cancer. Peritoneal metastasis is a classical signature of TNBC metastasis in patients, which is largely missing in most of the preclinical studies as the route of tumor cell inoculation is not always orthotopic, instead, it is tail vein or intra-cardiac [43, 44]. Further, it has been shown that the peritoneal metastasis is associated with poor survival among the other distant metastatic sites of breast cancer [45, 46, 47]. Therefore, our observations regarding H3K27me3 dependent TNBC splenic metastasis display the actual clinical scenario, and its further inhibition may have translational impact on TNBC pathophysiology. Previously, another compelling study showed the effect of epigenetic reprogramming in the progression of pancreatic ductal adenocarcinoma (PDAC) and identified the substantial difference in the enrichment of repressive (H3K9me3) and activating (H3K27ac and H3K36me) marks between peritoneal and distant metastasis [48]. Similarly, we also identified a massive epigenetic reprogramming in the expression of global H3K27me3 between the isolated cells from primary tumor versus cells from peritoneal metastatic organs like spleen and liver. Further, we observe that isolated H3K27me3 enriched spleen metastatic cells have even aggressive disease progression and fatality in mice indicating the critical correlation between elevated H3K27me3 function and TNBC progression and its overall poor survival.

Our transcriptome analysis of H3K27me3^High cells not only identifies cytokeratin 14 (*KRT14*) as a fresh target of H3K27me3 in TNBC but also establishes a unique correlation between induction of H3K27me3 with upregulation of gene (*KRT14*) expression. In support of our positive regulatory circuit between H3K27me3-KRT14, Granit *et.al.,* earlier demonstrated silencing of EZH2 protein reduces the expression of KRT5 and KRT14, whereas promotes expression of the luminal cytokeratin KRT18 in course of maintaining bi-lineage identity in basal-like breast cancer[49]. Usually, EZH2 mediated silencing of genes is the fundamental mechanism of the PRC2 complex as described by several elegant studies [17, 18, 30, 50]. Despite its classical suppressive function, Majewski group first documented enrichment of H3K27me3 in the transcriptionally activated genes [51]. In correlation with our finding, H3K36me3 and H3K4me2 also have a contrasting impact on gene expression depending on their differential distribution in chromatin landscape[52, 53]. The evolution in the ChIP-Seq pipeline revealed that the chromatin landscape is highly dynamic, and the distribution of epigenetic marks is not universal. Multiple ChIP-seq studies advocate that the PRC2 binding is identified in relatively very minor part of the genome; however, its catalytic product is found in 70-80% of all H3 [54, 55, 56, 57]. In support of such observations, we also did not find any enrichment of particular genes when we performed ChIP with EZH2 antibody (Supplementary Figure 3A and 3B) again suggesting that the epigenetic modulators and their biological products may not always be correlative in terms of recruitment and gene regulation. Similarly, in clinical samples, we observe good degree of correlation between the expression H3K27me3 and KRT14 in TNBC metastasis where EZH2 levels failed to corroborate with high

H3K27me3 level. Indeed, any epigenetic signature changes in the classical distribution pattern may change the global network of gene transcription [51, 52, 53, 58]. Further extending the concept, here we provide an insight that recruitment of transcription factor can be controlled by epigenetic modulators as H3K27me3 promotes *KRT14* transcription by inhibiting the binding of transcription factor SP1 to its promoter in TNBC cells. Another essential aspect of our study is the positioning of KRT14 as one of the potential metastatic regulators in TNBC. So far, it is well known as an intrinsic molecular marker for basal-like TNBC [4, 24], but our studies demonstrate its functional significance in TNBC pathophysiology. In support of our observations, several reports have suggested that the KRT14+ cells have a metastatic advantage compared to KRT14- cells in the TNBC heterogeneous population and they regulate the function of a wide plethora of genes involved in different stages of metastatic cascade. [21, 59, 60]. Further, KRT14 expressing cells act as stem cells for the natural or injury-induced bladder regeneration and typically lead to the origin of bladder cancer [61]. Though H3K27me3-KRT14 axis played major role in delineating TNBC peritoneal metastasis in our experimental set up, contribution of other regulatory factors such as EZH2 mediated suppression versus activation of gene expression should also be carefully considered in the bigger picture of TNBC metastasis.

Existing literature indicates that the role of EZH2 in tumor growth and progression is highly context-dependent as mentioned earlier, and to some extent, it exerts an opposite effect in different types of cancers. Our recent studies in colon cancer, as well as another thorough study by Gonzalez *et.al,* in breast cancer, reiterate that loss of EZH2 results in primary tumor growth inhibition, whereas our current observation in TNBC shows no significant impact of EZH2 in primary tumor growth [12, 62]. Consistent with our anti-metastatic effect of EZH2 inhibitor, recent studies [19, 39] that tested the effect of EZH2 HMT inhibitor (GSK-126) against TNBC and luminal B breast cancer, respectively, also witnessed the robust anti-metastatic potential of EZH2 inhibitor. Targeting EZH2 with methyltransferase inhibitors has not always been advantageous in clinical trials, apparently due to the EZH2 methyltransferase-independent functions in tumorigenesis[63, 64]. Moreover, various preclinical and clinical studies suggest that the EZH2 inhibitor (Tazemetostat) showed better efficacy and minimize therapy relapse primarily in lymphomas but not in solid tumors[64]. Tazemetostat selectively inhibits H3K27me3 function of EZH2 but not the level of total EZH2 protein and lymphomas have survival dependency on H3K27me3 function[65]. The overall discrepancy of efficacy of EZH2 inhibitors in lymphoma versus solid tumors including TNBC in the context of primary tumor growth is due to the lack of particular mutations (Y646, A682, and A692) in solid tumors that are present in lymphomas. These gain of function mutations result in catalytically hyperactive EZH2 in 25-27% of germinal center follicular lymphomas and make them vulnerable for EZH2 inhibition therapy. Therefore, Tazemetostat has proven to be very effective in reducing primary tumor growth in lymphomas, whereas, selective loss of H3K27me3 function by Tazemetostat does not impact on primary tumor growth or tumor cell proliferation in most solid tumors. However, as observed by us and others, selective loss of H3K27me3 function of EZH2 poses significant inhibitory influence on cancer cell migration and tumor metastasis [19]. Context dependency is profound even in terms of EZH2-dependent gene regulation. Our breast cancer (Yau 2010) data mining in the PAM50 subtypes of breast cancer cohort display a positive correlation between EZH2 and KRT14 expression selectively in basal breast cancer subtype (TNBC) among all breast cancer subtypes. In compliance with preclinical observations, the EZH2-H3K27me3-KRT14 axis is highly overexpressed in peritoneal (liver) metastasis of human TNBC samples compared to matched primary tumors. However, in the case of other secondary organ metastases such as lung, we found marked upregulation of H3K27me3 level compared to matched primary tumors, but EZH2 level on these metastatic sites failed to correlate with H3K27me3 expression suggesting EZH2-independent mechanisms may be involved in such cases. Demethylases like UTX/KDM6A could be potential candidates to be considered for further investigation[27]. Therefore, the clinicians

should carefully consider the EZH2 therapeutic window as EPZ6438 (EZH2 inhibitor) or Tazemetostat recently received FDA approval against sarcoma [35, 36].

In conclusion, our results reveal that the EZH2 catalytic activity enhances KRT14 expression in the basal-like TNBC subtype. Mechanistically, we have excavated that instead of the classical suppression function; H3K27me3 can promote specific gene expression, like KRT14 transcriptional upregulation to govern the TNBC peritoneal metastasis. Further, we corroborate the critical involvement of EZH2-H3K27me3-KRT14 axis in human TNBC metastasis. Finally, we identify that the EZH2 inhibitor drug Tazemetostat (EPZ6438) can be a promising therapeutic option against the most aggressive TNBC subtype, where targeted therapy is still an enigma.

Methods

Study Approval

All animal studies were conducted by following standard principles and procedures approved by the Institutional Animal Ethics Committee (IAEC) of CSIR-Central Drug Research Institute (Protocol Number: IAEC/2018/F-65). All studies with clinical specimens were approved by the Institutional Review Board of the Rajiv Gandhi Cancer Institute and Research Centre (RGCIRC), New Delhi, India (Protocol Number: Res/BR/TRB-24/2021/43) and CSIR-CDRI Institutional Human Ethics Committee (IEC), Lucknow, India (Protocol Number: CDRI/IEC/2022/A9).

Reagents and antibodies

Dimethyl Sulfoxide (DMSO), Bovine Serum Albumin (BSA), anti-β-Actin (cat# A3854, 1:10,000) antibody, Crystal violet dye, doxycycline and Polybrene were purchased from Sigma-Aldrich. EPZ6438 was purchased from Apex biosciences. XenoLight D-Luciferin potassium salt (P/N 122799) obtained from Perkin Elmer. ProLong™ Gold Antifade Mountant was purchased from Invitrogen. Isoflurane (FORANE) was bought from Baxter U.S. Health Care. Matrigel Invasion Chamber (24 well plate 0.8 microns, Lot-8351001) was purchased from Corning. Magnetic ChIP kit and antibodies for EZH2 (cat# 5246S), H3k27me3 (cat# 9733S), H3k4me3 (cat# 9751S), p-PolII-S5 (cat# 13523S), Sp1 (cat# 9389S) were purchased from Cell Signaling Technology (CST) and used in 1:1000 dilution for WB studies and 1:50 for IHC and ChIP studies wherever applicable. The antibody for GAPDH (#25778, 1:1000) and anti-mouse SP1 (cat# sc-17824, 1:500) were purchased from Santa Cruz Biotechnology. Antibody for KRT14 (cat# ab7800, 1:1000), and Ki-67 (cat# ab16667, 1:1000) were procured from Abcam. PVDF membrane and stripping buffer were obtained from Millipore Inc. BCA protein estimation kit, RIPA cell lysis buffer, blocking buffer, Super Signal West Pico and Femto chemiluminescent substrate, Lipofectamine-3000, Puromycin, Alexafluor 488/594 conjugated secondary antibodies, FBS, RPMI-1640 media, Anti-Anti, DYNAmo Color Flash SYBR Green qPRC kit (cat# F-416L) were purchased from Thermo Fisher Scientific. Primers for real time PCR and ChIP assay were purchased from IDT Inc (Details of primer are listed in the Supplementary Table 2 and 3). Dual luciferase assay kit (cat# E1910) was purchased from Promega. Iscript AdV cDNA kit for RT-PCR (cat# 1725038) was purchased from *BIO-RAD*. RNeasy Mini Kit (cat#74104) was bought from Qiagen. Ex prep™ plasmid SV mini (cat# 101-150) procured from Gene All. The scrather was purchased from SPL life sciences. The collagenase Type I (cat# 1700-017) was purchased from Gibco. All chemicals and antibodies were obtained from Sigma or Thermo scientific unless specified otherwise.

Procurement and culture of cell lines

Various basal like or basaloid TNBC human (HCC1806, CRL-2335 and MDA-MB-468, HTB-132) and mouse (4T-1, CRL-2539) cell lines were obtained from American Type Culture Collection (ATCC), USA. Mycoplasma free early passage cells were revived from liquid nitrogen vapor stocks and inspected microscopically for stable phenotype before use. Human cell lines used in the study are authenticated by STR profiling. All experiments were performed within early passages (<10) of individual cell lines. Cells were cultured as monolayers in recommended media supplemented with 10% FBS, 1-X anti-anti (containing 100 μg/ml streptomycin, 100

unit/ml penicillin and 0.25 μg/ml amphotericin B) and maintained in 5% CO_2 and humidified environmental 37°C.

Generation of stable cell lines

MSCV (cat# 24828), MSCV EZH2 ΔSET-Hygro (cat# 49403) EZH2-Y641-F (cat# 80077), pTRIPZ M)-YFP-EZH2 (cat# 82511), MSCV-EZH2OE (cat#75125), MSCV–EZH2^{EZH1SET} (cat#75126) were procured from Addgene USA. Control (MSCV), EZH2 ΔSET-Hygro and EZH2-Y641-F cell lines were generated by utilizing retroviral mediated transduction system followed by puromycin selection. The HEK293-T (ATCC- CRL-3216) cell line was used for the generation of viral particles following standard protocol. The HEK293-T cells were plated in the 6-well plate at 80% confluency. Polybrene (8μg/ml) was added to the viral soup during the transduction matured viral particles into the target cells. MSCV control cell were subjected to puromycin and EZH2 Y641-F and EZH2 ΔSET cells were subjected to hygromycin selection, and the overexpression of stable EZH2, ΔSET and EZH2-Y641-F were confirmed by western blot. Following the same protocol reported in our recent publication [66] *EZH2* mouse, *KRT14* mouse and Human shRNA, *SP1* mouse and human and *UTX* mouse shRNA sequence were cloned in the 3rd generation transfer plasmid pLKO.1 TRC cloning vector (Addgene cat # 10878) between unique AgeI and EcoRI restriction sites downstream of the U6 promoter. HEK-293T cell line was used for the generation of lentiviral particles and media containing the viral particles was supplemented with Polybrene (8μg/ml) for the transduction purpose. Cells were subjected to puromycin selection after 48 hours of transduction, and the knockdown for EZH2 and KRT14 were confirmed by western blot. ShRNA sequences were listed in the Supplementary Table 4.

Patient sample collection

A total of 3500 Breast Cancer patients were screened that had reported to RGCIRC between the years 2015-2019. The time frame chosen was such that a two-year follow up period could be accounted for. Out of these 3500 patients, 600 cases qualified as triple negative BC patients based on IHC and Her2 by FISH analysis and who had also undergone surgery and other treatments at RGCIRC. Complete follow-up data of these 600 patients was analysed to look for disease progression in the form of local recurrence or distant metastasis. Approximately, 60 patients had recurred or progressed at varying time points. Of these 60 cases, 10 TNBC cases (patient details are enlisted in Supplementary Table 6) were selected wherein there was a matched tumor block and a matched metastatic site block was available. Formalin-fixed, paraffin-embedded specimens of 10 primary TNBC cancer tissues and matched 10 metastatic samples were used for IHC staining.

Immunohistochemical (IHC) staining and analysis

IHC staining was performed using Ventana Benchmark XT automated closed system following their recommended protocol. EZH2 and H3K27me3 antibodies were purchased from Cell Signaling Technology and KRT14 was obtained from Abcam. Colon, Skin and Appendix were used as internal positive control for KRT14, EZH2, and H3K27me3 staining respectively. All stained slides were analysed by Leica Aperio ImageScope software. The staining intensity of each section was scored as 0 (no staining), 1+ (weak staining), 2+ (moderate staining), or 3+ (strong staining). The tumor cell positive rate (0% to 100%) per slice was multiplied by the staining intensity to get an overall H-scores ranged from 0 to 300.

Cloning of *KRT14* promoter in luciferase reporter vector and luciferase assay

The 500bp (-0.5 Kb from TSS) and 1100 bp (-1.1 Kb form TSS) *KRT14* fragments were amplified from Hela cell DNA by PCR. The amplified fragments were cloned into the PGL4.12 [*luc2 CP*] vector between the HINDIII and BglII restriction sites. The control and SP1 KD HCC1806 cells were seeded at 50-60% confluence in 6 well plates and transfected with 5μg of PGL4-1.1 Kb KRT14-P, and 50 ng of PGL4 (hRluc-CMV) plasmid using lipofectamine 3000 as transfection reagent (Invitrogen). The same process was used for PGL4-0.5 Kb KRT14-P. For mithramycin

treatment, the PGL4-0.5 Kb KRT14-P transfected HCC1806 cells were treated either with vehicle control or two doses of mithramycin (150nM and 300nM) for 24 hr. Lysis buffer contained in Dual-Glo Luciferase assay kit (Promega) was used to lyse the cells. The activities of Firefly and Renilla luciferases were measured using the GloMax® 96 Microplate Luminometer according to the manufacturer's procedure (Promega). Firefly luciferase activity was normalized to Renilla luciferase activity for each sample. Luciferase KRT14 promoter primers are enlisted in Supplementary Table 5.

MTS assay

The 4T-1 cells were seeded in the 96 well plates at a density of 8,000 cells per well in the 5% serum-containing media (100μl) overnight. The adhered cells were treated with vehicle control and 3 doses of EPZ6438 (10μM, 20μM, and 40μM) for 48 h. for MTS assay, the Cell Titer96 [R] Aqueous One Solution Proliferation Assay Kit was used following the manufacture's instruction. The 20 μl of the MTS reagent was added to each well and incubated at 37^0C for 4 h. The absorbance was detected at 490nm by plate reader.

Western blotting

Cells were subjected for lysis in RIPA buffer containing phosphatase and protease inhibitor cocktail and incubated at -20^oC for 48 hour and subsequently the samples were thawed at RT and centrifuged at 5000g for 15 min at 4°C, supernatant was collected and the pallet was discarded. The Protein concentrations were estimated by utilizing the BCA kit. Equal amounts of protein were resolved by SDS-PAGE and transferred to a PVDF membrane. Membranes were blocked with 5% nonfat dry milk or 5% BSA followed by incubation with appropriate dilutions (1:1000) of primary antibodies overnight at 4°C and subsequently incubated with a 1:5000 dilution of horseradish peroxidase-conjugated secondary antibodies for 1 hour at room temperature. Immunoreactivity was detected by enhanced chemiluminescence solution (ImmobilonTM western, Millipore, USA) and scanned by the gel documentation system (Bio-Rad chemidoc XRS plus).

RNA Seq analysis

Illumina NovaSeq was used to perform transcriptome sequencing followed by the Fast QC and Multi QC tools were used to assess data quality. Adapter sequences (P7 adapter read 1: AGATCGGAAGAGCACACGTCTGAACTCCAGTCA and P5 adapter read 2: AGATCGGAAGAGCGTCGTGTAGGGAAAGAGTGT) and low-quality bases were removed from raw sequence reads using fastp. Using the STAR v2 aligner, the QC-passed reads were mapped onto the indexed *mus musculus* genome (GRCm39) [67]. Gene expression levels were calculated as read counts using feature-counts software. Spearman Rank correlation and Principal Components Analysis (PCA) was used to assess the similarity of expression between biological replicates. For differential expression analysis, the biological replicates were grouped as Control and Y641-F. Differential expression analysis was carried out using the edgeR package after normalizing the data based on trimmed mean of M (TMM) values [68]. After normalization, 19162 features (47.66%) have been removed from the analysis because they did not have at least 0.1 counts-per-million in three replicate samples. Genes with absolute Log_2FC +1, -1 and p-value $\leq$ 0.05 was considered significant. The expression profile of differentially expressed genes across the samples is presented in volcano plot.

Gene Set Enrichment Analysis (GSEA)

Gene set enrichment analysis was performed using updated version GSEA 4.2.2 (https://www.gsea-msigdb.org/gsea/index.jsp) using h.all.v7.5.1.symbols.gmt (Hallmarks) gene set database and mouse gene symbol remapping human orthologs MSigDB v7.5.1.chip with allowed 1000 permutations and permutation type selected was phenotype [69].The heat map of the genes enriched at the top or bottom of the gene sets were identified using the FDR value threshold (p < 0.05) and ranked according to the normalized enrichment score.

Real-time PCR

Total RNA was isolated from cultured cells using the standard procedure of the RNeasy Mini Kit (Qiagen, cat # 74104). The concentration and purity of the RNA samples was determined using nanodrop. Total RNA (7 μg) of each sample was reverse-transcribed (RT) with iscript ADV cDNA synthesis kit. The final cDNA was diluted with nuclease-free water (1:3), 1μl of this having a concentration of 80ng/μl was used for each reaction in real-time PCR. Real-time PCR was carried out using an ABI Step One plus Real-Time PCR System (Applied Biosystems). Reactions for each sample were performed in triplicate. 18s amplification was used as the housekeeping gene. A gene expression score was calculated by taking two raised to the difference in Ct between the housekeeping gene and the gene of interest (2 ΔCt). For amplification of *NIFK, ADAMTS1, CCN2, JAG1, SEMA3C, TM4SF1, CYP1B1, KRT14, KRT16, NCAM1, AQP1, BNIP3, CBS, CCNG2, ARRB1, NDRG1, and SP1,* we performed SYBR Green based RT-PCR following manufacturer's instructions. Primers were listed in the Supplementary Table 2.

Chromatin Immunoprecipitation (ChIP) Assay

ChIP assay was conducted by using the ChIP assay kit (Cell Signaling Technology) following the manufacturer's protocol. In brief, cells at 80% confluence were fixed with formaldehyde (1% final concentration directly to the culture media) for 10 minutes. Cells were then centrifuged, followed by lysis in 200μl of membrane extraction buffer containing protease inhibitor cocktail. The cell lysates were digested with MNase for 30 minutes at 37°C to get chromatin fragments followed by sonication (with 20 second on/20 second off 3 Sonication cycles at 50% amplitude) to generate 100-500 bp long DNA fragments. After centrifugation, clear supernatant was diluted (100:400) in 1X ChIP buffer with protease inhibitor cocktail followed by keeping 5% of input control apart and incubated with primary antibody or respective normal IgG antibody overnight at 4°C on a rotor. The next day, IP reactions were incubated for 2 hours in ChIP-Grade Protein G Magnetic Beads, followed by precipitation of beads and sequential washing with a low and high salt solution. Then elution of chromatin from Antibody/Protein G Magnetic beads and reversal of cross-linking was carried out by heat. DNA was purified by using spin columns, and SYBR Green based real-time PCR was conducted. Primer sequences used for the ChIP experiment for different genes are enlisted in Supplementary Table 3.

Confocal microscopy

Control and treated cells were fixed with ice-cold pure methanol for 10 min at -20º C followed by blocking with 2% BSA for 1 hour at RT. After overnight primary antibodies (anti-H3K27me3 and anti-KRT14) incubation, cells were washed twice with PBS and incubated with fluorescent-conjugated secondary antibodies at RT for 1 hour, followed by DAPI staining for 5 min at RT. After washing, cells were mounted with anti-fade mounting medium on glass slides and viewed under an inverted confocal laser scanning microscope (Zeiss Meta 510 LSM; Carl Zeiss, Jena, Germany). Plan Apochromat63X/1.4NA Oil DIC objective lens was used for imaging and data collection. Appropriate excitation lines, excitation and emission filters were used for imaging.

Wound healing assay

For wound healing assay, 500,000 cells were seeded in to 6 well plates and incubated for overnight to form a confluent monolayer. The scratch has been made by scrather to generate a straight-line scratch in the cell monolayer. The cells were washed with PBS and cultured with fresh complete RPMI media at 37^0C for different time intervals. The cells were incubated at 37^0C for different time intervals with or without treatments. Five (5) reference points were randomly selected from single well at different time intervals and percentage of wounds healed area was measured by Image J software. Three independent replicate experiments were conducted for single data representation.

Invasion Assay

For each invasion assay, cells were re-suspended in 500μl of serum free RPMI and was added to the inside of Matrigel inserts (Coring Bio Coat) and DMEM media with the 10 % serum was added outsides of inserts. The Matrigel invasion chambers incubated for 24 hours at 37^0C. The

non-invading cells were then removed by scrubbing with cotton tipped swab. Invasion chambers were fixed with 100 % methanol for 5 minutes. The invasion chambers were stained with crystal violet for 1 hour and then washed with PBS twice. 5 reference points were randomly selected for each invasion camber. The number of invaded cells were analysed by Image J software. Three independent replicate experiments were conducted for single data representation.

Animal studies

Experimental mice were maintained in IVC cages under pathogen-free conditions with a 12 h light/12 h dark cycle, at $24 \pm 2\,°C$ temperature with humidity of $45 \pm 5\%$, and were fed with irradiated standard mouse diet at CSIR-CDRI Central Laboratory Animal facility. Six-week-old female Balb/c nude mice were used for all studies. For orthotopic inoculation, different tagged (GFP, Td Tomato, Luc) 4T-1 cells $(1x10^6)$ in 100 µl was injected in to the mammary fat pad of 4–6-week-old nude Crl: CD1-Foxn1^{nu} female mice, whereas, same number of cells were inoculated in dorsal right flank for subcutaneous mice model. For tracking of genetically manipulated metastatic cells as described in Figure 4A-4C, following strategies were adapted. First strategy: The Td-Tomato$^+$ control and EZH2 (Y641-F) GFP$^+$ cells were mixed in equal ratio (1:1). The 100µl of mixed cells $(0.5 \times 10^6$ Td- Tomato $^+$ 0.5×10^6 Y641-F-GFP$^+)$ were orthotopically inoculated in the right mammary fat pad of female nude (n=5). 2nd strategy: The MSCV Td-Tomato$^+$ control and EZH2 (Y641-F) GFP$^+$ cells were mixed in equal ratio (1:1). The 100 µl of mixed cells $(0.5 \times 10^6$ Td- Tomato $^+$ 0.5×10^6 Y641-F –GFP$^+)$ were inoculated *via* tail vein in the female nude mice (n=5). 3rd strategy: the control $(0.5 \times 10^6$ Td- tomato$^+)$ and EZH2 $(0.5 \times 10^6$ Y641-F GFP$^+)$ cells in 100 µl PBS were orthotopically inoculated in the right and left mammary fat pad of female nude mice (n=5). EPZ6438 (250mg/kg dose) or vehicle (0.5% NaCMC + 0.1% Tween-80 in water) was administered per day by oral gavage for 24 days after 1 week of post tumor cell inoculation. Throughout the study, tumors were measured with an electronic digital caliper at regular interval and the tumor volume was calculated using standard formula $V = \Pi / 6 \times a^2 \times b$ ('*a*' is the short and '*b*' is the long tumor axis). At the end of experiment, mice were sacrificed, and tumors were dissected for further studies. Tumor volume of mice did not go beyond 2500 mm3 as allowed by the Institutional Animal Care and Ethical Committee. Live animal bioluminescent imaging (IVIS spectrum, Perkin Elmer) performed once per week of post inoculation. For *in- vivo* imaging studies, 150 mg/Kg D-Luciferin (10mg/ml in PBS) was injected intraperitoneal in the tumor bearing mice. Subsequently, mice were anesthetized by Isoflurane. Images were captured with dorsal and ventral positions using Perkin Elmer IVIS system coupled with bioluminescence image acquisition and analysis software. Regions of interest (ROI) from displayed images were identified on the tumor and metastatic sites and quantified as photons per second (p/s) using Living Image software. Spectral unmixing was used to detect Td–tomato and GFP signals in the same mice, and finally data were acquired at 570 nm (Td) and 465 nm (GFP).

Colony formation assay

The 4T-1 cells were seeded at 200 cells per well in 12 well plates, after 24 h the adhered cells were treated either with the vehicle and different doses of EPZ6438 (10µM, 20µM, and 40 µM) and incubated for a week at 37^0C. Subsequently, the media was aspirated followed by two times PBS washing. The washed cells were fixed with ice-cold methanol for 10 minutes and stained with 0.5 % crystal violet dye for 1h. The excess stain was washed by water and the plates were allowed for air dry. The stained colonies were counted by Image J Software.

Tumor cell isolation form peritoneal fluid

4T1 tumor bearing mice were euthanized and sprayed with 70% ethanol. The outer skin of peritoneum was cut with the help of scissors and forceps and then the skin was gently pulled back to expose the inner skin, lining the peritoneal cavity. Ice cold PBS was injected in to the peritoneal cavity with the help of a needle and the peritoneal fluid with cell suspension was collected and kept in tubes on ice. The collected cell suspension was spun at 1500 RPM for 10

minutes, supernatant was discarded and cells were resuspended in desired media in presence of 60 μM of 6-TG.

Isolation, culture and analysis of metastatic cells

Mice were sacrificed and primary tumors and other organs were harvested under sterile condition. Single cell suspension was prepared following standard protocol. Briefly, chopped tissues were incubated in HBBS solution containing 1mg/ml of Collagenase on a rocker for 2 hr at 37 °C. Suspension was then centrifuged for 5 min at 500x g, washed and cell pellet was re-suspended in normal growth medium (RPMI, 10% FBS, 1X anti-anti) onto a T-25 flask. After 24 hours, fresh media containing 60 μM 6-Thioguanine was added and cultured for 3 days to keep only 6-Tg resistant 4T1 cells. Isolated cells from primary tumors and metastatic organs were used for further analysis.

Analysis of breast cancer dataset

Illumina HiSeq mRNA data of patients with Breast cancer (Yau 2010) was downloaded from UCSC Xena [70] for *ESR1, PGR, ERBB2 EZH2* and *KRT14.* The breast cancer dataset was segregated into a PAM50 subtype for luminal A, Luminal B, HER2$^+$, basal and normal like subtypes and heatmap was generated.

Statistics and reproducibility

Data are presented as mean $\pm$ SEM or mean $\pm$ SD, as indicated, of at least three independent experiments or biological replicates. Two Way ANOVA, One Way ANOVA, Student's t-test and two-tailed distributions were used to calculate the statistical significance of *in vitro* and *in vivo* experiments. The Kaplan Meier survival curve significance was analysed by log rank Test. These analyses were done with GraphPad Prism software. Results were considered statistically significant when p-values ≤ 0.05 between groups. All data shown are representative of three independent experiments with similar results unless otherwise indicated.

Data Availability

Data were curated using publicly available databases such as, UCSC Xena online Browser (https://ucsc-public-main-xena-hub.s3.us-east-1.amazonaws.com/download/YauClinical_public%2FYauGeneExp_genomicMatrix.gz; Full metadata) Breast Cancer Gene Expression Minor Version V 4.8 (http://bcgenex.ico.unicancer.fr/BC-GEM/GEM-requete.php), Eukaryotic Promoter Database, TRRUST (Version 2), JASPAR (https://jaspar.genereg.net/). The RNA-seq data relevant to this study have been deposited in the Gene Expression Omnibus database under accession code GSE217474. All data needed to evaluate the conclusions in the paper are present in the paper and/or in the Supplementary Information. Additional data related to this manuscript is available in 'Source Data' File. Source data are provided with this paper.

References:

1.   Bray F, Ferlay J, Soerjomataram I, Siegel RL, Torre LA, Jemal A. Global cancer statistics 2018: GLOBOCAN estimates of incidence and mortality worldwide for 36 cancers in 185 countries. *CA Cancer J Clin* **68**, 394-424 (2018).

2.   Wolff AC*, et al.* Recommendations for human epidermal growth factor receptor 2 testing in breast cancer: American Society of Clinical Oncology/College of American Pathologists clinical practice guideline update. *Arch Pathol Lab Med* **138**, 241-256 (2014).

3.   Cheang MC*, et al.* Basal-like breast cancer defined by five biomarkers has superior prognostic value than triple-negative phenotype. *Clin Cancer Res* **14**, 1368-1376 (2008).

4.   Lehmann BD*, et al.* Identification of human triple-negative breast cancer subtypes and preclinical models for selection of targeted therapies. *J Clin Invest* **121**, 2750-2767 (2011).

5.   Chaffer CL, Weinberg RA. A perspective on cancer cell metastasis. *Science* **331**, 1559-1564 (2011).

6.   Gupta GP, Massague J. Cancer metastasis: building a framework. *Cell* **127**, 679-695 (2006).

7.   Kennecke H*, et al.* Metastatic behavior of breast cancer subtypes. *J Clin Oncol* **28**, 3271-3277 (2010).

8.   Dent R*, et al.* Triple-negative breast cancer: clinical features and patterns of recurrence. *Clin Cancer Res* **13**, 4429-4434 (2007).

9.   Holm K*, et al.* Global H3K27 trimethylation and EZH2 abundance in breast tumor subtypes. *Mol Oncol* **6**, 494-506 (2012).

10.   Karsli-Ceppioglu S*, et al.* The Epigenetic Landscape of Promoter Genome-wide Analysis in Breast Cancer. *Sci Rep* **7**, 6597 (2017).

11.   Kleer CG*, et al.* EZH2 is a marker of aggressive breast cancer and promotes neoplastic transformation of breast epithelial cells. *Proc Natl Acad Sci U S A* **100**, 11606-11611 (2003).

12.   Singh AK*, et al.* Salinomycin inhibits epigenetic modulator EZH2 to enhance death receptors in colon cancer stem cells. *Epigenetics*, 1-18 (2020).

13.   Kim KH, Roberts CW. Targeting EZH2 in cancer. *Nat Med* **22**, 128-134 (2016).

14.   Anwar T*, et al.* p38-mediated phosphorylation at T367 induces EZH2 cytoplasmic localization to promote breast cancer metastasis. *Nat Commun* **9**, 2801 (2018).

15.   Kim J*, et al.* Polycomb- and Methylation-Independent Roles of EZH2 as a Transcription Activator. *Cell Rep* **25**, 2808-2820 e2804 (2018).

16.   Moore HM, Gonzalez ME, Toy KA, Cimino-Mathews A, Argani P, Kleer CG. EZH2 inhibition decreases p38 signaling and suppresses breast cancer motility and metastasis. *Breast Cancer Res Treat* **138**, 741-752 (2013).

17.   Jiao L*, et al.* A partially disordered region connects gene repression and activation functions of EZH2. *Proc Natl Acad Sci U S A* **117**, 16992-17002 (2020).

18.   Wang J*, et al.* EZH2 noncanonically binds cMyc and p300 through a cryptic transactivation domain to mediate gene activation and promote oncogenesis. *Nat Cell Biol* **24**, 384-399 (2022).

19.   Yomtoubian S*, et al.* Inhibition of EZH2 Catalytic Activity Selectively Targets a Metastatic Subpopulation in Triple-Negative Breast Cancer. *Cell Rep* **30**, 755-770 e756 (2020).

20.   Karantza V. Keratins in health and cancer: more than mere epithelial cell markers. *Oncogene* **30**, 127-138 (2011).

21.   Cheung KJ*, et al.* Polyclonal breast cancer metastases arise from collective dissemination of keratin 14-expressing tumor cell clusters. *Proc Natl Acad Sci U S A* **113**, E854-863 (2016).

22.   Verma A, Singh A, Singh A, Chaturvedi P, Nengroo M, Datta D. Epigenetic modulator EZH2 governs CSC properties and alters metastatic cascade. In: *CANCER MEDICINE*). WILEY 111 RIVER ST, HOBOKEN 07030-5774, NJ USA (2018).

23.   Verma A*, et al.* Selective ezh2 functional activation alters the metastatic landscape of triple negative breast cancer.). AACR (2020).

24.   Burstein MD*, et al.* Comprehensive genomic analysis identifies novel subtypes and targets of triple-negative breast cancer. *Clin Cancer Res* **21**, 1688-1698 (2015).

25.   Volk-Draper LD, Rajput S, Hall KL, Wilber A, Ran S. Novel model for basaloid triple-negative breast cancer: behavior in vivo and response to therapy. *Neoplasia* **14**, 926-942 (2012).

26.   Maheshwari S*, et al.* Discovery of a Novel Small-Molecule Inhibitor that Targets PP2A-beta-Catenin Signaling and Restricts Tumor Growth and Metastasis. *Mol Cancer Ther* **16**, 1791-1805 (2017).

27.   van Haaften G*, et al.* Somatic mutations of the histone H3K27 demethylase gene UTX in human cancer. *Nat Genet* **41**, 521-523 (2009).

28.   Margueron R*, et al.* Ezh1 and Ezh2 maintain repressive chromatin through different mechanisms. *Mol Cell* **32**, 503-518 (2008).

29.   Hohmann AF*, et al.* Sensitivity and engineered resistance of myeloid leukemia cells to BRD9 inhibition. *Nat Chem Biol* **12**, 672-679 (2016).

30.   Varambally S*, et al.* The polycomb group protein EZH2 is involved in progression of prostate cancer. *Nature* **419**, 624-629 (2002).

31.   Benayoun BA*, et al.* H3K4me3 breadth is linked to cell identity and transcriptional consistency. *Cell* **158**, 673-688 (2014).

32.   Cai BH*, et al.* p53 acts as a co-repressor to regulate keratin 14 expression during epidermal cell differentiation. *PLoS One* **7**, e41742 (2012).

33.   Innocente SA, Lee JM. p53 is a NF-Y- and p21-independent, Sp1-dependent repressor of cyclin B1 transcription. *FEBS Lett* **579**, 1001-1007 (2005).

34.   Hagen G, Muller S, Beato M, Suske G. Sp1-mediated transcriptional activation is repressed by Sp3. *EMBO J* **13**, 3843-3851 (1994).

35.   Hoy SM. Tazemetostat: First Approval. *Drugs* **80**, 513-521 (2020).

36.   Rothbart SB, Baylin SBJC. Epigenetic Therapy for Epithelioid Sarcoma. *Cell* **181**, 211 (2020).

37.   Hussein YR*, et al.* Clinical and biological relevance of enhancer of zeste homolog 2 in triple-negative breast cancer. *Hum Pathol* **43**, 1638-1644 (2012).

38.   Guo S*, et al.* EZH2 overexpression in different immunophenotypes of breast carcinoma and association with clinicopathologic features. *Diagn Pathol* **11**, 41 (2016).

39.   Hirukawa A*, et al.* Targeting EZH2 reactivates a breast cancer subtype-specific anti-metastatic transcriptional program. *Nat Commun* **9**, 2547 (2018).

40.   Ma A*, et al.* Discovery of a first-in-class EZH2 selective degrader. *Nat Chem Biol* **16**, 214-222 (2020).

41.   Zhang L*, et al.* Blocking immunosuppressive neutrophils deters pY696-EZH2-driven brain metastases. *Sci Transl Med* **12**, (2020).

42.   Zhang L*, et al.* EZH2 engages TGFbeta signaling to promote breast cancer bone metastasis via integrin beta1-FAK activation. *Nat Commun* **13**, 2543 (2022).

43.   Comperat E, Bardier-Dupas A, Camparo P, Capron F, Charlotte F. Splenic metastases: clinicopathologic presentation, differential diagnosis, and pathogenesis. *Arch Pathol Lab Med* **131**, 965-969 (2007).

44.   Gengenbacher N, Singhal M, Augustin HG. Preclinical mouse solid tumour models: status quo, challenges and perspectives. *Nat Rev Cancer* **17**, 751-765 (2017).

45.   Beniey M. Peritoneal Metastases from Breast Cancer: A Scoping Review. *Cureus* **11**, e5367 (2019).

46.   Flanagan M*, et al.* Peritoneal metastases from extra-abdominal cancer - A population-based study. *Eur J Surg Oncol* **44**, 1811-1817 (2018).

47.   Bertozzi S*, et al.* Prevalence, risk factors, and prognosis of peritoneal metastasis from breast cancer. *Springerplus* **4**, 688 (2015).

48.   McDonald OG*, et al.* Epigenomic reprogramming during pancreatic cancer progression links anabolic glucose metabolism to distant metastasis. *Nat Genet* **49**, 367-376 (2017).

49.   Granit RZ*, et al.* EZH2 promotes a bi-lineage identity in basal-like breast cancer cells. *Oncogene* **32**, 3886-3895 (2013).

50.   Schwartz YB, Pirrotta V. Polycomb silencing mechanisms and the management of genomic programmes. *Nat Rev Genet* **8**, 9-22 (2007).

51.   Young MD*, et al.* ChIP-seq analysis reveals distinct H3K27me3 profiles that correlate with transcriptional activity. *Nucleic Acids Res* **39**, 7415-7427 (2011).

52.   Kolasinska-Zwierz P, Down T, Latorre I, Liu T, Liu XS, Ahringer J. Differential chromatin marking of introns and expressed exons by H3K36me3. *Nat Genet* **41**, 376-381 (2009).

53.   Pekowska A, Benoukraf T, Ferrier P, Spicuglia S. A unique H3K4me2 profile marks tissue-specific gene regulation. *Genome Res* **20**, 1493-1502 (2010).

54.   Ku M*, et al.* Genomewide analysis of PRC1 and PRC2 occupancy identifies two classes of bivalent domains. *PLoS Genet* **4**, e1000242 (2008).

55.   Tanay A, O'Donnell AH, Damelin M, Bestor TH. Hyperconserved CpG domains underlie Polycomb-binding sites. *Proc Natl Acad Sci U S A* **104**, 5521-5526 (2007).

56. Jung HR, Pasini D, Helin K, Jensen ON. Quantitative mass spectrometry of histones H3.2 and H3.3 in Suz12-deficient mouse embryonic stem cells reveals distinct, dynamic post-translational modifications at Lys-27 and Lys-36. *Mol Cell Proteomics* **9**, 838-850 (2010).

57. Peters AH*, et al.* Partitioning and plasticity of repressive histone methylation states in mammalian chromatin. *Mol Cell* **12**, 1577-1589 (2003).

58. Hon GC*, et al.* Global DNA hypomethylation coupled to repressive chromatin domain formation and gene silencing in breast cancer. *Genome Res* **22**, 246-258 (2012).

59. Aw Yong KM*, et al.* Heterogeneity at the invasion front of triple negative breast cancer cells. *Sci Rep* **10**, 5781 (2020).

60. Granit RZ*, et al.* Regulation of Cellular Heterogeneity and Rates of Symmetric and Asymmetric Divisions in Triple-Negative Breast Cancer. *Cell Rep* **24**, 3237-3250 (2018).

61. Papafotiou G, Paraskevopoulou V, Vasilaki E, Kanaki Z, Paschalidis N, Klinakis A. KRT14 marks a subpopulation of bladder basal cells with pivotal role in regeneration and tumorigenesis. *Nat Commun* **7**, 11914 (2016).

62. Gonzalez ME*, et al.* EZH2 expands breast stem cells through activation of NOTCH1 signaling. *Proc Natl Acad Sci U S A* **111**, 3098-3103 (2014).

63. McCabe MT*, et al.* EZH2 inhibition as a therapeutic strategy for lymphoma with EZH2-activating mutations. *Nature* **492**, 108-112 (2012).

64. Gulati N, Beguelin W, Giulino-Roth L. Enhancer of zeste homolog 2 (EZH2) inhibitors. *Leuk Lymphoma* **59**, 1574-1585 (2018).

65. Morin RD, Arthur SE, Assouline S. Treating lymphoma is now a bit EZ-er. *Blood Adv* **5**, 2256-2263 (2021).

66. Nengroo MA*, et al.* CXCR4 intracellular protein promotes drug resistance and tumorigenic potential by inversely regulating the expression of Death Receptor 5. *Cell Death Dis* **12**, 464 (2021).

67. Dobin A*, et al.* STAR: ultrafast universal RNA-seq aligner. *Bioinformatics* **29**, 15-21 (2013).

68. Robinson MD, McCarthy DJ, Smyth GK. edgeR: a Bioconductor package for differential expression analysis of digital gene expression data. *Bioinformatics* **26**, 139-140 (2010).

69. Subramanian A*, et al.* Gene set enrichment analysis: a knowledge-based approach for interpreting genome-wide expression profiles. *Proc Natl Acad Sci U S A* **102**, 15545-15550 (2005).

70. Goldman MJ*, et al.* Visualizing and interpreting cancer genomics data via the Xena platform. *Nat Biotechnol* **38**, 675-678 (2020).

Acknowledgments

Author Contributions Statements

AV was involved with study designing, performed experiments and wrote the draft manuscript. AS helped in carrying out *in vivo* studies. MPS performed bioinformatic analysis. MAN, KKS, ABS, PC, SRS, MAK, SM, and AKS provided active support for carrying out various *in vitro* and *in vivo* experiments. DD conceived the idea, designed experiments, analysed data, wrote the manuscript and provided overall supervision. All authors read and approved the final manuscript.

Competing Interests Statements
The authors declare that they have no conflict of interests related to this manuscript.

Figure legends
Figure 1: H3K27me3 but not NC-EZH2 protein promotes TNBC metastasis
(A) Schematic representation of EZH2 (Y641-F) and EZH2 –ΔSET retroviral overexpression constructs. (B) Immunoblot analysis for EZH2, H3K27me3, and β-actin expression in control, stable EZH2 (Y641-F), and EZH2 (ΔSET) overexpressed (OE) 4T-1 cells. (C) Tumor growth curve is shown in control, EZH2 (Y641-F) OE, and EZH2 –ΔSET OE; data are represented as mean, error bar +/- SD, left to right $^*P$ =0.0064, $^\#P$=0.0001, $^@P$=0.0025 respectively, compared to control, Two Way ANOVA, Dunnett's multiple comparisons test. (D) Average weight of harvested tumors of Control, EZH2 (Y641-F) OE, and EZH2 –ΔSET OE groups depicted by graph, (n=6) each group, data are represented as mean +/- SD, $^*P$=0.0068, compared to control, One Way ANOVA, Dunnett's multiple comparisons test. (E) The body weight curve is shown for control, EZH2 (Y641-F) OE, and EZH2 –ΔSET OE; (n=5) each group, data are represented as mean, error bar +/- SD, E: left to right $^*P$ =0.0102 and $^\#P$= 0.013 respectively, compared to control, Two Way ANOVA, Dunnett's multiple comparisons test. (F) *In-vivo* bioluminescence monitoring of orthotopic control (left panel), EZH2 (Y641-F) OE 4T-1 Luc2- GFP (middle panel) and EZH2 –ΔSET OE (right panel) primary tumor and distant metastatic sites. The colour scale indicated the photon flux (photon/ sec) emitted from each group. (G) Quantitative bar graph representation of total photon flux calculated from the region of flux (ROI), compared to control, (n=3) each group, data are represented as mean, error bar +/- SD, $^*P$=0.0021, compared to control, Two Way ANOVA, Turkey's multiple comparisons test. (H) Representative images of the wound healing assay to measure the migration ability of control and EZH2 (Y641-F) OE and EZH2 –ΔSET OE 4T-1 cells in time point manner (0-hour, 12 hour and 24 hour), magnification 10 X. (I) The quantitative analysis of wound healing assay; $^*P$=0.0001 and $^*P$=0.0002, Two Way ANOVA, Dunnett's multiple comparisons test. (J) Representative images of the trans-well chamber migration assay to measure the invasion ability of control and EZH2 (Y641-F) OE and EZH2 –ΔSET OE 4T-1 cells at 24 hours. (K) The quantitative bar graphs of tans-well chamber migration assay of control and EZH2 (Y641-F) OE and EZH2 –ΔSET OE 4T-1 cells in 24 hours. $^*P$ =0.0001 and $^\#P$ =0.0001, One Way ANOVA, Dunnett's multiple comparisons test. (L) Immunoblot analysis for UTX, EZH2, H3K27me3 and β-actin expression in control and UTX KD 4T-1 cells. (M) Representative images of the trans-well chamber migration assay to measure the invasion ability of control and UTX KD 4T-1 cells at 48 hours. (N) The quantitative bar graphs of tans-well chamber migration assay of control and UTXKD 4T-1 cells at 48 hours; $^*P$ =0.0001, Student's t-test (two–sided). (O) Immunoblot analysis for EZH2, H3K27me3 and GAPDH expression in control, EZH2 ^{OE} and EZH2 $^{-EZH1\ SET}$ HCC1806 cells. (P) Representative images of the trans-well chamber migration assay to measure the invasion ability of control, EZH2 ^{OE} and EZH2 $^{-EZH1\ SET}$ HCC1806 cells at 24 hours. (Q) The quantitative bar graphs of tans-well chamber migration assay of control and EZH2 ^{OE} and EZH2 $^{-EZH1\ SET}$ cells at 24 hours. $^*P$ =0.0001, Student's t-test (two–sided). (R) The 4T-1 cells were either treated for vehicle or 10μM EPZ6438 to analyse the expression of EZH2, H3K27me3 and β-actin by Immunoblot. (S) Representative images of trans-well chamber assay to analyse the invasion ability of control and EPZ6438 (10 μM) treated 4T-1 cells. (T) The quantitative bar graphs of tans-well chamber migration assay of

control and EPZ6438 (10 μM) at 48 hours. $^{*}P$ =0.0006, Student's t-test (one–sided). In I, K, N, Q, and T, Columns are mean of triplicate readings; error bar +/- SD. P values are calculated as compared to control. Source data are provided as a Source Data file.

Figure 2: Functional hyper-activation of EZH2 (increased H3K27me3) leads to TNBC splenic metastasis

(A) Schematic representation for generation of control Td-Tomato^{+} and H3K27me3^{High} (Y641-F) GFP $^{+}$ 4T-1 cells by retroviral transduction (Upper panel). The schematic delineation of different strategies used in the *in-vivo* studies (Lower panel). (B-C) Live fluorescence imaging of primary tumors and distant metastatic sites were shown under different strategies (described in Methods, Animal studies section). The excitation and emission wavelength: Td-Tomato- 570-620 nm and GFP-465-520 nm. (D) The fluorescence imaging of harvested control (Td-Tomato^{+}) and EZH2 Y641-F (GFP $^{+}$) primary tumors at a specific wavelength (upper panel). The metastatic potential of control (Td-Tomato^{+}) and EZH2 Y641-F (GFP^{+}) cells were analysed by fluorescence imaging in the harvested organs at a specific wavelength (lower panel). (E) The fluorescence images of single-cell harvested from both tumors control (Td-Tomato^{+}) and EZH2 Y641-F (GFP^{+}) and harvested organs (n=3). Scale bar 50 μm. (F) Representative flow cytometry-derived scatter plots showing control (Td-Tomato^{+}) and EZH2 Y641-F (GFP^{+}) cells in primary tumors and metastatic organs harvested from mice (n=3). (G) The quantitative analysis of the percentage of Control (Td-Tomato^{+}) and EZH2 Y641-F (GFP^{+}) cells in harvested primary tumors and metastatic organs (n=3), data are represented as mean, error bar +/- SD, $^{*}P$ =0.0120 and $^{#}P$ = 0.00484, respectively, compared to Td-Tomato group, Two Way ANOVA, Sidak's multiple comparisons test. (H) Photomicrographs of H&E staining in the lung, liver, and spleen of control and Y641-F tumor-bearing mice. Scale bar 50 μm. (I) Photomicrographs of metastatic cells isolated form the peritoneal fluid of Y641-F tumor bearing mice under bright field (extreme left) and GFP fluorescence (middle left) panels respectively. Scale bar 50 μm. The excitation and emission wavelength: GFP-465-520 nm. Colony formation assay was carried out in metastatic cells isolated form the peritoneal fluid of Y641-F tumor bearing mice, stained with crystal violet and photo-micrographic images were taken under bright field (middle right) and inset (extreme right) panels. Source data are provided as a Source Data file.

Figure 3: Transcriptome analysis revealed that overexpression of EZH2 catalytic function (elevated H3K27me3) increases *KRT14* transcription

(A) The schematic representation of experimental planning. (B) The immunoblot analysis of EZH2, H3K27me3 expression in 4T-1 cells harvested from primary tumor and metastatic organs; GAPDH was used as loading control. (C) The *in-vivo* imaging of mice having primary tumor and splenic metastatic cell inoculation (n=5). The colour scale indicated the photon flux (photon/ sec) emitted from each group. (C) Quantitative bar graph representation of total photon flux calculated from the region of flux (ROI), data are represented as mean, error bar +/- SD, $^{*}P$=0.0038, compared to primary tumor, Two Way ANOVA, Sidak's multiple comparisons test. (D) The Kaplan-Meier survival curve of mammary tumor onset in the nude mice with inoculation of primary tumor and spleen metastatic cells (n=6). $^{*}P$=0.0150, compared to primary tumor, log-rank test. (E) Volcano plot represents the significant differential expression of genes between control and Y641-F cells. Red and blue dots represent the up-regulated and down-regulated genes with (Log$_2$FC +1, -1 and p<0.05) respectively. (F) Heat map of top 100 ranked genes differentially expressed between control and Y641-F phenotype. Expression values are represented as colors, where the range of colors (red, pink, light blue, dark blue) shows the range of expression values (high, moderate, low, lowest), respectively. (G) Heat map shows differential expression of cell migration and metastasis related genes between control and Y641-F. (H) RNA was isolated from control and EZH2 Y641-F 4T1 cells and subjected to real time-PCR for gene expression analysis. Data points are mean of triplicate readings of samples; error bars, ± S.D,

$^{*,#}P$=0.0001, $^{@}P$=0.0134, $^{$}P$=0.001, $^{\%,+,\&,^}P$=0.0001, Two Way ANOVA, Sidak's multiple comparisons test. (I) RNA was isolated from 4T1 cells isolated from primary tumor, metastatic lung, liver and spleen and subjected to real time-PCR for gene expression analysis. Data points are mean of triplicate readings of samples; error bars, ± S.D, Left Panel, $^{*}P$=0.0162, $^{#}P$=0.0101, ^{X}P=0.0031, $^{@}P$=0.0002, $^{$}P$=0.0065, $^{\%}P$=0.0039, ^{+}P=0.0001, $^{\&}P$=0.001, $^{^}P$=0.0001, Right Panel, $^{*}P$=0.0001, $^{#}P$= 0.0009, $^{@}P$=0.0001, $^{$}P$=0.0088, $^{\%}P$=0.0009 and ^{+}P=0.0493, compared to isolated cells from primary tumors, Two Way ANOVA, Dunnett's multiple comparisons test. Source data are provided as a Source Data file.

Figure 4: H3K27me3 level positively regulates the expression of KRT14 in mRNA and protein level

(A) Immunoblot analysis for EZH2, H3K27me3, β-actin in control and EZH2 ^{OE} HCC1806 cells. (B) Control and EZH2 Y641-F cells were analysed for expression of EZH2, H3K27me3, KRT14 and β-actin by Immunoblot. (C) Immunoblot analysis for EZH2, H3K27me3, β-actin in control and EZH2 ^{EZH1SET} HCC1806 cells. (D) The control and EZH2 Y641-F cells were treated with 10μM dose of EPZ6438 and performed q-PCR analysis for *KRT14* expression. Data points are mean of triplicate readings of samples; error bars, ± S.D, compared to control $^{*}P$=0.0001 and Y641-F $^{#}P$=0.0001 respectively, One Way ANOVA, Turkey's multiple comparisons test (E) The control and EZH2 Y641-F cells were treated with 10μM dose of EPZ6438 and analysed for expression of EZH2, H3K27me3, KRT14 and β-actin by immunoblot. (F) The vehicle control and Tet-ON EZH2-YFP OE HCC1806 cells were analysed for expression of EZH2 WT, EZH2-YFP, H3K27me3, KRT14 and β-actin by immunoblot. (G) The HCC1806 cells were treated either for vehicle control or 10μM dose of EPZ6438 for the analysis of the expression of *KRT14* by RT-q PCR. Data points are mean of triplicate readings of samples; error bars, ± S.D, $^{*}P$=0.0001 compared to control cells, student's t-test (Two -sided). (H) The HCC1806 and MDAMB468 cells were either treated for vehicle or 10μM EPZ6438 to check the expression of EZH2, H3K27me3, KRT14 and β-actin by immunoblot. (I) HCC-1806 cells were treated with either vehicle or 10 μM EPZ6438 treatments for 24 hours, co-stained with H3K27me3 (red) and KRT14 (green) antibodies and analysed under confocal microscope. Scale bar, 50 μm. (J-K) 4T1 cells were isolated from primary tumors and metastatic spleen and subjected to confocal analysis after having either co-staining (J) with H3K27me3 (red) and KRT14 (green) or single (K) staining with Ki-67 (red) antibodies. In both the cases, DAPI was used stain the nuclei. Scale bar 20 μm and 5 μm. Source data are provided as a Source Data file.

Figure 5: H3K27me3 occupancy in the *KRT14* promoter is linked with active transcription

(A) Diagrammatic scheme showing genomic location of *KRT14* gene for both mouse and human. (B) ChIP was performed in 4T-1 mouse cells using anti-H3K27me3, p-Pol-II-S5 and IgG antibodies and then examined by real-time q-PCR using primer pairs targeting -1.5 Kb to -0.2 Kb of the *KRT14* gene (C) Same procedure for HCC1806 human cells as in B. (D and E) the differential fold change enrichment for H3K27me3 and p-Pol-II-S5 were observed in -0.2Kb and -0.5 Kb regions from TSS in control and EZH2- Y641-F cells by ChIP q-PCR. (F) The differential fold change enrichment for H3K27me3 and p-Pol-II-S5 were analysed in -0.2Kb region from TSS in the HCC1806 cells treated either with vehicle control or 10μM EPZ6438. (G) ChIP was performed in 4T-1 mouse cells using anti-H3K4me3 and IgG antibodies and then examined by real-time q-PCR using primer pairs targeting -1.1 Kb to +2.4 Kb of the *KRT14* gene (H) Same procedure for HCC1806 human cells as in G. (I) the differential fold change enrichment for H3K4me3 +2.4 Kb region from TSS in control and EZH2- Y641-F 4T1 cells by ChIP q-PCR. (J) The differential fold change enrichment for H3K4me3 was analysed in +2.4 Kb region from TSS in the HCC1806 cells treated either with vehicle control or 10μM EPZ6438. B-F; Columns, are mean of quadruplicate readings of samples; error bars, ± S.D, B and C: compared to IgG control, left to right, $^{*}P$ =0.0158, $^{#}P$ =0.0001, $^{\%}P$ =0.0003, $^{$}P$ =0.0001, $^{\&}P$ =0.0001 and $^{@}P$ =0.0004, Two

Way ANOVA, Sidak's multiple comparisons test. D-F: compared to control, left to right, $^*P$ =0.0029, $^\#P$ =0.0025, $^\$P$ =0.0022, $^\&P$ =0.0024, $^\%P$ =0.0036 and ^+P =0.0134, Two Way ANOVA, Turkey's multiple comparisons test. G-I; Columns, a mean of duplicate readings of samples, error bars, ± S.D, G-H: compared to IgG control, left to right, $^*P$ =0.0023 and $^\#P$ =0.0001, Two Way ANOVA, Sidak's multiple comparison test. I: compared to VC, $^*P$ =0.0001, Two Way ANOVA, Turkey's multiple comparisons test. J: Columns, a mean of triplicate readings of samples, error bars, ± S.D, compared to VC, $^\#P$ =0.0082, Two Way ANOVA, Turkey's multiple comparisons test. Source data are provided as a Source Data file.

Figure 6: H3K27me3 enrichment in the *KRT14* promoter attenuates SP1 binding and promotes *KRT14* expression

(A) Diagrammatic representation of SP1 binding motif obtained from JASPAR database for mouse (left) and human (right). (B) The human nucleotide sequence for *KRT14* promoter with TATA and GC-box. (C-D) The *KRT14* mRNA expression was analysed in the control and *SP1* KD HCC1806 (C) and 4T1 (D) cells by qRT-PCR. left to right, compared to control, $^*P$ =0.0002, $^\#P$ =0.0030, $^\$P$ =0.0001 and $^\%P$ =0.0053, student's t test (two- sided). (E) The control and Y641-F cells were analysed for SP1 and GAPDH by immunoblot. (F) The control and SP1 KD 4T-1(Y641-F) cells were analysed for SP1, KRT14 and β-actin expression by immunoblot. (G) Control and SP1 KD HCC1806 cells were analysed for SP1 and β-actin protein expression by immunoblot (Left panel) and the control and SP1 KD cells were analysed for luciferase activity followed by the transfection of -1.1 Kb and -0.5 Kb *KRT14* promoters (right panel). G: right panel, compared to control, $^\wedge P$ =0.0010 and $^@P$ =0.0005, Two Way ANOVA, Sidak's multiple comparisons test. (H) The HCC1806 cells were treated either with vehicle or 150nM or 300nM of mithramycin and subjected to immunoblot analysis for SP1 and β-actin (Left Panel). Relative luciferase activity was measured as described in Methods section and represented in right panel. H: right panel, compared to control, $^\&P$ =0.0289 and ^+P =0.0201, Two Way ANOVA, Dunnett's multiple comparisons test. (I) ChIP q-PCR data showing the recruitment of SP1 (left panel), p-Pol-II-S5 (middle panel), and H3K27me3 (right panel) on the *KRT14* promoter upon EPZ6438 (10µM) treatment in HCC1806 cells. I: left to right, compared to control, ^XP =0.0052, ^YP =0.0097, and ^ZP =0.0011, Two Way ANOVA, Sidak's multiple comparisons test. In, C, D, G (right), H (Right) and I, Columns represent a mean of triplicate readings of samples, error bars, ± S.D. J, Pictorial representation illustrating how H3K27me3 inhibits the SP1 binding to the promoter of *KRT14* gene and activate its transcription. Source data are provided as a Source Data file.

Figure 7: Genetic knock down of *KRT14* inhibits splenic metastasis

(A and B) The *KRT14* knock down was confirmed through immunoblot by using two different shRNA in 4T-1 and HCC1806 cells. The β-actin used as a loading control. (C-F) Representative images of the wound healing assay to measure the migration ability of control and *KRT14* KD in 4T-1 (C) and HCC1806 (E), magnification 10 X. (D, F) The quantitative analysis of wound healing assay. Columns, a mean of quadruplicate readings of samples; error bar, +/- SD, $^*P$ =0.0001 and $^\#P$ =0.0001, compared to control, Two Way ANOVA, Sidak's multiple comparisons test. (G-J) Representative images of the trans-well chamber migration assay to measure the invasion ability of control and *KRT14* KD 4T-1 (G) and HCC1806 (I) cells at 24 hours. The quantitative bar graphs of trans-well chamber migration assay of control and *KRT14* KD 4T-1 (H) and HCC1806 (J) cells are shown. Columns represent a mean of triplicate readings of samples, error bars, ± S.D. compared to control, $^\$P$ =0.0002, $^\%P$ =0.0058, Student's t-test (two- sided). (K) Fluorescence imaging of metastatic cells harvested from spleen (n=5). The Td-Tomato fluorescence is for control cells and GFP fluorescence is for *KRT14* KD (Left panel). Scale bar 50µm. The excitation and emission wavelength: Td-Tomato- 570-620 nm and GFP-465-520 nm. (L) The quantitative analysis for the metastatic control (Td-Tomato$^{+)}$ and *KRT14* KD (GFP$^+$) cells harvested from spleen (n=5, three different fields from each spleen), Columns, a mean of fifteen

readings of samples, error bar, +/- SD, $^{\&}P$ =0.0001, compared to Td-Tomato, Student's t-test (two- sided). (M) Representative flow cytometry-derived scatter plots showing control (Td-Tomato$^+$) and EZH2 Y641-F (GFP$^+$) metastatic cells harvested from spleen (n=5). (N) The quantitative analysis of the percentage of Control (Td-Tomato$^+$) and *KRT14* KD (GFP$^+$) metastatic cells harvested from spleen (n=5) Columns, a mean of five readings of samples, error bar, +/- SD, $^{@}P$ =0.0001, compared to Td-Tomato, Student's t-test (two- sided). Source data are provided as a Source Data file.

Figure 8: H3K27me3 and KRT14 levels are significantly increased in human TNBC metastasis

(A) Analysis of *EZH2* and *KRT14* transcript levels on the basis of ESR1, PGR, ERBB2 expression in different PAM50 subtypes represented in a heat map. Data is retrieved from Breast Cancer (Yau 2010) data set, publicly accessible via XENA USSC Cancer Genome Browser. (B) Representative of heat map in the form of box and Whiskers plot for Breast Cancer (Yau 2010) PAM50 subtypes, Normal (Brown) n=66, ESRI s.d.=1.01, mean=-0.26, PGR s.d.= 2.35, mean= 0.474, ERBB2s.d.=1.41, mean=-0.212, EZH2 s.d.= 0.80, mean= -.505 and KRT14 s.d=2.33, mean=2.76. Luminal B (sky blue) n=139, ESR1 s.d.=0.39, mean=0.071, PGR, s.d.= 2.44, mean=0.155, ERBB2 s.d.=1.36, mean=-0.420, EZH2 s.d. =1.20, mean=0.366, KRT14 s.d=2.47, mean=-2.28.Luminal A n=222, ESR1 s.d.=0.45, mean= -0.301, PGR s.d.= 2.27, mean=1.26, ERBB2 s.d.=1.43, mean=-0.195, EZH2 s.d.=0.725, mean=-0647 and KRT14 s.d.= 2.80, mean=0.752. HER+ n=102, ESR1 s.d. = 1.70, mean=-1.842, PGR s.d. =1.56, mean=-1.48, ERBB2, s.d. =2.59, mean=3.29, EZH2 s.d. =0.78, mean=0.303 and KRT14 s.d. =2.79, mean=-1.906. Basal n=170, ESR1s.d. =1.80, mean=-2.76, PGR s.d. =0.791, mean=-1.54, ERBB2 s.d. =2.50, mean=-1.18, EZH2 s.d. =0.98, mean=1.97 and KRT14 s.d. =3.42, mean=1.45. Whiskers for the plot signify SD and the bar denotes the mean for each subtype, where the box extends from 25th–75th percentile and whiskers ranges from minimum and maximum value, with centre denotes the median value (C) Correlation plot showing IHC co-expression of the EZH2 and KRT14 in breast cancer TNBC subtype. Pearson pairwise correlation coefficient on 897 TNBC samples shows positive correlation (r=0.10) between EZH2 and KRT14 and significantly associated with each other (p=0.0018). (D) Immunohistochemistry was carried out to detect EZH2, H3K27me3 and KRT14 in FFPE serial sections of matched human TNBC primary tumor and respective metastatic counterparts using anti-EZH2, anti-H3K27me3, and anti-KRT14 antibodies. Representative photomicrographs were shown at 10X and 40X magnifications (inset). Scale bar, 200 μm (10X) or 50 μm (40X). (E-G) Quantitative H-scores for TNBC primary tumors and metastatic counterparts (n=10) were calculated for EZH2 (E), H3K27me3 (F) and KRT14 (G) expression and represented as scatter plots; error bar, +/- SD, left to right $^{*}P$=0.0047, $^{#}P$=0.046, compared to expression in respective primary tumors, Student's t test (Two-sided). Source data are provided as a Source Data file.

Figure 9: Inhibition of EZH2 methyltransferase activity reduces TNBC peritoneal metastasis

A) Immunoblot for EZH2, H3K27me3 and β-actin expression in Control and EZH2 knockdown (KD) 4T-1 cells. (B-E) Representative images of the wound healing (B) and trans-well chamber migration (D) assays in control and EZH2 KD 4T-1 cells, 10X magnification. The quantitative analysis of wound healing (C) and trans-well (E) assay; Columns, mean of triplicate readings of samples, error bar, +/- SD, compared to control, $^{*}P$=0.0453, Two-way ANOVA, Sidak's multiple comparisons test and $^{#}P$=0.0467 student's t-test (two-sided). (F) Bioluminescence image of tumor bearing control (Top panel), EZH2 KD (bottom panel) mice. The colour scale indicated the photon flux (photon/ sec) emitted from each group. (G) Quantitative bar graph representation of total photon flux calculated from the region of flux (ROI). Columns, a mean of quadruplicate readings of samples, error bar, +/- SD, $^{\$}P$=0.0010 compared to control, Two-way ANOVA,

Sidak's multiple comparisons test. (H) Bioluminescence images of liver and spleen harvested from control and EZH2 KD tumor bearing mice. (I) The Kaplan-Meier survival curve of control and EZH2 KD 4T1 tumor bearing mice cells (n=10), $^{\%}P$=0.0001, compared to control, log-rank test. (J-M) Representative images of the wound healing (J) and trans-well chamber migration (L) assays in 4T1 EZH2Y641-F (control) and EPZ6438 (10μM) treated cells, 10X magnification. The quantitative analysis of wound healing (K) and trans-well (M) assay; Columns, a mean of duplicate (K) and triplicate (M) readings of samples, error bar, +/- SD, compared to control, $^{\&}P$=0.0158, $^{\wedge}P$=0.0219, ^{X}P =0.0011, ^{Y}P=0.0001, Two-way ANOVA, Sidak's multiple comparisons test. (N) Representative bioluminescence images of EZH2 (Y641-F) 4T1 tumor bearing mice, treated with either vehicle or EPZ6438 (250mg/Kg). (O) Quantitative bar graph representation of total photon flux calculated from the region of flux (ROI); Columns, a mean reading of triplicate samples, error bar, +/- SD, ^{Z}P=0.0078, compared to control, Two-way ANOVA, Sidak's multiple comparisons test. (P) The bioluminescence analysis of metastatic signal in the organs harvested from control (Y641-F) and EPZ6438 treated mice. (Q) The Kaplan-Meier survival curve of nude mice, either treated with vehicle control (n=5) or EPZ6438 (250mg/Kg) (n=5). $^{@}P$=0.0326, compared to vehicle control, log-rank test. Source data are provided as a Source Data file.

Figure 10: Schematic representation of how catalytically hyperactive EZH2 (increased H3K27me3) can promote TNBC peritoneal metastasis and its therapeutic vulnerabilities against EZH2 inhibitor EPZ6438

Smac Mimetic PCT Filing Details

Patent Title: SMAC MIMETICS FOR TREATMENT OF CANCER, PROCESS FOR PREPARATION AND PHARMACEUTICAL COMPOSITION THEREOF (**Patent Link: https://patentscope.wipo.int/search/en/detail.jsf?docId=WO2022130411&_cid=P10-L50LD3-74541-1**)

Principal Investigator: Dr. Dipak Datta

Publication Number: WO/2022/130411, **Publication Date: 23.06.2022**, International Application No.PCT/IN2021/051182, International Filing Date:17.12.2021

Name of Other Contributors: Haq W, Ali R, Singh A, Nengroo MA, Katekar R, Singh G, Vaishnav J, Afsar M, Singh M, Rath SK, Koley D, Mishra DP, Ramachandran R, Ampapathi RS, Gayen JR

Patent Abstract:

The present invention relates to novel SMAC mimetic peptidomimetics useful for the treatment of proliferative diseases including cancer in mammals. The novel SMAC mimetics are prepared by incorporating (2S,5R)-5-(5-methylfuran-2-yl)pyrrolidine-2-carboxylic acid, a novel unnatural amino acid that imparts exclusively trans amide bond geometry favourable for target protein binding. Here, the novel SMAC mimetic molecule(s) not only show its efficacy in varied cancer types but also demonstrate in vitro and in vivo efficacy against therapy resistant cancer as a single agent. The novel SMAC mimetics disclosed in the present invention binds to BIR-2 and BIR-3 domains of the XIAP and exhibit high anti-proliferative activity against variety of mammalian cancer cell lines that include but not limited to chemotherapy and TRAIL resistant cell lines.

Field of invention:

The present invention is related to SMAC (Second Mitochondria-derived Activator of Caspase) mimetic compounds useful for treatment of proliferative disorder including cancer.

Background of the invention:

Evasion of apoptosis or 'programmed cell-death' is one of the hallmarks of human cancer. Therefore, restoration or induction of apoptosis in cancer cells is an attractive therapeutic strategy. There are multiple endogenous cellular counter acting proteins that regulate intricate balance between cell death and survival. One of the classical examples of such reciprocal regulation within cell is the interaction between SMAC and IAP. The SMAC is a pro-apoptotic protein, sensitizes cells to apoptosis in cancerous cells by antagonizing the activity of lAPs. Therefore, SMAC mimetics have been found as a novel and targeted therapeutic approach to treat cancer (Abraha et.al, World J Gastrointest Oncol. Aug 15, 2016; 8(8): 583-591). Currently, multiple clinical trials are ongoing for different SMAC mimetics against various cancer types demonstrating its immense importance in cancer therapeutics (Fulda et.al., Clinical Cancer Research. Volume 21, Issue 22, 2015. 5030-5036).

The Inhibitors of Apoptosis Proteins (lAPs) are naturally occurring intra-cellular proteins that suppress caspase-dependent apoptosis. lAPs are the key negative regulators that inhibit the distinct caspases which are critical for initiation and execution of apoptotic pathways. There are eight members in the mammalian IAP family. Among these X-chromosome-linked IAP (XIAP) is perhaps the best characterized member of lAPs family that is known to play a direct role in the regulation of apoptosis. XIAP bind to caspase-3 and caspase-7 via its BIR2 domain and the preceding linker region, respectively. In addition, XIAP also binds to caspase-9 via its BIR3 domain, thereby blocking the dimerization and subsequent activation of caspase-9. Given that fact caspase-3 and -7 play a major role in the implementation of apoptosis in both the extrinsic and intrinsic pathways, and caspase-9 is a critical initiator caspase in the intrinsic pathway, XIAP

is the most preferable target to revive the apoptosis. SMAC is the naturally available antagonist of IAP proteins. SMAC is released from the mitochondria into the cytosol upon apoptotic signalling and binds to the BIR3 domain of XIAP via conserved IAP -binding motif (IBM) which contains four amino acid residues (AVPI) that is exposed at the amino-terminus of the mature processed SMAC protein and prevent the interaction of XIAP with caspases (Cong et.al., J. Med. Chem. 2019, 62, 5750 5772).

In addition, Smac also binds to the BIR3 domain of cIAPl and cIAP2 and as a result enhances their E3 ligase activity which promotes the auto-ubiquitination and proteasomal degradation of cIAPl and cIAP2. Several small molecule mimetics of AVPI, termed IAP inhibitors are being advanced in clinical trials for the treatment of cancer. The LCL-161 and AT-406 are structurally monovalant whereas Birinapant/TL32711 is a bivalent are among the prominent ones under development.

The major approach used for the designing the SMACs are focussed on the synthesis of conformationally constrained compounds where Xxx-Pro bond is preferably in trans geometry. Yet another consideration was undertaken is the balance of lipophilicity at the C-terminal end or of the linkers for the bivalent molecules. Several efforts are made in the past for the evolution of Smac AVPI tetrapeptide to develop bioavailable Smac mimetics by systematically examination of the role and tolerance to substitution of each amino acids of AVPI (1) peptide.

A library of tetrapeptides using the N- terminal of Smac are prepared with a novel strategy to control trans geometry around the proline residue as a starting point. They replaced the position of each one of the four amino acids with all the natural amino acids. It is found that alanine residue at position 1 of the tetrapeptide is very crucial for activity and binding is greatly diminished if alanine is replaced with any natural amino acids.

Therefore, there is a need in the art for new compounds, which are capable of restoring or inducing apoptosis in cancer cells for treatment of cancer.

Objectives of the invention:

The main objective of the present invention is to develop peptide SMAC mimetics useful as monotherapy as well as in combination with available anti-cancer drugs as safe and effective therapy against various types of cancer.

Another objective of the invention is to develop a process for the synthesis of SMAC mimetics.

Yet another objective of the present invention is to develop formulations of SMAC mimetics suitable for human application.

Still another objective of the present invention is treatment of cancer using SMAC mimetics.

Another objective of the present invention is to provide targeted therapy against treatment resistance cancer by using SMAC mimetics.

Yet another objective of the present invention is to provide SMAC mimetic or IAP antagonist or IAP inhibitor having the capability to potently bind both BIR-2 and BIR-3 domains of XIAP/IAP and having significant bioavailability with robust in-vitro and in-vivo efficacy against therapy resistant refractory cancers.

Data Details: Here are the details of Patent Filing data enlisted as a preliminary data work package

Figure 1: Clinical Positioning & Target Product Profile (TPP): Smac Mimetic/XIAP/IAP antagonist
Figure 2: Synthetic Step comparison with Clinical comparators
Figure 3: S016-1348-Target Binding with XIAP-BIR2/BIR3
Figure 4: Superiority over existing Comparators (2D assays)
Figure 5: Superiority over existing Comparators (3D assays)

Study Highlights:
a) Orally active, monovalent XIAP antagonist exhibits anti-tumor efficacy as a single agent
b) nM level target binding with nM level in vitro efficacy against chemotherapy resistant cancer cells.
c) Oral Bioavailability: 55% (mice), Rat (20%), Dog (50%)
d) Better preclinical efficacy and bioavailability than existing Phase-II clinical trial comparator (Novartis LCL-161)
e) Detailed molecular mechanisms deciphered for its mode of action
f) Efficacy dose-2.5mg/kg in mice, NOAEL: 150mg/kg in 7-Day DRF in Rat
g) IND studies on-going

IND enabling studies of Smac mimetic (S016-1348) as a potential cancer therapeutic

Preliminary Data Package

CSIR – Central Drug Research Institute, Lucknow

| Indication	Solid Tumors such as Colon, TNBC, Head & Neck Cancer
Target population	Must demonstrate anti-proliferative efficacy against tumor cell lines having an $IC_{50}<10\mu M$, having 5X safety margin in non-human cells, Target overexpression should achieve 10 fold IC_{50} increase.
Mechanism	Cell free assay should show binding of BIR2/3 domains of XIAP/IAP at nM range (Comparator LCL161, Birinapant) Cell based assay system should demonstrate Target degradation and Caspase cleavage at cellular IC_{50} dose (Comparator: LCL161, Birinapant)
Efficacy- proposed targets to be attained	In vivo efficacy to be determined at multiple doses in xenograft models with measurements of tumor size, body weight, and (metastatic flux, % mice survival in case of metastatic model) Comparator: LCL161, Birinapant
Safety	28-day repeat dose toxicity initially to establish at least a 5X window between the highest efficacious dose and the NOAEL Additional toxicity studies will be required prior to Phase 2 Comparator: LCL161, Birinapant
Route of administration	Oral bioavailability above 30%
Pharmacokinetics	PK suitable for once or twice a day dosing
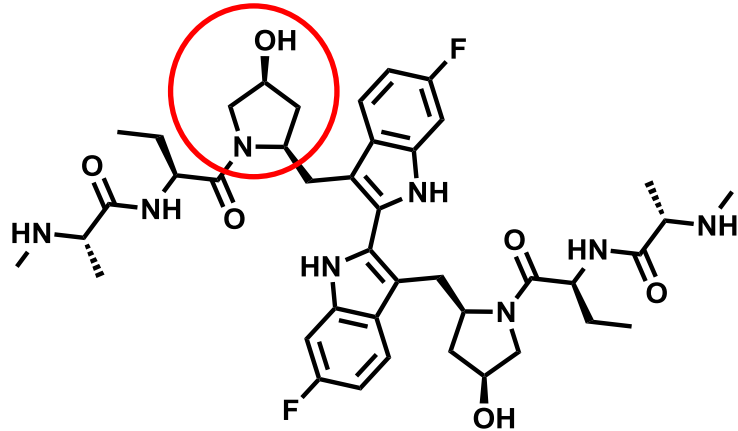
Birinapant (TL32711)

Merck, 15 steps
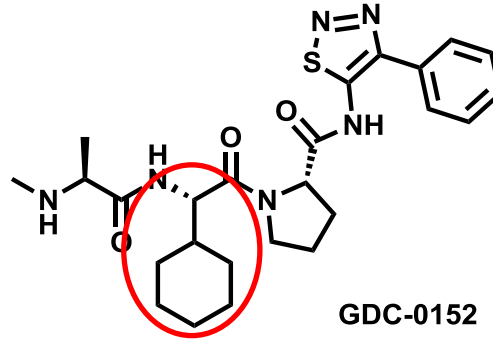
GDC-0152

Genentech, 11 steps
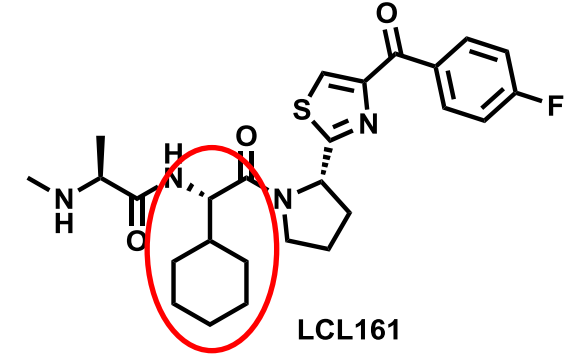
LCL161

Novartis, 11 steps

S-016-1348

CSIR-CDRI, 11 steps
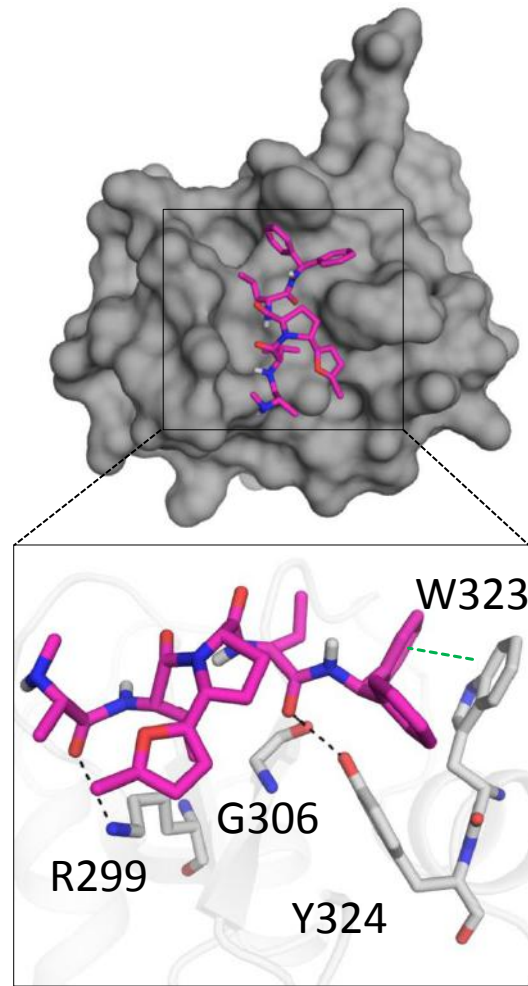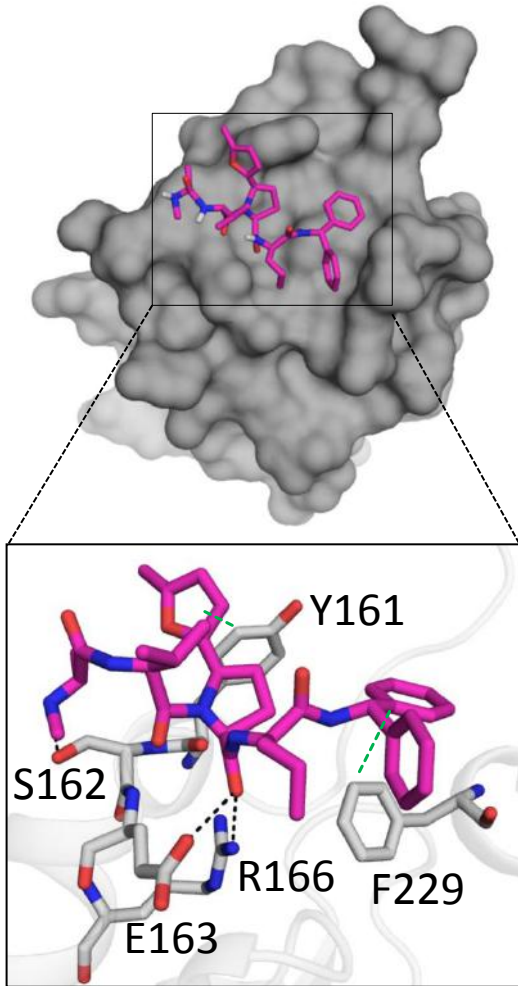
PCT/IN2021/051182, Date of Filing: 17-Dec-2021

BIR2-S016-1348

BIR3-S016-1348

Compound	BIR2	BIR3
S016-1348	-6.2 Kcal/mol	-6.4 Kcal/mol

> The analysis of contributing residues responsible for the stabilization of S016-1348 on BIR2 shows the active role of **S162, E163** and **R166** via hydrogen bonds while **Y161** and **F229** making base stacking interactions.

> Furthermore, the analysis of binding pocket of BIR3 displays that **Y324, R299** and **G306** are forming the hydrogen bonds and **W323** residues shows base stacking interaction in the stabilization of HD-1348 compound.

FPA Data: XIAP-BIR2-Kd:330nM, XIAP-BIR3 Kd: 142nM

Molecular Interaction studies with Target Confirmed by NMR and Chemical Shift Perturbation Assay

Compound	SW-620 IC$_{50}$ (µM)	HCT-116 IC$_{50}$ (µM)	HT-29 IC$_{50}$ (µM)
S016-1348 (CSIR-CDRI-Smac)	**2.7**	**7.5**	**3.3**
LCL-161 (Novartis-Smac)	74.52	67.41	81.01
AT-406 (Debiopharm-Smac)	> 100	> 100	> 100
Birinapant (Merck-Smac)	78.93	> 100	> 100

48 hour Cytotoxicity Determination by SRB Assay

S016-1348 is better than all Phase-II clinical trial Smac mimetics
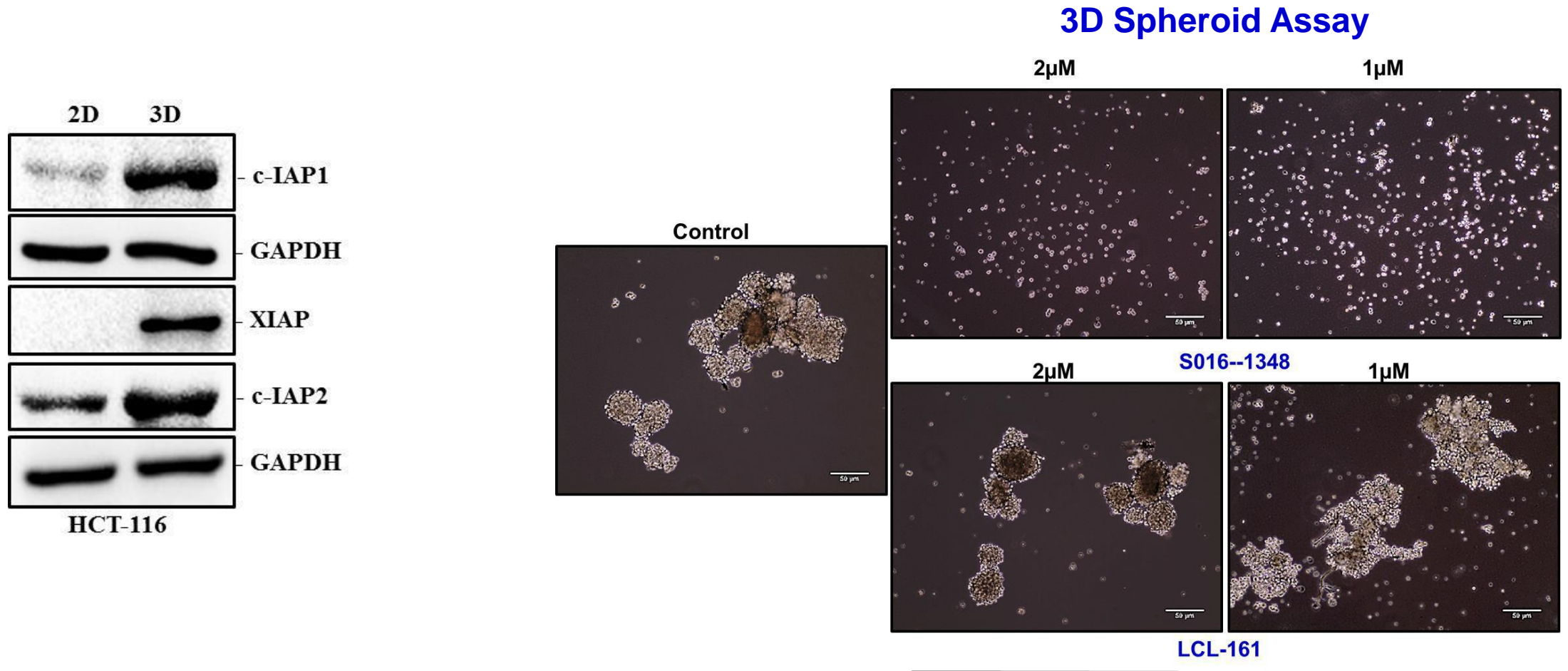
S016-1348 inhibits 3D colon tumor cell growth more efficiently than Novartis Smac mimetic LCL-161
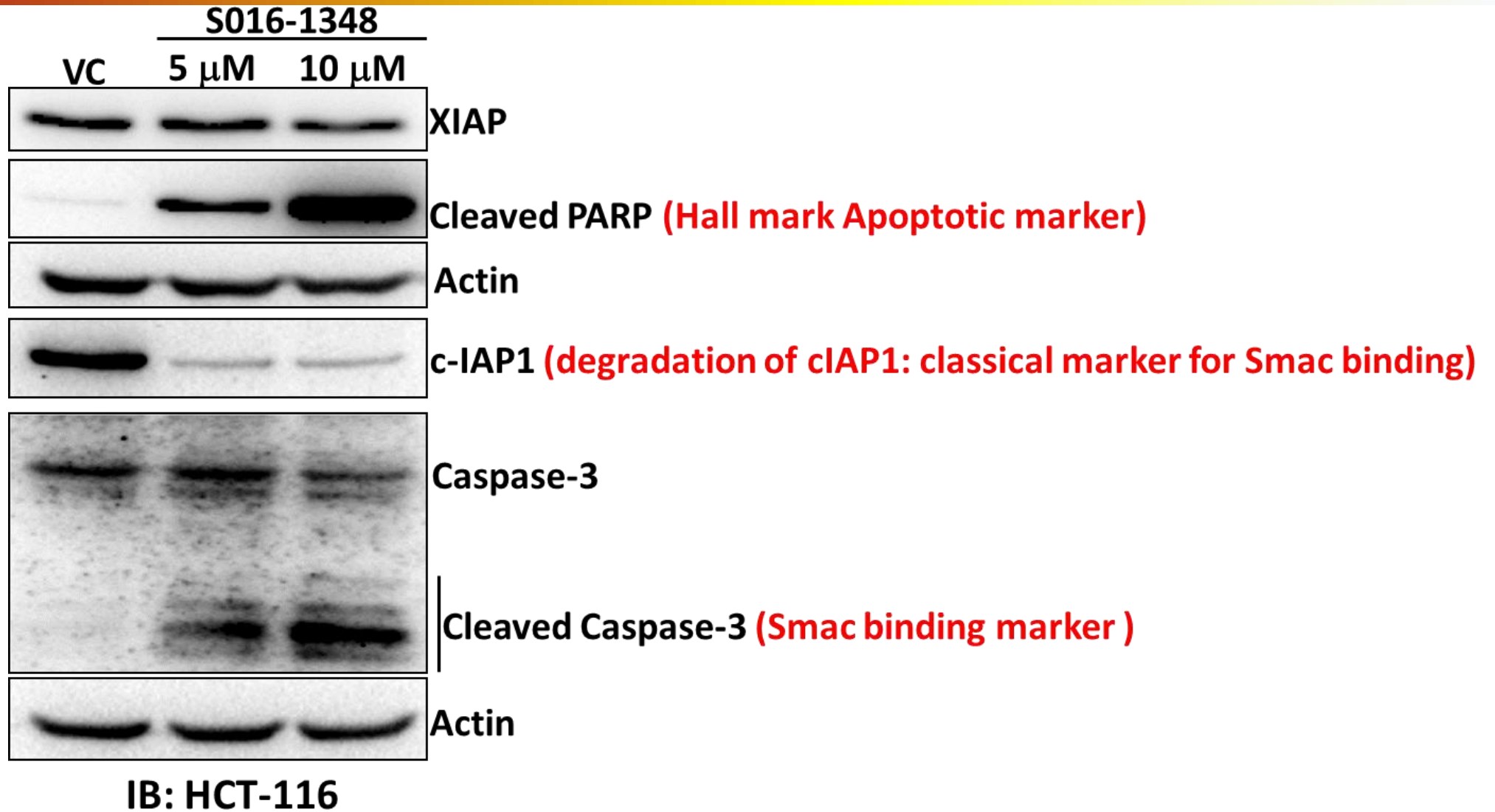
S016-1348 proficiently engages its cellular targets and activates hall mark apoptotic features
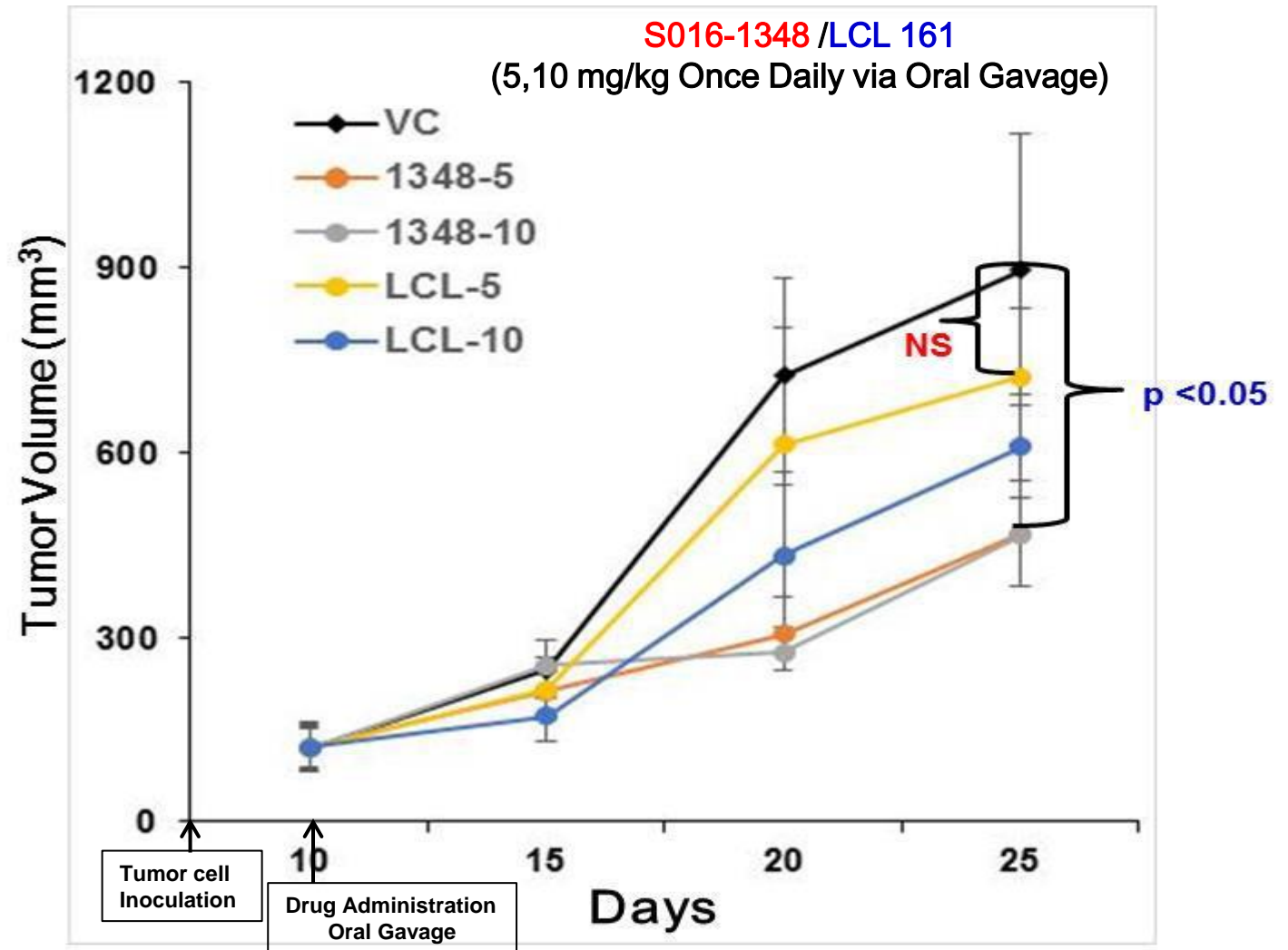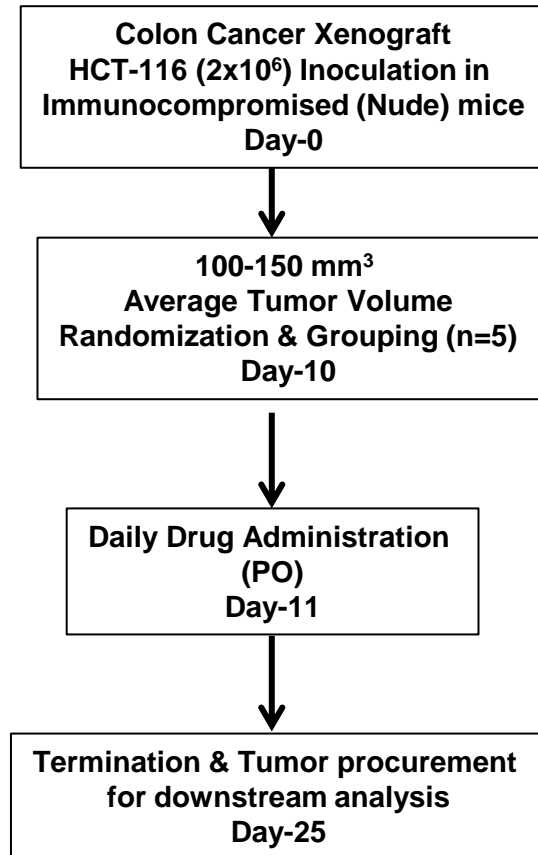
Figure 7: Bioavailability of S016-1348 in mice

| Parameter (Unit)	IV route (4 mg/kg)	SC route (30 mg/kg)	Oral route (30 mg/kg)
C_{max} (ng/mL)	10215 ± 2633.37	5018.33 ± 853.66	4490.00 ± 1514.05
$AUC_{0-\infty}$ (h*ng/mL)	4107.24 ± 852.34	17439.13 ± 2220.28	17227.95 ± 3433.39
T_{max} (h)	0.08	0.88 ± 0.21	1.08 ± 0.47
$T_{1/2}$ (h)	0.19 ± 0.05	2.10 ± 0.15	3.84 ± 1.80
Cl (L/hr/Kg)	1.02 ± 0.24	1.75 ± 0.24	1.79 ± 0.32
Vd (L/Kg)	0.28 ± 0.12	5.32 ± 0.98	9.52 ± 3.75
MRT (h)	1.72 ± 0.46	8.92 ± 1.35	4.18 ± 1.81
Absolute Bioavailability (%)	-	56.61 ± 7.21	55.93 ± 11.15

At 5mg/kg dose, S016-1348 shows significantly better in-vivo anti-tumor efficacy than LCL-161

Figure 9: S016-1348 - in-vivo Efficacy Dose – 2.5mg/kg/day
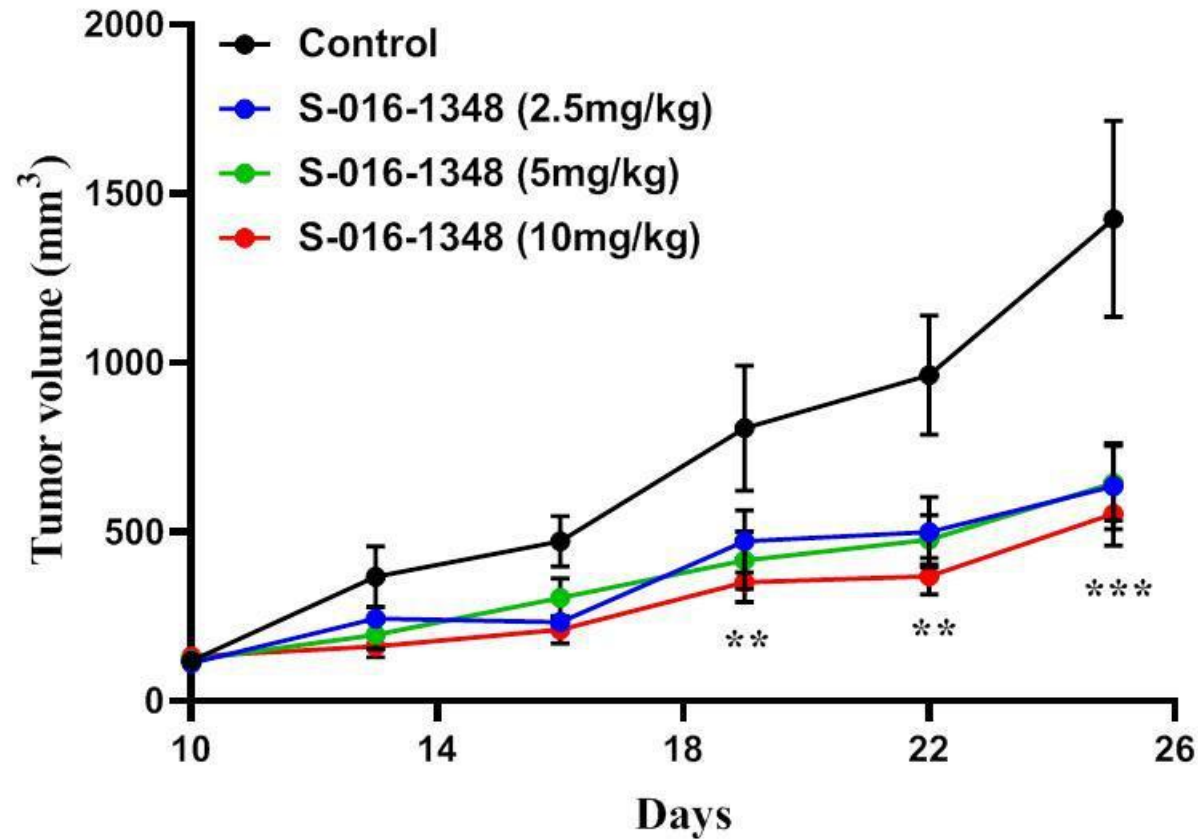
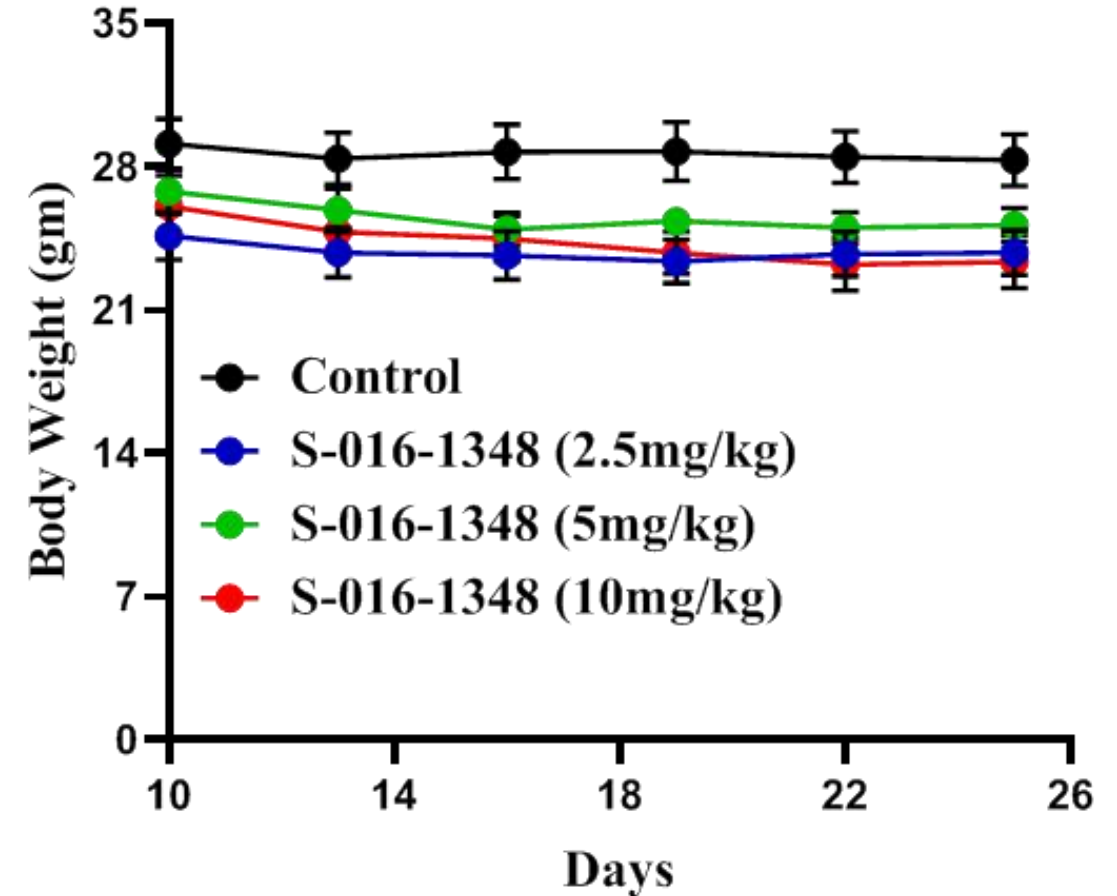**p<0.005, compared to Control

N=6

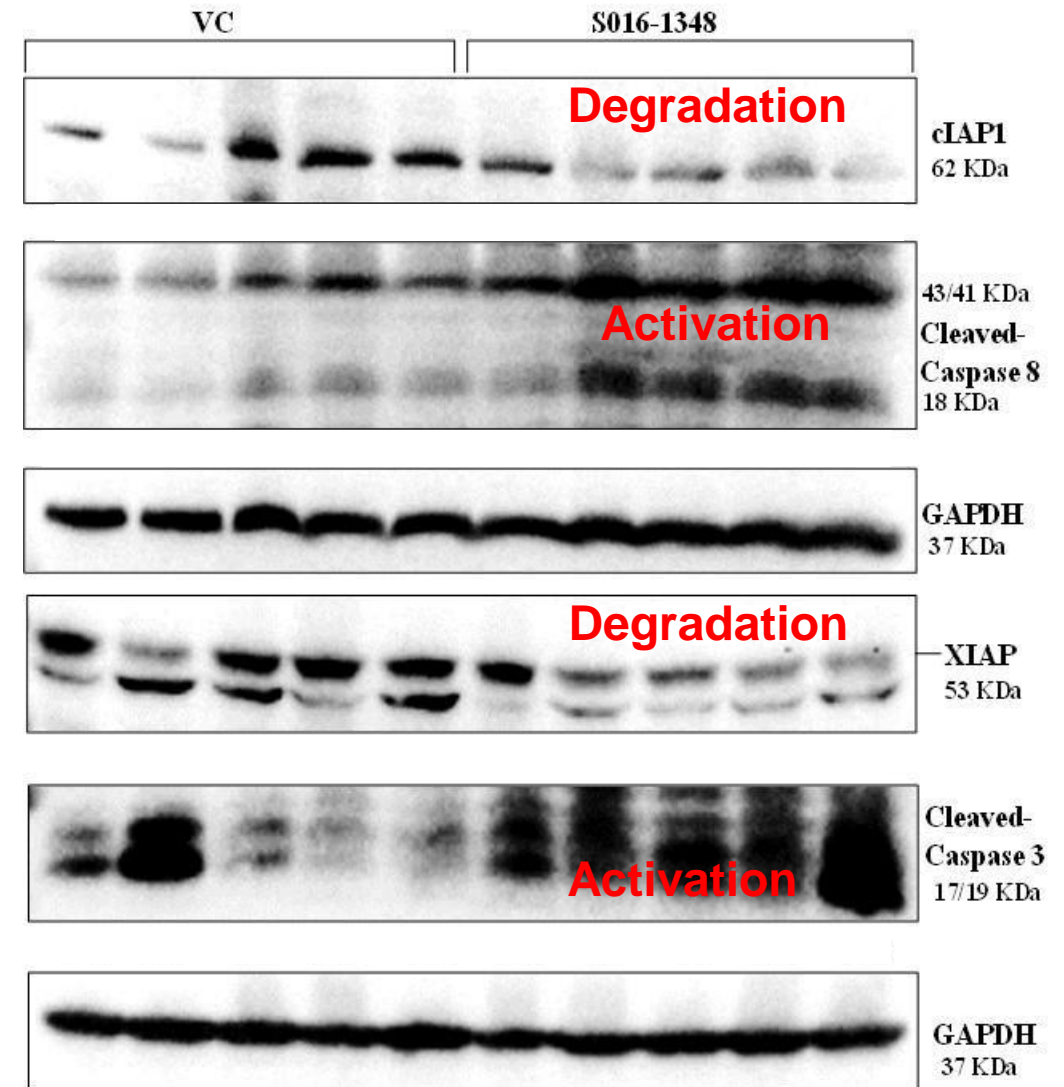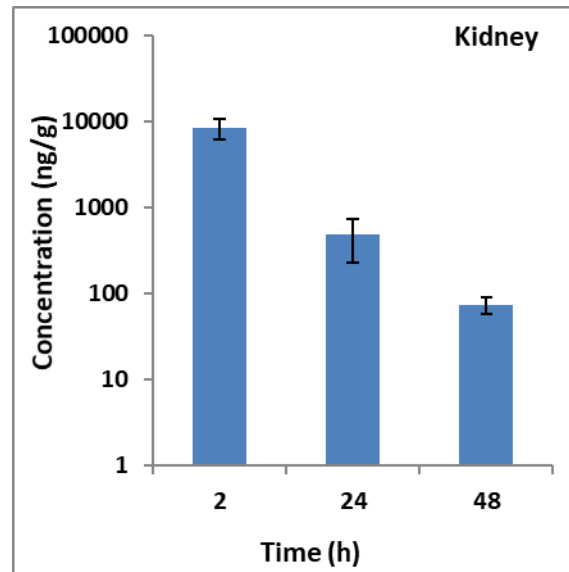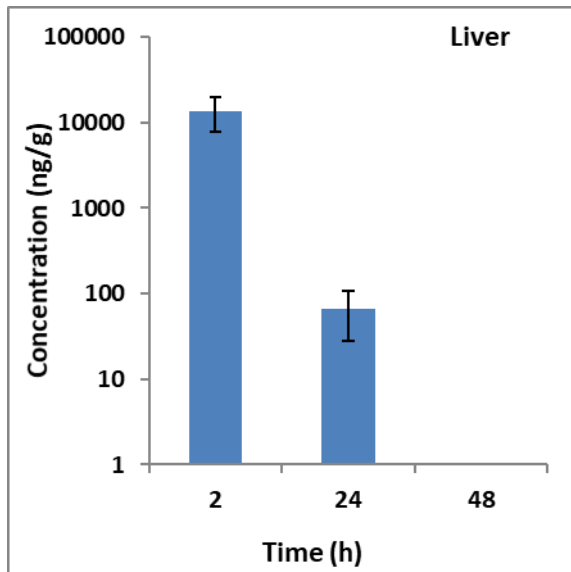***p<0.0005, compared to Control

Colon Cancer (HCT116) Xenograft Model
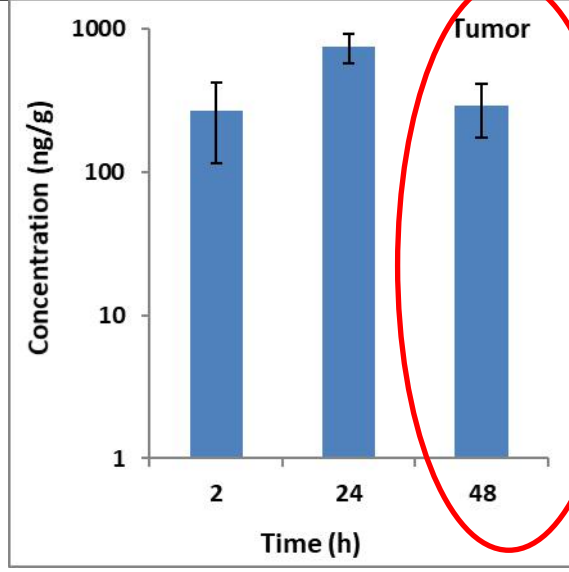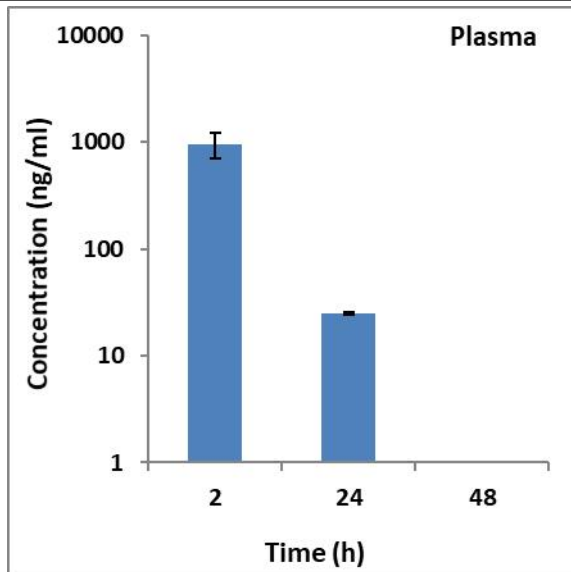
WB: Harvested Tumor Lysate
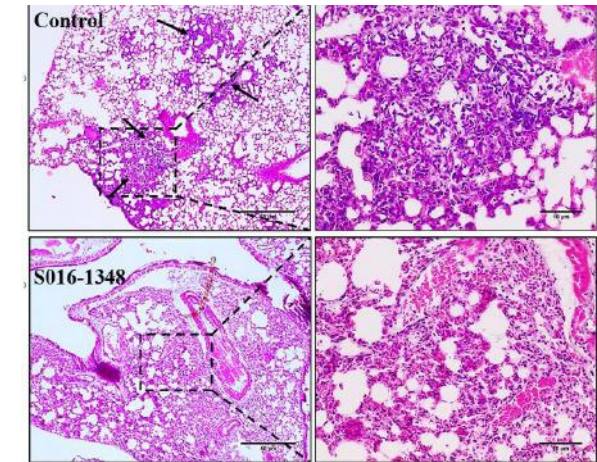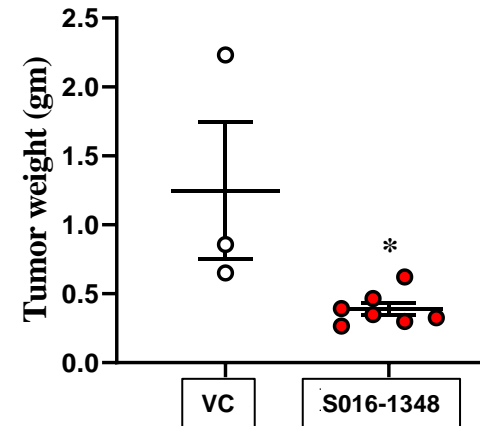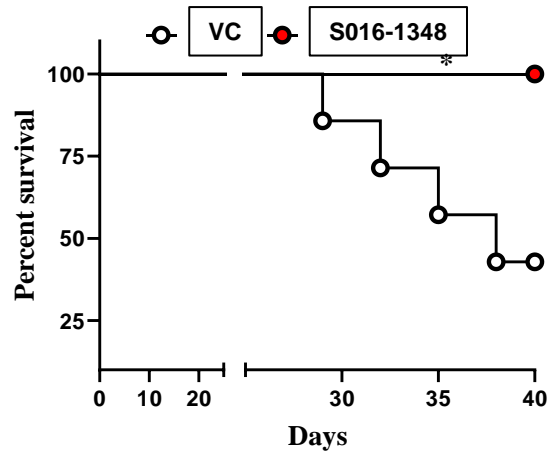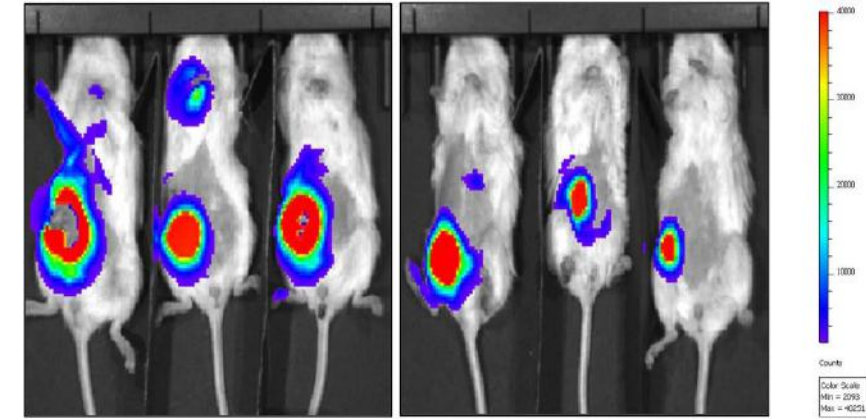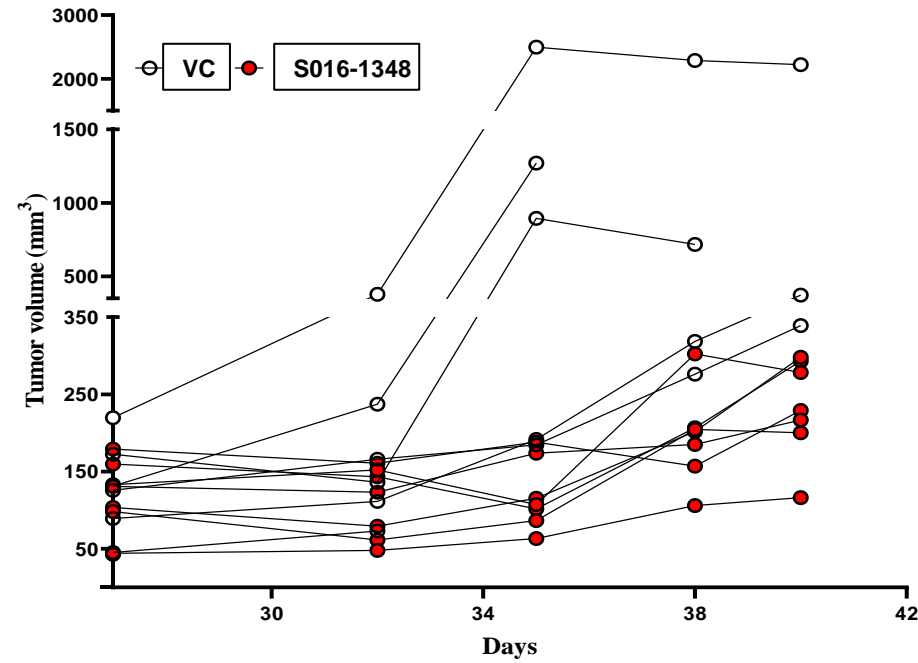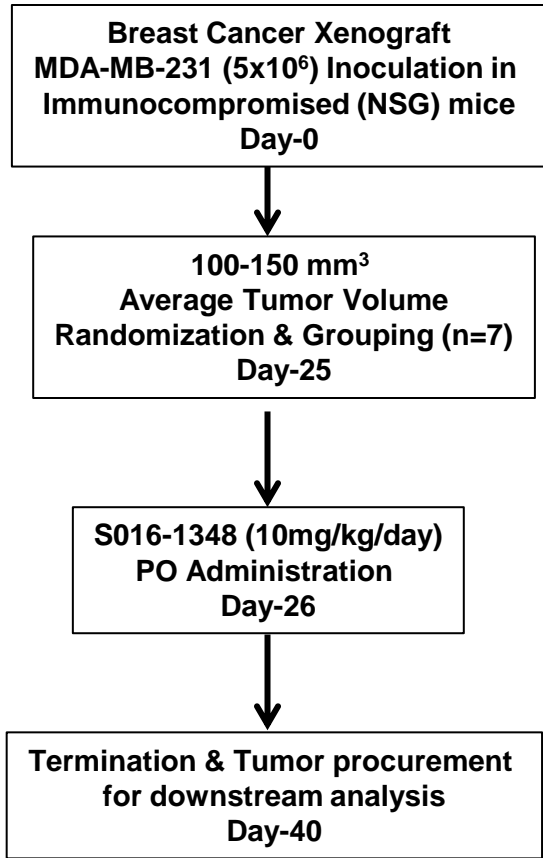
S-016-1348: Single Dose Toxicity Study in SD Rats by Oral Route – 14 Day Observation Period Body Weight (gm, Mean ±SD) of Animals of all Groups

Group No	Male (n=3)			Female (n=3)		
		Initial	Final		Initial	Final
Control	Mean	162.27	242.98	Mean	148.97	188.32
	±SD	5.13	10.66	±SD	11.42	19.90
50mg/kg	Mean	162.68	246.42	Mean	149.90	189.60
	±SD	6.13	16.03	±SD	8.39	14.49
150mg/kg	Mean	162.57	230.97	Mean	146.50	187.12
	±SD	7.65	26.26	±SD	4.84	11.21
500mg/kg	Mean	166.48	242.37	Mean	147.18	182.26
	±SD	7.13	14.39	±SD	3.42	5.37

No Mortality

No Loss of Body Weight

No Change in Water and Food intake

No Gross Pathological changes

No adverse effect at highest dose – 500mg/kg tested so far

Animals:
SD Rats

Doses:
50, 150 & 500 mg/kg body wt.

No. of animals:
3M + 3F per group

Vehicle:
0.5% Na-CMC

Route:
Oral

Duration:
7 Day Repeat Dose

7 Days — Quarantine

7 Days — Acclimatization

7 Days — Treatment / Observations

- Mortality
- General Behavior
- Body Weight
- Food & Water Intake

Daily

Initial & Final

Autopsy

- Gross Morphology
- Blood Biochemistry
- Hematology
- Organ weights
- Histopathology
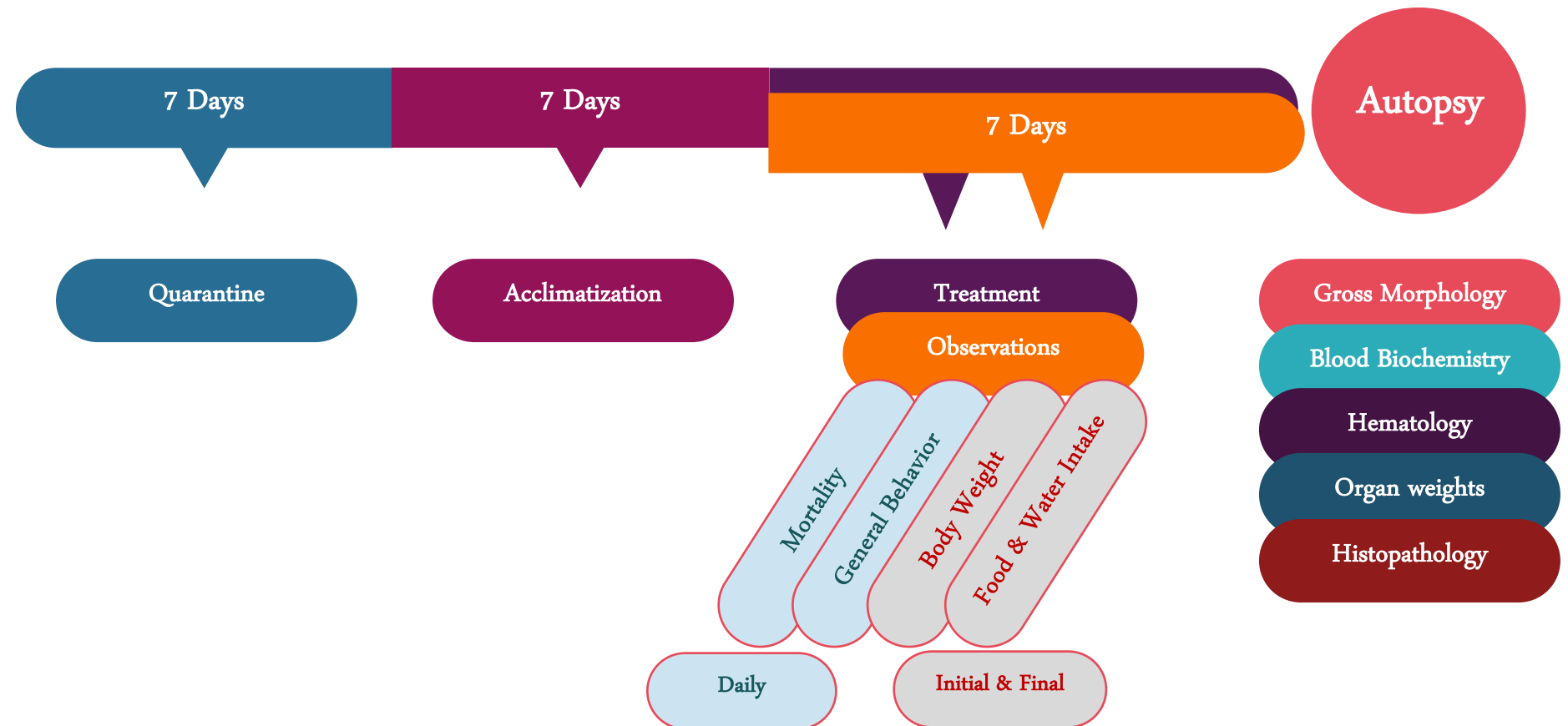
Figure 14
(S016-1348)

No Observed Adverse Effect Level (NOAEL)

Efficacy Dose in mice:
2.5-5mg/kg
Safety Index: 20-40 Fold

150
mg/kg body weight
in SD Rats

No Mortality, No gross abnormality of organs observed

Food and Water Intake comparable to control

Body weight gain comparable to control

Blood Biochemistry and Hematology parameters comparable to control

Unmet Medical Need: Lack of Small molecule Targeted Therapy

Standard of care: Chemotherapy (India), Chemotherapy+/-MAbs (Abroad)

Target: XIAP antagonism through Smac mimicking activity

Indication: Colon cancer, TNBC

Differentiation: Better efficacy than Phase-II Novartis Smac mimetic LCL161

In vitro studies:

- Cell free binding (XIAP-BIR2-Kd:330nM; XIAP-BIR3 Kd: 142nM)

- Cell based cytotoxicity: 500-1000nM based on cell lines in colony formation assay (CFA)

- 2-8 μM in Cisplatin resistant colon cancer cells by 48hr SRB assay (better than Novartis Smac mimetic LCL-161)

In vivo efficacy: (PO: Efficacy Dose) **2.5mg/kg/day Rat: 3.75mg/kg/day**

- Anti-tumor efficacy in Xenograft model: % tumor regression with respect to control (Oral Administration: head to head comparison)

  30 mg/kg every third day – S016-1348 vs LCL-161: **66% vs 50%**

  10 mg/kg/day – S016-1348 vs LCL-161: **55% vs 30%**

  05 mg/kg/day – S016-1348 vs LCL-161: **50% vs 20%**

Pharmacokinetics

In vitro:

SGF stability: 98%   SIF stability: 97%

Plasma (rat) stability: 78% ;   Metabolic stability (HLM): 75%

In vivo mice Pk at 30mg/kg:

- $T_{1/2}$ (h): 2.10 ± 0.15
- C_{max} (ng/mL): 5018.33 ± 853.66
- $AUC_{0-\infty}$ (h*ng/mL): 17439.13 ± 2220.28
- P. O. Bioavailability: 55%, Rat – 18 %

Safety and Toxicity

MTD (Acute tox): 500mg PO single dose: No mortality and morbidity (in Rat)

7-Day DRF (500, 150, 50mg/kg) – No Mortality, NOAEL: 150mg

CYP IC_{50}: 1A2, 2C9, 2D6, 2B6 > 20μM, 3A4 Midazolam <0.1μM

hERG IC_{50}: S016-1348, >5μM, LCL-161<3μM

Next steps
- IND Studies

Loss of PERK function promotes ferroptosis by downregulating SLC7A11 (System Xc⁻) in colorectal cancer

Krishan Kumar Saini[1,2], Priyank Chaturvedi[1], Abhipsa Sinha[1], Manish Pratap Singh[1], Muqtada Ali Khan[1], Ayushi Verma[1], Mushtaq Ahmad Nengroo[1], Saumya Ranjan Satrusal[1,2], Sanjeev Meena[1], Akhilesh Singh[1], Sameer Srivastava[3], Jayanta Sarkar[1,2], Dipak Datta[1,2,*]

Author's Affiliation:
[1]Division of Cancer Biology, CSIR-Central Drug Research Institute (CDRI), Lucknow 226031, India
[2]Academy of Scientific and Innovative Research, Ghaziabad, Uttar Pradesh, 201002, India.
[3]Department of Biotechnology, Motilal Nehru National Institute of Technology Allahabad, Prayagraj, 211004, India

Short Title: *PERK inactivation stimulates ferroptosis*

Key Words: ER stress, UPR, PERK, SLC7A11, Ferroptosis, Cancer

* Corresponding Author:
Dipak Datta, Division of Cancer Biology, CSIR-CDRI, B.S. 10/1, Sector 10, Jankipuram Extension, Sitapur Road, Lucknow-226031, India, Tel: 91-522-2772450 (Extn-4347/48), Fax: 91-522-2771941, E-mail: dipak.datta@cdri.res.in

Abstract
Ferroptosis, a genetically and biochemically distinct form of programmed cell death, is characterised by an iron-dependent accumulation of lipid peroxides. Therapy-resistant tumor cells display vulnerability toward ferroptosis. Endoplasmic Reticulum (ER) stress and Unfolded Protein Response (UPR) play a critical role in cancer cells to become therapy resistant. Tweaking the balance of UPR to make cancer cells susceptible to ferroptotic cell death could be an attractive therapeutic strategy. To decipher the emerging contribution of ER stress in the ferroptotic process, we observe that ferroptosis inducer RSL3 promotes UPR (PERK, ATF6, and IRE1α), along with overexpression of cystine-glutamate transporter SLC7A11 (System Xc⁻). Exploring the role of a particular UPR arm in modulating SLC7A11 expression and subsequent ferroptosis, we notice that PERK is selectively critical in inducing ferroptosis in colorectal carcinoma. PERK inhibition reduces ATF4 expression and recruitment to the promoter of *SLC7A11* and results in its downregulation. Loss of PERK function not only primes cancer cells for increased lipid peroxidation but also limits in vivo colorectal tumor growth, demonstrating active signs of ferroptotic cell death *in situ*. Further, by performing TCGA data mining and using colorectal cancer patient samples, we demonstrate that the expression of *PERK* and *SLC7A11* is positively correlated. Overall, our experimental data indicate that PERK is a negative regulator of ferroptosis and loss of PERK function sensitizes colorectal cancer cells to ferroptosis. Therefore, small molecule PERK inhibitors hold huge promise as novel therapeutics and their potential can be harnessed against the apoptosis-resistant condition.

Introduction

Cancer is a leading cause of death worldwide; in 2020, there were 19.3 million new cases of all types of cancer in which more than half of the patients died. Colorectal cancer is the third most commonly diagnosed cancer (10.0%) and the second leading cause of death (9.4%) worldwide in both males and females [1]. Therapy resistance is the key to tumor relapse and subsequent tumor-associated mortality. Evasion of apoptosis is one of the important hallmarks of cancer cells and mechanisms behind the same have enormous therapeutic potential in the context of current cancer research [2]. Recently, we have shown how intracellular CXCR4 protein and epigenetic modulator EZH2 promote therapy resistance, CSC properties and metastasis in colorectal and breast cancer [3–5]. Recent reports also suggest that these resistant cancer cells are vulnerable to iron-mediated cell death or 'Ferroptosis' [6,7].

As originally discovered by the Stockwell group, ferroptosis is morphologically, biochemically and genetically distinct from apoptosis, necroptosis, and autophagy and depends on intracellular iron [8,9]. Selenoprotein Glutathione peroxidase 4 (GPx4), cystine/glutamate antiporter (System Xc⁻) and enzyme Acyl-CoA synthetase long-chain family member 4 (ACSL4) are known to be the key modulators of ferroptotic process [10–12]. GPx4 is the critical enzyme that can reduce lipid hydroperoxides within biological membranes; hence ferroptosis can be induced by the treatment of small molecule GPx4 inhibitor RSL3 (Ras Selective Lethal) treatment [13,14]. SLC7A11 or System Xc⁻ is a multi-pass transmembrane protein that facilitates the export of intracellular glutamate and import of extracellular cystine in a 1:1 ratio [15]. Following cellular absorption, cystine (dimer) is reduced to form cysteine (monomer), which serves as the rate-limiting precursor for glutathione (GSH) synthesis [16]. GPx4 mediates the conversion of toxic lipid peroxides to nontoxic lipid alcohols in the presence of GSH[17]. Inhibition of SLC7A11 results in GSH depletion, which in turn promotes GPx4 downregulation, leading to the damage of cellular/subcellular membranes caused by the accumulation of iron-dependent lipid peroxides or ferroptosis [18]. On the other hand, ACSL4 modulates ferroptosis sensitivity by shaping the cellular lipid composition of the cell [20].

Though therapy-resistant cells have vulnerability to ferroptotic cell death, these cells are proficient in handling therapeutic insults by adapting to cellular stress caused by Unfolded Protein Response (UPR)[21]. UPR is initiated by three transmembrane proteins PERK (Protein kinase RNA-like endoplasmic reticulum kinase), ATF6 (activating transcription factor 6), IRE1α (inositol-requiring enzyme 1α), which are commonly known as three arms of UPR [22,23]. These three proteins are responsible for maintaining cell survival and homeostasis by regulating protein folding in response to UPR [24]. These proteins have an ER-luminal domain believed to sense the protein misfolding; alteration in this domain in response to stress also changes the oligomerization state of these UPR proteins. PERK and IRE1α only need the oligomerization of the luminal domain to be activated; an ER chaperone Bip/GRP78 binding keeps these two proteins inactive by maintaining these proteins in ER membrane in unstressed cell conditions [25,26]. PERK has a single kinase domain that limits eIF2α activity by phosphorylating it, resulting in global translation attenuation, whereas ATF4 translation is selectively upregulated when active eIF2α is limiting [27]. IRE1α possesses kinase and RNase activity; when activated, IRE1α cleaves *XBP1*, and *XBP1* then activates transcription of many ER-related genes that regulate protein folding in the ER [28,29]. ATF6 is translocated to the Golgi lumen and cleaved by site-1 protease (S1P) and Site-2 protease (S2P) to produce ATF6 (N). ATF6 (N) and XBP1 promote protein transcription, which increases ER size and protein folding capacity [30,31]. These transcriptional processes work in concert as homeostatic feedback loops to reduce ER stress. If the amount of misfolded protein is declined, UPR signaling is decreased and the cell survives.

The influence of UPR in regulating tumor cell apoptosis and autophagic cell death is vastly studied in the literature [32,33]. Ferroptosis-induced ER stress has been documented previously [34], however, very little is known regarding the role of UPR in modulating ferroptosis. Here, we reveal that ferroptosis inducer RSL3 promotes an enormous amount of ER stress in colorectal cancer cells. In the course of dissecting the impact of three independent UPR arms in modulating RSL3 induced ferroptosis, we observe that among all three arms of UPR, PERK selectively prevents ferroptotic tumor cell death. Further analysis suggests that PERK activation and downstream signaling protects tumor cells from ferroptosis through SLC7A11 upregulation. Similarly, loss of PERK function results in reduced colorectal tumor growth in vivo with increased ferroptosis. Finally, TCGA data mining and expression analysis of colorectal cancer patient-derived tumors with their matched normal counterpart display a positive correlation between *PERK* and *SLC7A11* expression signifying the clinical relevance of our finding.

Results

PERK arm of UPR positively regulates SLC7A11 (System Xc⁻) expression in colorectal cancer cells

The relationship between apoptosis/autophagic cell death and UPR or ER stress is well established. However, the contribution of UPR in modulating ferroptotic cell death in colorectal cancer remains elusive. To investigate the above relationship, first, we tested the impact of ferroptosis inducer (RSL3) on three different arms of UPR (PERK, ATF6 and IRE1α) in different colorectal cancer cells HT29, SW620, DLD1, and HCT116. As shown in Figures 1A-D, classical ferroptosis inducer RSL3 promotes the expression of three arms of UPR in all four colorectal cancer cells. In all the cases, RSL3 not only increases PERK protein expression but also promotes PERK phosphorylation as indicated by the upward shift of the PERK band as PERK has multiple phosphorylation sites. As expected, we also find similar upregulation of downstream effector proteins of UPR, such as ATF4 and Bip/GRP78 following RSL3 treatment (Supplementary Figure 1) in CRC cells. Further, we evaluated its effect on the expression of ferroptosis signature genes, such as *GPx4, ACSL4*, and *SLC7A11*.

Figure 2

As observed in Figure 1E, being a GPx4 inhibitor, RSL3 treatment inhibits GPx4 expression as expected, whereas the expression of SLC7A11 is markedly upregulated in HT29 cells, having no impact on ACSL4 expression. Similar results are obtained in other CRC cells (Supplementary Figure 2). Further, we sought to determine the role of three different UPR arms in the expression of ferroptosis signature genes *GPx4, ACSL4*, and *SLC7A11* in HT29 colorectal cancer cells. In Figure 1F-H, we observe individual knockdowns of each UPR arm like PERK, ATF6 and IRE1α in HT29 cells, resulting in non-noticeable changes in protein expression of ferroptotic genes except PERK knockdown markedly reduces the expression of SLC7A11 protein as compared to control. Since
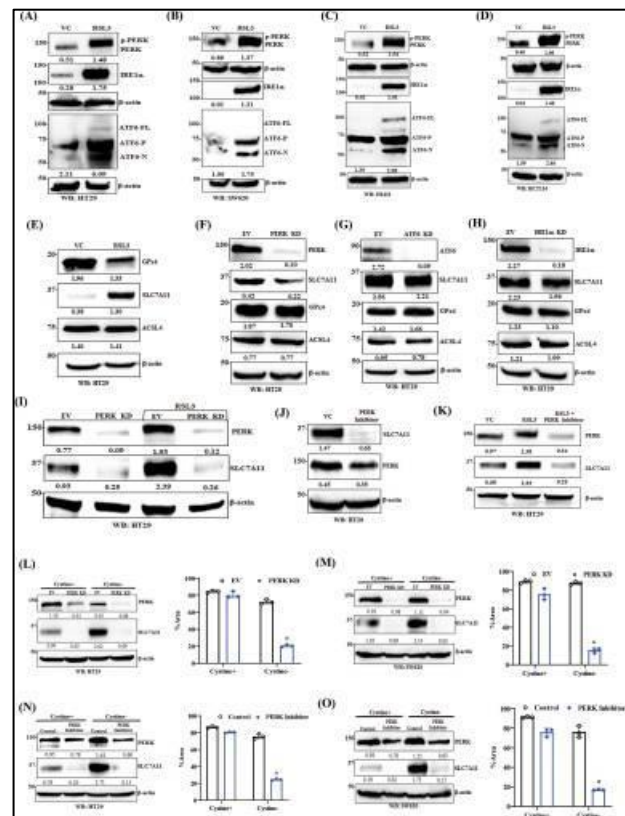
RSL3 was shown to upregulate SLC7A11 expression at basal conditions, we evaluated the effect of RSL3 on PERK genetic and pharmacological silencing in CRC cells. PERK knockdown prevented RSL3 induced SLC7A11 overexpression in both HT29 (Figure 1I) and SW620 (Supplementary Figure 3) cells as compared to their respective controls. Similarly, loss of PERK function (kinase activity inhibition) by PERK inhibitor (GSK2656157) treatment results in dramatic reduction of SLC7A11 expression in HT29 (Figure 1J) and other CRC cells (Supplementary Figure 4). We further treated HT29 cells either with RSL3 alone or in combination with PERK kinase inhibitor GSK2656157 and found that PERK inhibitor also mitigates RSL3 induced SLC7A11 expression (Figure 1K). Therefore, either the loss of PERK protein or functional loss of PERK kinase activity through PERK inhibitor dampens SLC7A11 expression at the basal conditions and abrogates RSL3-mediated SLC7A11 induction. Additionally, we cultured EV and PERK knockdown HT29 and SW620 cells for 72 hours in cystine$^+$ and cystine$^-$ conditions and observed that SLC7A11 expression is upregulated in cystine$^-$ conditions as compared to cystine$^+$ control. The above phenomenon is significantly abolished in PERK knockdown in HT29 and SW620 cells (Figure 1L-M, left panel), suggesting that PERK is indispensable for SLC7A11 upregulation in cystine-starved conditions. Further, the pictorial representation (Supplementary Figure 5, upper panel) and densitometric quantification (Figure 1L-M right panel), show a significant reduction in cell number (area covered) in PERK knockdown condition compared to the respective control when cells are cultured without cystine. As shown in Figure 1N-O and Supplementary Figure 5, bottom panel, we also cultured PERK inhibitor-treated HT29 and SW620 cells in cystine$^+$ and cystine$^-$ conditions for 72 hours and observed that PERK functional inhibition reduces SLC7A11 expression in both the culture conditions and inhibits cell viability in cystine$^-$ condition. Above findings suggest that either the genetic loss of PERK protein or functional loss of PERK kinase activity through PERK inhibitor treatment reduces cell viability in cystine$^-$ conditions and dampens SLC7A11 expression not only at basal condition but also abrogates RSL3 mediated SLC7A11 induction.

PERK loss of function sensitizes colorectal cancer cells to ferroptosis

SLC7A11 (System Xc$^-$) is a vital membrane transporter that imports cystine into the cytosol in exchange for glutamate, while glutathione synthetase and γ-glutamylcysteine synthetase synthesize the antioxidant and GPx4 substrate glutathione. Our prior findings show that loss of PERK reduces System Xc$^-$ expression, implying that this down-regulation might play a role in ferroptosis regulation. So, we treated different UPR arm knockdown HT29 cells with RSL3 and observed that PERK knockdown cells are more selectively sensitive to RSL3 mediated cell death than vehicle control, ATF6 KD, or IRE1α KD cells (Figure 2A and Supplementary Figure 6, top panel). PERK knockdown in SW620 cells produces similar results (Figure 2B and Supplementary Figure 6, bottom panel). We treated HT29 cells with erastin, another potent ferroptosis inducer, and observed sensitization in PERK knockdown cells compared to the control (Supplementary Figure 7). To further confirm the above observations, we seeded equal
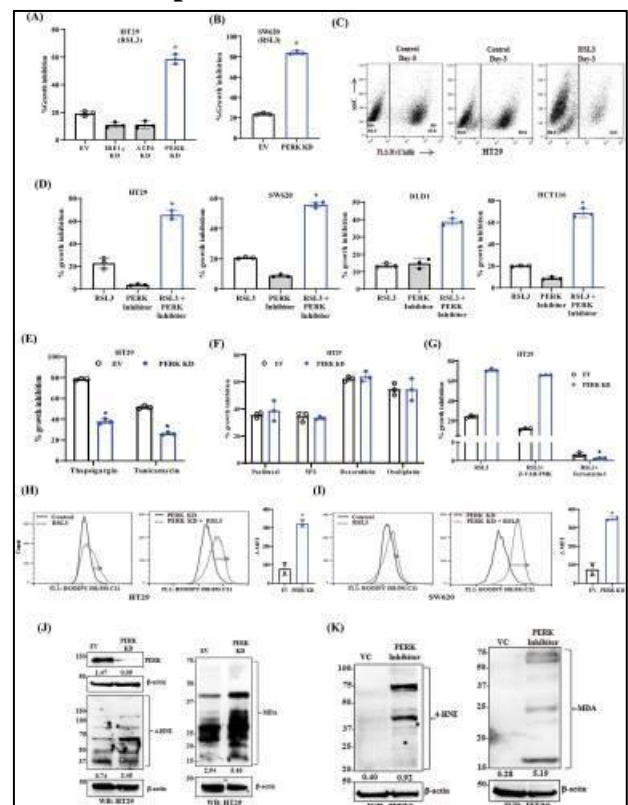

Figure 1

numbers of untagged HT29 EV (white) and chilli-luc tagged PERK (red) knockdown cells and cultured in the absence and presence of RSL3 for 3 days. FACS analysis of Day 0 and Day 3 cells shows a marked reduction of chilli luc tagged PERK (red) knockdown cells compared to untagged white control cells, again suggesting that loss of PERK sensitizes HT29 cells to cytotoxic function of RSL3 (Figure 2C). Similar with the above findings, PERK inhibitor treatment markedly sensitizes RSL3 induced colon cancer cell (HT29, SW620, DLD1 and HCT116) death (Figure 2D and Supplementary Figure 8). To understand the selectivity of PERK function in sensitizing the actions of other ER stress inducers, control and PERK knockdown cells were treated with Thapsigargin and Tunicamycin and observe that both the ER stress inducers failed to deliver their cytotoxic effect in absence of PERK, instead of its sensitization impact that was seen earlier in case of RSL3 (Figure 2E). Next to understand the clinical significance of this sensitization, we treated control and PERK knockdown HT29 and SW620 cells with classical chemotherapeutic drugs like paclitaxel, 5-fluorouracil and oxaliplatin and assessed their combined cytotoxic potential. Unfortunately, again we did not observe any synergistic cytotoxic effect on any of the chemotherapeutic drugs in combinations with PERK loss of function (Figure 2F, Supplementary Figure 9, 10). The above findings suggest that sensitization observed by PERK knockdown is specific to RSL3. Next, we sought to determine whether RSL3-mediated sensitization of cell death in the loss of PERK function is due to the induction of apoptosis or ferroptosis. To find out the same, we treated PERK knockdown cells with RSL3 in the presence or absence of either apoptosis inhibitor (pan-caspase inhibitor Z-VAD-FMK) or ferroptosis inhibitor (ferrostatin-1) and observed that only ferroptosis inhibitor (ferrostatin-1) significantly rescues cytotoxic impact of RSL3 (Figure 2G). The above findings demonstrate the role of ferroptosis in PERK knockdown-mediated sensitization of cell death. Additionally, there was no significant difference in cell growth inhibition with RSL3 along with pan-caspase inhibitor, so classical apoptotic cell death has a minimal role associated with RSL3-induced cell death. Ferroptosis is distinct from other types of programmed cell death and is characterised by the accumulation of lipid peroxides that can be detected by BODIPY-C11 staining of cells [35] To check the level of lipid peroxidation after RSL3 treatment, we treated HT29 (Figure 2H, left and right panel) and SW620 (Figure 2I, left and right panel) EV and PERK knockdown cells with RSL3 for 24 hours and subjected them to BODIPY-C11 staining (details described in materials and methods), we observe a marked increase in excitation shift of BODIPY-C11 staining in PERK knockdown cells as compared to control, suggesting that loss of PERK promotes lipid peroxidation and ferroptosis in colorectal cancer cells. 4-HNE and MDA are known lethal by-products of lipid peroxidation or ferroptosis, formed during the enzymatic and non-enzymatic breakdown of AA (arachidonic acid) and other PUFAs (polyunsaturated fatty acids) [36,37]. Here, we assessed the expression of 4-HNE and MDA in HT29 control, PERK KD and PERK inhibitor-treated cells and found their robust upregulation in both PERK KD (Figure 2J) and PERK inhibitor (Figure 2K) treated cells as compared to respective controls. PERK kinase activity inhibition in other CRC cell lines (SW620, DLD1 and HCT116) showed similar upregulation of these ferroptosis biochemical markers as compared to their respective controls (Supplementary Figure 11). The above observations highlight the importance of PERK as a negative ferroptosis regulator in colorectal cancer and suggest that apoptotic cell death has a minimum role in PERK mediated ferroptosis modulation. The above experimental evidence suggested us to dig deeper into the mechanistic aspects of PERK-mediated SLC7A11 regulation and ferroptosis induction.

**PERK regulates the expression and recruitment of transcription factor ATF4 to the promoter of SLC7A11 in the course of ferroptosis modulation**

RSL3-mediated upregulation of UPR-responsive proteins and further PERK mediated robust upregulation of SLC7A11 protein expression in RSL3 treatment prompted us to evaluate the impact of RSL3-mediated gene regulation at transcriptional level. We evaluated mRNA expression of UPR

marker genes i.e., *PERK, ATF6* and *IRE1a* and *SLC7A11* in HT29 cells (vehicle control and RSL3 treatment) and observed that all three UPR marker genes (Figure 3A) and SLC7A11 (Figure 3B) were found to be highly upregulated in RSL3 treated cells as compared to control. RSL3 mediated robust induction of PERK mRNA expression justifies its protein overexpression following RSL3 treatment. Next, we wanted to determine RSL3 mediated PERK activation is a direct RSL3 effect or indirect via the RSL3 mediated induction of ferroptosis. To investigate such possibilities, we treated cells with RSL3 alone and in combination with ferroptosis inhibitor Ferrostatin-1 (FER-1) and assessed the activation status of PERK and its downstream proteins. As shown in Figure 3C, RSL3 treatment promotes robust PERK activation or phosphorylation (as determined by upper shift of PERK band) along with overexpression of GRP78 and ATF4. However, the whole RSL3 mediated PERK and downstream activation was found to be completely abrogated when the cells are pre-treated with FER-1. Therefore, RSL3-mediated ferroptosis induction or lipid peroxidation promotes PERK phosphorylation and its downstream signals. To further confirm the positive regulatory loop between PERK and SLC7A11, we utilized Thapsigargin to activate the whole pathway and then assessed the impact of PERK inhibitor on SLC7A11 modulation. As shown in Figure 3D, PERK inhibitor treatment completely mitigated Thapsigargin induced PERK activation, SLC7A11, and ATF4 induction. As ATF4 is a critical downstream transcription factor of *PERK*, we further determined the level of ATF4 protein in control and PERK knockdown cells
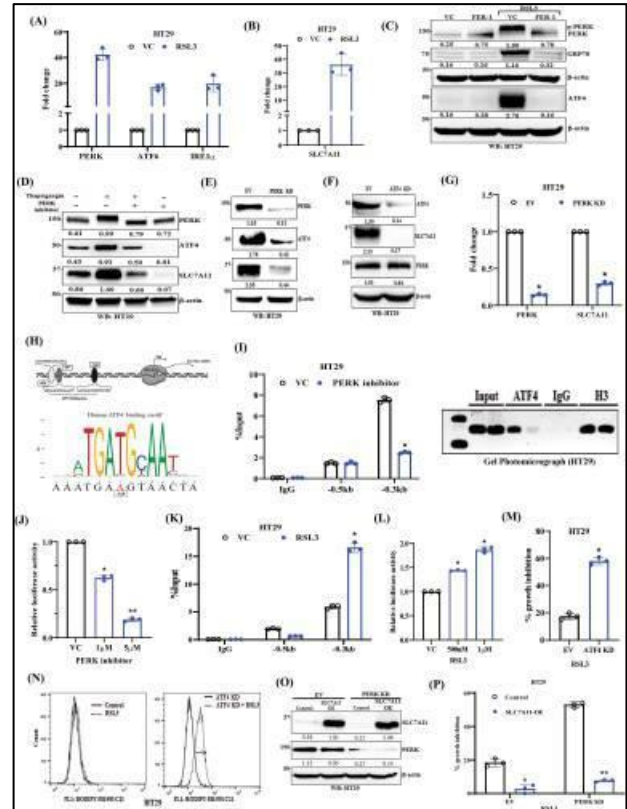
Figure 3

level of ATF4, as well as

 SLC7A11, are markedly downregulated in PERK knockdown cells as compared to control (Figure 3E). Moreover, to understand the direct regulation of ATF4 on SLC7A11 expression, we made stable knockdown of ATF4 in HT29 cells and observed that SLC7A11 protein expression is robustly downregulated in ATF4 knockdown cells as compared to control (Figure 3F). Because *ATF4*, a major PERK downstream transcription factor, is downregulated in PERK KD conditions, we decided to investigate the role of PERK in *SLC7A11* transcriptional regulation. First, we observed that PERK knockdown severely reduces mRNA expression of *SLC7A11* in HT29 colorectal cancer cells, as observed in Figure 3G. Further, we wanted to evaluate the contribution of ATF4 recruitment in PERK mediated downregulation of SLC7A11 expression. As shown in Figure 3H, the *SLC7A11* promoter has three putative ATF4 binding sites predicted by the publicly available software Eukaryotic Promoter Database (https://epd.epfl.ch/). In our ChIP assay (Figure 3I), we observed marked selective enrichment of ATF4 at the -0.3kb site upstream of the *SLC7A11* promoter in control cells, which was found to be significantly reduced following PERK inhibitor treatment. Loss of ATF4 recruitment at the *SLC7A11* promoter following PERK inhibition prompted us to check its role in modulating *SLC7A11* transcription. In our dual luciferase assay, we transfected the SLC7A11 promoter luciferase construct in HT29 cells (-0.6 kb from the TSS, cloned in the luciferase assay reporter vector pGL4.12), and found that PERK inhibitor reduces SLC7A11 transcription (relative

luciferase activity) in a dose-dependent manner (Figure 3J). The above data suggest that ATF4 functions as a transcription factor in PERK mediated regulation of *SLC7A11* expression. To further confirm the above hypothesis, we performed ChIP assay in HT29 cells and found that RSL3 treatment increased the enrichment of ATF4 on the predicted binding site at the SLC7A11 promoter (Figure 3K). Further, as observed in dual luciferase assay, RSL3 treatment induces SLC7A11 transcriptional activity in a dose-dependent manner in HT29 cells (Figure 3L). To assess the phenotypic impact of the PERK-ATF4-SLC7A11 axis, we treated control and ATF4 KD cells with RSL3 and performed cell viability assay and BODIPY C11 staining. As observed in Figure 3M, ATF4 loss not only makes cells prone to death in response to RSL3 but also promotes increased ferroptosis compared to control (Figure 3N). Altogether, our experimental results clearly indicate that PERK regulates ferroptosis through *SLC7A11* expression by modulating the recruitment of ATF4 to its promoter. To further evaluate the phenotypic role of System Xc⁻ in the hypersensitivity of PERK loss of function toward RSL3 in CRC cells, we ectopically overexpressed SLC7A11 in HT29 EV and PERK KD cells (Figure 3O) and determined cytotoxic response of RSL3 in those conditions. As shown in Figure 3P, both EV and PERK KD HT29 cells become significantly resistant to RSL3 mediated ferroptotic cell death following ectopic overexpression of SLC7A11. The above observation suggests that SLC7A11 or System Xc⁻ is a major player in PERK driven ferroptotic process.

Loss of PERK inhibits tumor growth and demonstrates active signs of ferroptotic tumor cell death in vivo

Considering the above-mentioned findings, we sought to look into the influence of PERK knockdown on tumor progression in vivo. We inoculated EV (control) and PERK KD HT29 cells (2×10^6 respectively) subcutaneously in nude mice and monitored the tumor progression twice a week for up to 6 weeks. As observed in Figure 4A-4C, compared to the control, PERK KD resulted in a marked reduction of tumor volume (Figure 4A, 4B) and weight (Figure 4C). Further, we performed western blot analysis of the harvested tumors to investigate the effect of PERK loss of function on the expression of SLC7A11 and ATF4 as well as hallmark ferroptotic markers such as 4-HNE and MDA in vivo. As observed in Figure 4D, PERK knockdown is maintained in vivo tumors and loss of PERK strongly reduces SLC7A11 expression along with ATF4 but promotes marked expression of both ferroptotic markers such as 4-HNE and MDA. We performed immunohistochemistry (IHC) staining using MDA and 4-HNE antibodies in control and PERK knockdown tumors to further validate the above finding. We observed that compared to the control, PERK KD tumors
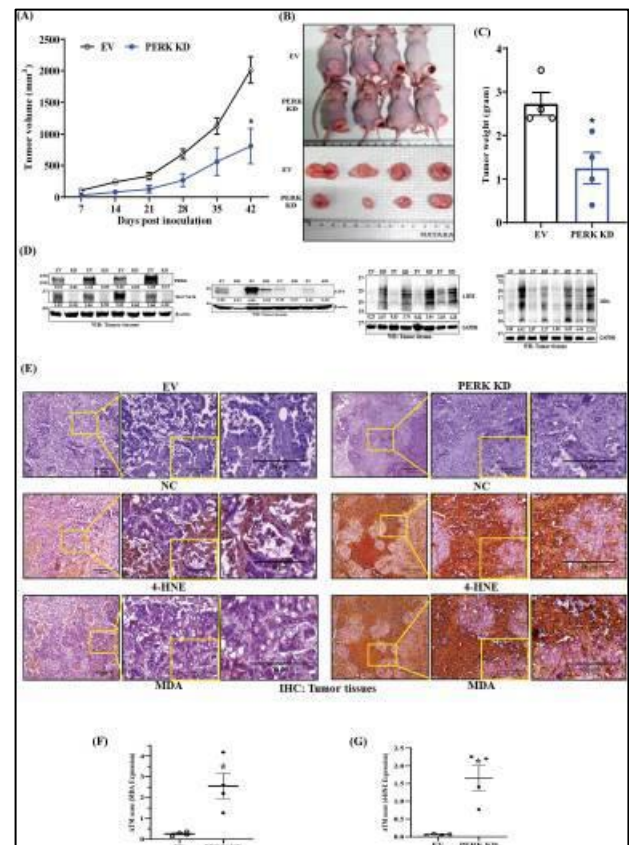
Figure 4

display robust overexpression of 4-HNE and MDA (Figure 4E). Further, we have calculated the IHC ATM (Averaged Threshold Measure) score by measuring the DAB intensity in respective IHC images, as represented in Figure 4F-G, where we find that PERK KD tumors have robustly high

ATM scores for both 4-HNE and MDA staining as compared to the control tumor. Together, our data indicate that PERK has an immense impact on tumor growth and genetic inhibition of PERK results in significant loss of tumor growth, along with the elevated levels of 4-HNE and MDA proteins. This suggests active ferroptotic tumor cell death in the course of PERK mediated tumor growth reduction.

Expression of *PERK* and *SLC7A11* is positively correlated in human colorectal cancer

To draw a clinical correlation between *PERK* and *SLC7A11* expression, we performed TCGA data mining using the UCSC Xena browser (https://xenabrowser.net/). We accessed mRNA expression data of 471 patients in the GDC TCGA COAD cohort of the database and drew a correlation plot between *PERK* and *SLC7A11* expression, and calculated Pearson's correlation (R), where we found a positive correlation between *PERK* and *SLC7A11* expression (Figure 5A). Further, we confirmed a positive correlation between *PERK* and *SLC7A11* expression in 15 human colorectal cancer patients by performing Real-Time-PCR analysis of CRC tumors and their respective matched normal counterparts (Figure 5B). As shown in Figure 5C-5D, we find that both PERK and SLC7A11 are overexpressed in human CRCs compared to normal counterparts.

The graphical abstract (Figure 5E) summarises how selectively the PERK arm of ER stress/UPR protects cancer cells from ferroptosis. PERK mediated ATF4 upregulation and ATF4 binding to the promoter of *SLC7A11* results in upregulation of System Xc⁻ that stimulates cystine import into the cytosol and inhibits lipid peroxidation and ferroptosis.

Figure 5

Discussion

Cancer cells make themselves resistant to therapeutic insults by effectively managing UPR and ER stress responses. It has been well established in the literature how an apoptotic stimulus induces ER stress in cancer cells leading to the activation of UPR and determination of the final cell fate decisions [38–40]. Recent reports also indicated the close connectivity between ferroptosis induced ER stress and crosstalk among ferroptosis and apoptosis [34,41]. Here, our study highlights that ferroptosis inducers can cause UPR and ER stress in colorectal cancer cells, where PERK arm of UPR selectively plays a decisive role in modulating ferroptotic response [42]. In corollary with our findings, ferroptosis inducers like Sorafenib, Dihydroartemisinin (DHA), Erastin, and 4-HNE (a by-product of lipid peroxides) have also shown to induce ER stress and UPR downstream signaling modulators. These modulators like ATF4, NRF2 GRP78 have been shown to prevent ferroptosis in different settings including cancer [11, 43–49]. Besides multiple reports demonstrating the involvement of the PERK arm of UPR in modulating apoptosis and autophagy, recent findings by Zheng et al. showed that PERK mediated sensitization of hepatocellular carcinoma in response to irradiation is due to enhanced apoptosis or ferroptosis [50]. In prostate cancer, it has been shown that loss of ATF6α promotes ferroptotic cell death, though the contribution of the other two arms (PERK and IRE1α) was not explored in this process [51]. In the current study, we observe the selective
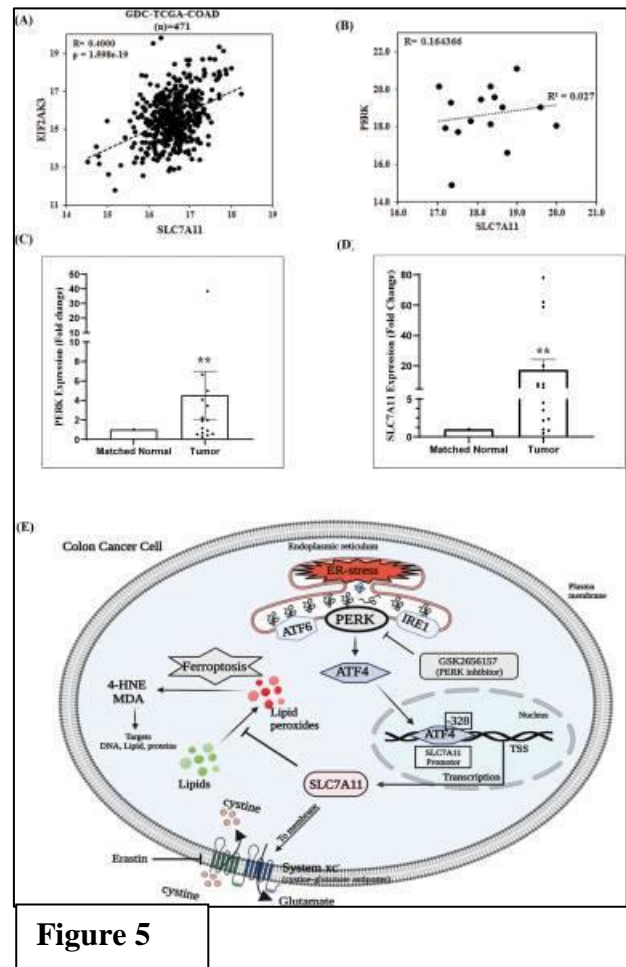
participation of PERK, over the other two UPR arms, in modulating ferroptosis. An elegant study by Chen et.al, earlier demonstrated that inhibition of the PERK-ATF4-HSPA5-GPX4 pathway increased DHA sensitivity of glioma cells by increasing ferroptosis, where they did not observe significant change in SLC7A11 level [46]. We observe similar upstream changes in response to RSL3 or loss of PERK function, but alterations in SLC7A11 level turn out to be the key factor for modulating ferroptotic phenotype in colon cancer. Our differential observations hint towards a possible contribution of context dependency and cancer specificity. Another unique aspect of our finding is that we observe exclusive ferroptotic cell death induction in the absence of PERK, which could only be rescued by ferroptosis inhibitor ferrostatin-1, and not by any other inhibitors of apoptosis and autophagy. This essentially advocates that the possibility of cross-talk between PERK mediated ferroptosis versus autophagy and apoptosis is minimal when the upstream signals come from lipid peroxidation. In fact, any of the chemotherapeutics tested in our study failed to sensitize colorectal cancer to either apoptosis or ferroptosis in the absence of PERK. This further supports the exclusivity of PERK in modulating the ferroptotic process. In addition to this, PERK has been shown to be selectively activated during Epithelial-to-Mesenchymal Transition (EMT) process, making cancer cells vulnerable to ER stress [52].

GPX4, SLC7A11 and ACSL4 are major downstream effectors of any ferroptotic process and the intricate balance between these play a critical role in executing full-blown ferroptosis [7,53,54]. For example, the presence of PERK in the cancer cells prevents the ferroptotic impact of GPX4 inhibitor RSL3 by positively regulating the expression of SLC7A11. Though the ferroptosis perspective was not studied, following exposure to paclitaxel, cancer cells have been shown to activate the PERK-ATF4 axis and maintain redox homeostasis by inducing the expression of the major antioxidant enzymes, including SLC7A11[55]. Several studies have indicated the regulation of *SLC7A11* by ATF4, but our study, for the first time, provided direct evidence for the transcriptional regulation of *SLC7A11* via ATF4 binding to its promoter [56,57]. In support of our observations, ATF4 has been shown to drive resistance to Sorafenib in hepatocellular carcinoma by preventing ferroptosis [58].

It is noteworthy to mention that in in vitro condition, functional loss of PERK either through PERK knockdown or by the treatment of PERK inhibitor alone does not result in ferroptotic cell death but loss of PERK function primes colorectal cancer cells towards ferroptosis which is evident by increased expression of 4-HNE and MDA in PERK knockdown state. However, in in vivo condition, we observe that PERK knockdown in colorectal cancer cells alone is able to reduce tumor growth significantly and harvested tumors show robust positivity for ferroptosis markers like 4-HNE and MDA. The above results advocate that in in vivo condition under the influence of tumor microenvironment, PERK loss of function alone is sufficient to deliver its anti-tumor impact. Therefore, PERK inhibitors may have huge therapeutic potential in the clinics especially where tumors are non-responsive to chemotherapy that usually promotes apoptotic cell death.

Altogether, our study reveals a new role of the PERK-ATF4-SLC7A11 axis in modulating ferroptotic cell death in colorectal cancer in vitro and in vivo and posits therapeutic rationale for the development of small molecule PERK inhibitors against colorectal cancers that are commonly resistant to apoptosis but vulnerable to ferroptosis.

Materials and Methods

Reagents and antibodies

Dimethyl Sulfoxide (DMSO), ferrostatin-1, Doxorubicin, Paclitaxel, 5-fluorouracil, anti-β-Actin (cat#A3854) antibody, Doxycycline, Bovine Serum Albumin (BSA), Ferrostatin-1 (Fer-1), Thapsigargin, Tunicamycin and Polybrene were purchased from Sigma-Aldrich. RSL3 (cat#B6095) and Erastin (cat#B1524) were purchased from APExBIO. PERK inhibitor GSK2656157 (Cat#S7033) was purchased from Selleck Chemicals LLC. Recombinant Anti-Glutathione Peroxidase 4 antibody [EPNCIR144] (cat# ab125066) obtained from Abcam. Anti-ATF6α antibody

clone# (37-1) (cat#73-505) was procured from BioAcademia. PVDF membrane and stripping buffer were obtained from Millipore Inc. BCA protein estimation kit, RIPA cell lysis buffer, blocking buffer, Super Signal West Pico and Femto chemiluminescent substrate, Lipofectamine-3000, Puromycin, FBS, RPMI-1640 media, Anti-Anti, were purchased from Thermo Fisher Scientific. Primers for real-time PCR and ChIP assay were purchased from IDT Inc and Eurofins Scientific. All chemicals were purchased from Sigma or Thermo scientific unless specified otherwise. Antibodies were obtained from cell signaling technology (CST) or mentioned otherwise.

Cell Culture

Colorectal cancer cell lines HT29, SW620, DLD1, and HCT116 were obtained from American Type Culture Collection (ATCC), USA. Mycoplasma-free early passage cells were resuscitated from liquid nitrogen vapor stocks and inspected microscopically for stable phenotype before use. HT29, DLD1, and HCT116 cells were cultured in RPMI-1640 medium containing 10% fetal bovine serum (Gibco/Invitrogen), supplemented with anti-anti (Invitrogen containing 100 μg/ml streptomycin, 100 unit/ml penicillin, and 0.25 μg/ml amphotericin B). SW620 cells were cultured in DMEM medium containing 10% fetal bovine serum (Gibco/Invitrogen), supplemented with anti-anti. RPMI-1640 L-cysteine, L-cystine, L-glutamine and L-methionine free media (MP Biomedicals) was used to culture HT29 cells in cystine-free conditions. STR profiling was performed to authenticate all the cell lines employed in the investigation. Cell lines were cultured in an Eppendorf Galaxy 170R/170S CO2 incubator to provide a stable and homogeneous 5% CO_2 and 37ºc temperature and humid atmosphere required for cell culture.

Cytotoxicity assay (SRB assay)

In-vitro cytotoxic effects of RSL3, Paclitaxel, Doxorubicin, 5-Fluorouracil, and Oxaliplatin were assessed with standard SRB (Sulforhodamine B) assay as described before [59,60]. Following an incubation period of 48 hours, cell monolayers were fixed with 10% (wt/vol) trichloroacetic acid and stained for 30 minutes before being washed repeatedly with 1% (vol/vol) acetic acid to remove excess color. The protein-bound dye was dissolved in a 10 mM Tris base solution, and the absorbance of the treated and untreated cells was measured on a multi-well scanning spectrophotometer (Epoch Microplate Reader, Biotek, USA) at a wavelength of 510 nm. All the calculations for percent inhibition and IC50 were done in excel.

Western blotting

After harvesting, the cells or tissues were lysed on ice with Pierce™ RIPA lysis solution for 30 minutes. The Pierce™ BCA protein assay kit was used to estimate the protein concentration of the lysates. An equal quantity of the protein was resolved in a 4–15% Mini-PROTEAN® TGX™ Precast Protein Gels and transferred to an Immun-Blot PVDF Membrane (Bio-Rad) for antibody incubation. After transfer, the PVDF membrane was blocked with 5% non-fat dry milk or 5% BSA, followed by incubation with appropriate dilutions (manufacturer's protocol) of primary antibodies overnight at 4°C. After 3 washes for 5 minutes each, the membrane was incubated with a 1:5000 dilution of horseradish peroxidase-conjugated secondary antibody for 1 hour at room temperature. Immunoreactivity was detected by enhanced chemiluminescence solution (Bio-Rad Clarity Western ECL Substrate and Immobilon™ western, Millipore, USA) and scanned by the gel documentation system (Bio-Rad chemidoc XRS plus).

Flow cytometry

We used flow cytometry to assess the cytotoxic effect of RSL3, Paclitaxel, Doxorubicin, 5-Fluorouracil, Oxaliplatin in HT29 EV (untagged) and PERK knockdown cells (pUltra-Chili-Luc-red). In brief, 6 lacs cells/well were seeded in 6-well plates and allowed to grow with treatment or vehicle control. Cells were harvested with TrypLE (Invitrogen) for single-cell suspension in FACS buffer (PBS with 0.1% BSA and 1mM EDTA). After washing and centrifugation, cell pellets were

resuspended in FACS buffer and analysed by FACS Calibur (BD). Acquired data were analysed using FlowJo software (Treestar).

BODIPY 581/591 C11 Assay

BODIPY 581/591 C11 (Invitrogen) is a lipid-soluble fluorescent indicator of lipid peroxidation. Upon oxidation, its excitation maximum shifts from 581 to 500 nm, and the emission maximum shifts from 591 to 510 nm. To estimate lipid peroxidation in vitro, 6 lacs cells per well were seeded in 6-well plates and treated with RSL3 for 6 hours or mentioned otherwise. After completion of treatment, cells were incubated with 5μM BODIPY C11 in the CO_2 incubator for 30 minutes. After incubation, cells were harvested with TrypLE, washed with DPBS, and analysed by FACS Calibur (BD). Acquired data were analysed using FlowJo software.

Generation of stable cell lines by lentiviral transduction

3rd generation lentiviral vector pUltra-Chili-Luc (addgene no. 48688) with the bi-cistronic expression of tdTomato and luciferase was used to make HT29 cells fluorescent tagged. Lentiviral particles were generated in HEK-293T cells. Transduction was carried out in the presence of Polybrene (8 μg/ml). A population of transduced cells (HT29-Chili-Luc) was identified by chilli red expression and sorted by flow cytometry. For *PERK, SLC7A11*, and *ATF4* knockdown generation, shRNA sequences were cloned into the 3rd generation transfer plasmid pLKO.1 TRC cloning vector (Addgene cat no. 10878) between unique AgeI and EcoRI sites downstream of the U6 promoter. HEK-293T cell line was used to generate lentiviral particles using the transfection reagent Lipofectamine 3000. The media containing the viral particles was supplemented with Polybrene (8 μg/ml) for transduction. Cells were subjected to puromycin selection after 48 hours of transduction, and the knockdown profile of PERK, SLC7A11, and ATF4 was confirmed after 1 week of selection via western blot. Following oligo sequences were used to clone *PERK, SLC7A11* and *ATF4* shRNA in pLKO.1 plasmid-

Gene name	shRNA sequence (5'- 3')
PERK	CCGGGGAACGACCTGAAGCTATAAACTCGAGTTTATAGCTTCAGGTCGTTCCTTTTTG
SLC7A11	CCGGCCTGTCACTATTTGGAGCTTTCTCGAGAAAGCTCCAAATAGTGACAGGTTTTTG
ATF4	CCGGGCCTAGGTCTCTTAGATGATTCTCGAGAATCATCTAAGAGACCTAGGCTTTTTG

Generation of stable SLC7A11 overexpression cell lines

The SLC7A11 ORF was amplified from the cDNA of the total RNA of HEK293 cells. The amplified product and pLJM1-EGFP (Plasmid #19319) were further digested with NheI and AgeI restriction enzymes to produce sticky ends on both. After cloning, HEK293T cells were used for viral soup generation. The Viral particles in the presence of Polybrene (8 μg/ml) were added to culture plates containing HT29 EV and PERK KD cells. Transformed cells were cultured for 3 days, and EGFP-positive cells were sorted in BD FACSAria. After culturing the cells for 1-week cells were subjected to western blot analysis to confirm the expression of SLC7A11. The Following primer sets were used to amplify the SLC7A11 ORF from HEK293 cells-

Primer	primer sequence (5'- 3')
Forward	AGAGGCTAGCATGGTCAGAAAGCCTGTTGTGT
Reverse	TATTACCGGTTCATAACTTATCTTCTTCTGGT

Real-time quantitative PCR (RT-qPCR)

Total RNA was isolated from the cultured cells and tissues using the standard procedure of the RNeasy Mini Kit (Qiagen, cat no.74104). The concentration and purity of the RNA samples were

determined using nanodrop. The total RNA (1µg) of each sample was reverse-transcribed (RT) with random hexamer according to the manufacturer's protocol (Verso cDNA synthesis kit). The final cDNA was diluted with nuclease-free water (1:5), and 10ng of diluted cDNA was used for each reaction in real-time PCR. Real-time PCR was carried out using an ABI 7500 Real-Time PCR System (Applied Biosystems). Reactions for each sample were performed in triplicate. 18s amplification was used as the housekeeping gene control. The Standard delta-delta Ct method was used to calculate the relative fold change in gene expression. For amplifying *PERK*, *ATF4*, and *SLC7A11*, we performed SYBR Green-based RT-PCR following the manufacturer's (PowerUp SYBR Green ABI) instructions.

Chromatin Immunoprecipitation (ChIP) Assay

Following the manufacturer's protocol, ChIP assay was conducted using the CUT&RUN Assay Kit (cat# 86652 Cell Signaling Technology). In brief, cells at 80% confluency were fixed with 1% formaldehyde for 10 minutes. Cells were then centrifuge washed, followed by lysis in 200µl of membrane extraction buffer containing protease inhibitor cocktail. The cell lysates were digested with MNase for 30 minutes at 37°C to get chromatin fragments of 100-500 bp long DNA fragments. Incubation with ATF4 rabbit monoclonal primary antibody, normal IgG, and anti-histone 3 (H3) was done overnight at 4ºC. After washing with the wash buffer three times, elution of chromatin from Antibody/Protein A Magnetic beads and reversal of cross-linking was carried out by heat. Spin columns purified DNA then used for SYBR Green-based real-time PCR. The following primers were used to amplify the -328bp site on *SLC7A11* promoter forward primer- 5'CTACTCACAAAACAGTCGCA3', reverse primer- 5'GCAACTCGTAGTGAGCAACAA3', and -494bp and -447bp sites were amplified using forward primer- 5'ATTGGATTTGACTGTATTGCCTT3' and reverse primer- 5'CATTGTTTATAACAACACAGTTTGA3'.

Cloning of *SLC7A11* promoter in luciferase reporter vector and luciferase assay

The following primers were used to PCR amplify the *SLC7A11* promoter -0.6 kb upstream of the TSS from the HEK293 cell line- forward primer- 5'TCGGCTAGCGAGGAAGGCTTATAGTTGTGTGTATGTGAC3', reverse primer- 5'AGCCTCGAGCAGCTCAGCTTCCTCATGGGC3'. The amplified fragments were cloned into the PGL4.12 [luc2 CP] vector between the NheI and XhoI restriction sites. HT29 cells were seeded in a 6-well plate upto 50-60% confluency and transfected with 2.5µg of cloned PGL4.12 and 50ng of PGL4 (hRluc-CMV) plasmid using lipofectamine-3000 as transfection reagent (Invitrogen). The transfected cells with cloned pGL4.12 and pGL4 (hRluc-CMV) were treated with vehicle control or two doses (5µM and 1µM) of PERK inhibitor (GSK2656157) or RSL3 (500nM and 1µM) for 24 hours. Cells were lysed with 100µL of lysis buffer provided with the Dual-Glo Luciferase assay kit (Promega). The GloMax® 96 Microplate Luminometer was used to measure the activity of Firefly and Renilla luciferases according to the manufacturer's protocol (Promega). For each sample, firefly luciferase activity was normalised to Renilla luciferase activity, and fold change in luciferase activity in different treatment groups was calculated.

In vivo studies in xenograft tumor models

All animal studies were conducted following standard principles and procedures approved by the Institutional Animal Ethics Committee (IAEC) of CSIR-Central Drug Research Institute. All the animals were maintained in a pathogen-free facility under a day-night cycle. Mice were randomly assigned to groups by a blinded independent investigator. Following our well-established colorectal cancer xenograft models[3], we inoculated 2×10^6 cells (HT29 EV and HT29 PERK KD each) in 100µl PBS subcutaneously into the flanks of the left or right hind leg of each 4–6 weeks old nude Crl: CD1-Foxn1^{nu} mice. Throughout the study, the tumors were measured with an electronic vernier caliper at regular intervals, and the tumor volumes were calculated using the standard formula V =

(W (2) × L)/2, where 'W' is the short and 'L' is the long tumor axis. At the end of the experiment, mice were sacrificed, and subcutaneous tumors were dissected for further studies.

Immunohistochemistry of tumor tissues

Harvested tumors were fixed in 10% neutral buffered formalin (NBF), and paraffin blocks were prepared for sectioning. For staining, tissue sections were deparaffinised and rehydrated by passing through serial dilutions of xylene and ethanol. Antigen retrieval was performed in 10mM sodium citrate buffer (pH 6.2) by heating at 95°C for 20-30 minutes. Processed slides were washed in PBS for 5 minutes. We used VECTASTAIN ABC KIT (VECTOR laboratories) for IHC staining. ImmEdge pen (hydrophobic barrier pen), and Bloxall blocking solution, were purchased from Vector Laboratories, Inc. Fluorochrome conjugated secondary antibodies, ProLong™ Gold Antifade Mountant, were purchased from molecular Probes-Invitrogen. The endogenous peroxide activity was neutralised by incubating the slides with BLOXALL blocking solution for 10 minutes. After washing, tissue sections were incubated with diluted normal blocking buffer for 20 minutes to prevent non-specific staining. The sections were incubated overnight at 4°C with primary antibodies of 4-HNE and MDA diluted in buffer (1:100). The sections were incubated with biotinylated secondary antibody for 1 hour, followed by VECTASTAIN ABC Reagent for 30 minutes. Slides were incubated with diaminobenzidine (DAB) as a chromogen and counterstained with hematoxylin. Negative control sections were processed in parallel without the primary antibody incubation. The sections were dehydrated and mounted using DPX (Sigma). Stained sections were examined under a microscope (EVOS XL core) under 10x and 40x magnification. ImageJ software was used for scoring 4-HNE and MDA staining. The color deconvolution tool split the IHC images into three color images separately, showing different staining intensities. After adjusting the threshold, images were changed in binary. Analyse the particle tool was used to get the average value of pixels in the DAB channel. ATM score was calculated following the standard formula (Refs) ATM Score = 1/255 (the average value of all the pixels in the DAB channel), where ATM stands for Average Threshold Measure, and 255 is the value of maximum staining intensity [61,62].

Analysis of TCGA colorectal cancer dataset

Illumina HiSeq mRNA data from GDC TCGA colorectal Cancer (n=471) was downloaded from the TCGA portal for *PERK* and *SLC7A11* genes using the UCSC Xena browser (https://xena.ucsc.edu) [63]. Log2 (fpkm-uq + 1) values for *PERK* and *SLC7A11* were used to draw a scatter plot. Pearson's correlation coefficient (r) and p-value were calculated in excel.

Patient samples collection and RNA isolation

Patient samples were scrutinised following the set criteria. A total of 15 CRC tumors with paired normal colorectal mucosa samples were collected from RGCIRC (Rajiv Gandhi Cancer Institute and Research Centre), India, from 2016 to 2019. It was ensured that the tumor was sporadic and the patient had not received chemotherapy or radiotherapy before surgery. The pathologist ensured the total oncogenic area of cancerous cells was not less than 80%. Informed consent was obtained from each patient. The ethical approval of the study was approved by the Institute Ethics Committee, Motilal Nehru National Institute of Technology Allahabad (Ref. No. IEC17-18/027). Total RNA was extracted from tumor tissues using RNeasy Mini Kit (Qiagen, cat no.74104), and RNA concentration and quality were estimated using nanodrop (BioTek Take3). The cDNA preparation and RT-PCR analysis were done as described above.

Statistics

In the figure legends, most in vitro experiments represent at least two or more independent experiments or specified otherwise. Student's t-test was used to examine statistically significant differences for two-group analysis. All data are presented as means ± SD or SEM. These analyses

were done with Graph-Pad Prism software. Results were considered statistically significant when p values ≤ 0.05 between groups.

Author Contributions: KKS was involved in study designing, performed experiments and wrote the draft manuscript. MPS performed bioinformatic analysis. PC, ABS, MAK AV, MAN, SRS, SM, and AS helped in carrying out in vitro and in vivo studies. SS provided support for patient sample data generation. JS helped in animal maintenance and experimentation. DD conceived the idea, designed experiments, analysed data, wrote the manuscript and provided overall supervision. All authors read and approved the final manuscript.

Conflict of Interest: The authors declare no conflict of interest related to this manuscript.

Figure legends

Figure 1: Ferroptosis inducer RSL3 causes UPR and the PERK arm of UPR regulates SLC7A11 expression

(A-D) HT29, SW620, DLD1 and HCT116 cells were either treated with 1μM RSL3 or vehicle control (VC) for 24 hours and protein lysates were prepared for western blot analysis. Immunoblot shows the expression for classical UPR marker proteins, i.e., PERK, ATF6, and IRE1α. Full-length ATF6 (ATF6-FL), membrane-associated ATF6 (ATF6-P), and nuclear-translocated S2P-cleaved ATF6 (ATF6-N) all are indicated in the immunoblot. (E) Major ferroptosis regulator proteins GPx4, SLC7A11, and ACSL4 in HT29 cells. (F-H) Immunoblot analysis of PERK, ATF6, IRE1α, SLC7A11, GPx4, and ACSL4 in (F) PERK knockdown (KD), (G) ATF6 KD and (H) IRE1α KD in HT29 cells with respective empty vector (EV). (I) Immunoblot showing the expression of PERK and SLC7A11 in EV and PERK KD HT29 cells that were either treated with vehicle or 1μM RSL3 for 6 hours. (J-K) Immunoblot analysis of PERK and SLC7A11 in (J) VC and 5μM PERK inhibitor (GSK2656157) treated and (K) VC, PERK inhibitor and RSL3 treated HT29 cells. (L-M) EV and PERK KD, (N-O) VC and PERK inhibitor treated HT29 (L, N) and SW620 (M, O) cells were cultured in RPMI 1640 in the presence (cystine+) or absence (cystine-) of cystine for 72 hours and subjected to Western blot analysis (left) for the expression of PERK and SLC7A11, quantitative analysis (right) of percent area covered by the cultured cells are shown in the graph (Original photomicrographs are shown in Supplementary Figure 5). *p < 0.05; compared to control. β-actin was used as a loading control in all immunoblot studies. Respective molecular weight marker (left of each immunoblot) and densitometric quantifications (bottom of each immunoblot) are shown.

Figure 2: Loss of PERK function promotes ferroptosis in colorectal cancer

(A) HT29 EV, PERK, ATF6, and IRE1α KD cells were treated with either vehicle or 1μM RSL3 for 48 hours, and SRB assay was performed to evaluate the cytotoxic effect of the same. (B) SW620 EV and PERK KD cells were treated with vehicle or 1μM RSL3 for 48 hours, and subjected to SRB assay. For A and B, percent growth inhibition was tabulated. *p < 0.05; compared to respective EV.

(C) HT29 EV (untagged) and chilli-tagged PERK KD (red) cells were mixed in equal numbers and subjected to flow cytometric analysis on day 0 and day 3 following treatment with vehicle control or 500nM RSL3. Analysed cell populations are shown in the FACS plot. (D) Different CRC cells were treated with RSL3 (HT29 and SW620 - 1μM), (DLD1 - 125nM), and (HCT116 - 2μM) alone or in combination with 5μM of PERK inhibitor (GSK2656157) for 48 hours and SRB assay was performed. Percent growth inhibition was tabulated. $*p < 0.05$; compared to RSL3 treated cells. (E) HT29 cells were treated with vehicle control or 10nM Thapsigargin or 1μg/ml Tunicamycin for 48 hours and subjected to SRB assay. Percent growth inhibition was calculated and tabulated in columns. $*p < 0.05$; compared to respective controls. (F) HT29 EV and PERK KD cells were treated with vehicle control or different chemotherapeutic drugs i.e., paclitaxel (20nM), 5-Fluorouracil (100μM), Doxorubicin (10μM), Oxaliplatin (50μM) for 48 hours and cytotoxic impact of these drugs was evaluated via SRB assay. Percent growth inhibition was tabulated in the columns. (G) HT29 EV and PERK KD cells were treated either with either 1μM RSL3 alone or in combination with (25μM) Z-VAD-FMK (pan-caspase inhibitor) or (10μM) ferrostatin-1 (ferroptosis inhibitor) and percent growth inhibition in different groups was estimated by SRB assay. $*p < 0.05$; compared to respective RSL3 control. In A-B and D-G Columns represent an average of triplicate readings of samples; error bars ± S.D. (H-I left panel) Control (EV) and PERK KD of (H) HT29 and (I) SW620 cells were treated with 1μM RSL3 or vehicle control for 24 hours followed by BODIPY C11 staining (Lipid peroxidation sensor) and cells were analysed by FACS (detailed description provided in materials and methods section). Histogram overlays show BODIPY C11 positivity correlating with lipid peroxidation levels in respective groups. (H-I) Right Panels, respective delta mean fluorescence intensity (MFI) of the cells, stained for BODIPY C11. The delta mean was calculated by subtracting the mean fluorescence intensity of the control from the RSL3 treated cells. Columns represent an average of duplicate readings of samples; error bars ± S.D. $*p < 0.05$; compared to EV (control). (J-K) Immunoblots representing 4-Hydroxynonenal (4-HNE) and malondialdehyde (MDA) conjugated protein expression in (J) HT29 EV and PERK KD cells and (K) HT29 VC and PERK inhibitor-treated (24 hours) cells. β-actin was used as a loading control in all immunoblot studies. Respective molecular weight marker (left of each immunoblot) and densitometric quantifications (bottom of each immunoblot) are shown.

Figure 3: PERK-ATF4 axis regulates *SLC7A11* expression and colorectal cancer cell ferroptosis

(A) Total RNA was isolated from control and RSL3 treated HT29 cells, reverse transcribed, and subjected to qRT-PCR analysis for *PERK, ATF6* and *IRE1α* mRNA expression. Fold change in mRNA expression is represented in the bar graph. Data is representative of three independent experiments, resulting from different samples; Columns, the fold change of mRNA expression of *PERK, ATF6* and *IRE1α* compared to respective control. (B) Control and RSL3 treated HT29 cells were subjected to qRT-PCR analysis as described above for expression of the *SLC7A11* gene. Columns represents fold change in mRNA expression of *SLC7A11*; bars ± SD. *, $p < 0.05$, compared with control. (C) HT29 cells were pre-treated for 30 minutes with 10μM Ferrostatin-1 (ferroptosis inhibitor) and further treated with 1μM RSL3 alone or in combination with FER-1. Immunoblot analysis shows the expression of PERK, Bip/GRP78, and ATF4. (D) HT29 cells were treated with Thapsigargin (ER stress inducer) alone or with PERK inhibitor (pre-treated for 2 hours) for 6 hours and subjected to western blot analysis. The expression of PERK, ATF4, and SLC7A11 is shown in the immunoblot images. (E-F) Immunoblots show the expression of PERK, ATF4, and SLC7A11 in (E) HT29 EV and PERK KD or (F) HT29 EV and ATF4 KD cells. (G) qRT-PCR analysis of HT29 EV and PERK KD cells; Columns showing the fold change in mRNA expression of *PERK* and *SLC7A11* genes. bars ± SD. *, $p < 0.05$, compared with respective control. (H) Diagrammatic representation of *SLC7A11* promotor showing (Top) putative ATF4 DNA binding sites and

transcription start site (TSS) with RNA pol II, (Down) Human ATF4 binding motif of *SLC7A11* promoter on predicted binding site (-0.3kb upstream from TSS) that is publicly available at JASPAR database (http://www.jaspar.genereg.net). (I) ChIP assay (Details described in the Methods section) was performed in vehicle control, and PERK inhibitor-treated (24 hours) HT29 cells using anti-ATF4 and IgG antibodies and then examined by real-time qPCR using primer pairs targeting predicted -0.3 kb and -0.5kb ATF4 binding sites upstream from TSS of the *SLC7A11* gene. Fold change in enrichment for ATF4 and IgG with respect to % input was shown; Data is representative of three independent experiments resulting from different samples; Columns, the average value of percentage enrichment compared to input; bars ± SD. *, p < 0.05, compared with respective control. Photomicrograph of Gel showing conventional PCR validation of ChIP experiments. Lanes are vehicle control and treatment, respectively, for each group of the ChIP sample. (J) The HEK293 cells were transfected with -0.6kb upstream of *SLC7A11* promoter luciferase construct plasmid (pGL4.12) followed by treatment with vehicle or 1μM and 5μM of PERK inhibitor for 24 hours and cells were harvested for luciferase activity (detailed description in Methods Section). Columns, the average value of relative firefly luciferase activity compared to Renila luciferase activity derived from triplicate readings of different samples; bars ± SD. **, p < 0.01, compared with vehicle control. (K) HT29 cells were treated with vehicle control or 1μM of RSL3, and ChIP assay was performed using anti-ATF4 and IgG antibodies and then examined by real-time qRT-PCR using primer pairs targeting the predicted ATF4 binding sites on the *SLC7A11* promoter. Fold change enrichment for ATF4 and IgG with respect to % input was shown in Columns; bars ± SD. *, p < 0.05, compared with vehicle control. (L) The HEK293 cells were transfected with -0.6kb upstream of *SLC7A11* promoter luciferase construct plasmid, followed by treatment with vehicle or 500nM and 1μM of RSL3 for 24 hours, and subjected to luciferase activity. Columns, the average value of relative firefly luciferase activity compared to Renila luciferase activity derived from triplicate readings of different samples. (M) HT29 EV and ATF4 KD cells were treated with 1μM RSL3 for 48 hours, and SRB assay was performed. Percent growth inhibition was tabulated, Columns, an average of triplicate readings of samples; error bars ± S.D. *p < 0.05; compared to EV. (N) HT29 EV and ATF4 KD cells were treated with 1μM RSL3 for 6 hours and analysed by flow cytometry after staining with BODIPY C11. Histogram overlays show lipid peroxidation levels in respective treatment groups. (O) EV and PERK KD HT29 cells were made stable for overexpression of SLC7A11 and subjected to immunoblot analysis for SLC7A11 and PERK. (P) HT29 EV and PERK KD cells with stable SLC7A11 overexpression (as shown in the immunoblot) were treated with 1μM RSL3 for 48 hours and subjected to SRB assay. Percent growth inhibition was tabulated, Columns, an average of triplicate readings of samples; error bars ± S.D. *p < 0.05; compared to respective control. β-actin was used as a loading control in all immunoblot studies. Respective molecular weight marker (left of each immunoblot) and densitometric quantifications (bottom of each immunoblot) are shown.

Figure 4: Loss of PERK has compromised in vivo colorectal tumor growth due to increased ferroptosis

2×10^6 HT29 EV and PERK KD cells in 100μl PBS were injected subcutaneously in the flanks of the right hind leg of 4–6 weeks old Crl: CD1-Foxn1nu mice in two different groups for each condition. Tumor volumes were measured twice a week with a caliper. (A) Tumor progression of the same is shown in the graph. Each point indicates the average tumor volumes at a particular time; error bars ± SEM (n = 4 for each group); *p < 0.05 compared to control tumors. (B) Photographs of tumor-bearing mice (top) and harvested tumors (bottom) from respective groups were shown. (C) The average tumor weight of each group is shown in the graph. error bars ± SEM (n = 4 for each group); *p < 0.05 compared to control tumors. (D) Harvested tumors were lysed and subjected to western blot analysis to visualize the protein expression of PERK SLC7A11, ATF4, MDA (malondialdehyde) and 4-HNE (4-Hydroxynonenal). β-actin and GAPDH were used as loading

control in immunoblot studies. Respective molecular weight marker (left of each immunoblot) and densitometric quantifications (bottom of each immunoblot) are shown. Respective molecular weight marker (right) and densitometric quantifications (below) are shown for respective blots of all Western blot images. (E) Immunohistochemistry was conducted to detect MDA and 4-HNE in formalin-fixed paraffin-embedded serial sections of harvested tumors with respective antibodies. Representative photomicrographs are shown at 10X and 40X magnifications. Scale bar, 50μm (10X) or 15μm (40X). (F-G) Quantitative ATM scores for the expression of (F) MDA and (G) 4-HNE are represented as scatter plots; Error bar, +/- SEM, *p-value, <0.05, compared to expression in control tumors.

Figure 5: PERK (*EIF2AK3*) and *SLC7A11* are positively correlated in human colorectal tumors

(A) GDC TCGA COAD patient data were acquired from the Xena browser, and a correlation graph was plotted between *EIF2AK3* (PERK) and *SLC7A11*. R (Pearson's correlation coefficient) (B) RT-PCR in matched non-malignant (Normal) and malignant tumor samples of colorectal cancer patients showed the correlation between delta Ct of *EIF2AK3* (PERK) and *SLC7A11*. (C-D) Total RNA was isolated from colorectal cancer patient tumor tissue samples along with their respective matched non-malignant counterparts, reverse transcribed, and RT-qPCR was performed for *PERK* and *SLC7A11* expression analysis. 18s is used as an internal control. Fold change in mRNA expression in (C) *PERK* and (D) *SLC7A11* is shown in bar diagram; Columns, the average value of fold change as compared to control; error bars ± SEM. *, $p < 0.05$, compared to control, n = 15. (E) The findings are illustrated in a graphical abstract showing how selectively PERK arm of ER stress regulates ferroptosis in colorectal cancer.

References:

[1] H. Sung, J. Ferlay, R.L. Siegel, M. Laversanne, I. Soerjomataram, A. Jemal, F. Bray, Global Cancer Statistics 2020: GLOBOCAN Estimates of Incidence and Mortality Worldwide for 36 Cancers in 185 Countries, CA Cancer J Clin. 71 (2021) 209–249. https://doi.org/10.3322/CAAC.21660.

[2] A.K. Singh, R.K. Arya, S. Maheshwari, A. Singh, S. Meena, P. Pandey, O. Dormond, D. Datta, Tumor heterogeneity and cancer stem cell paradigm: Updates in concept, controversies and clinical relevance, Int J Cancer. 136 (2015) 1991–2000. https://doi.org/10.1002/IJC.28804.

[3] M.A. Nengroo, S. Maheshwari, A. Singh, A. Verma, R.K. Arya, P. Chaturvedi, K.K. Saini, A.K. Singh, A. Sinha, S. Meena, A. Gupta, A. Mishra, J. Sarkar, D. Datta, CXCR4 intracellular protein promotes drug resistance and tumorigenic potential by inversely regulating the expression of Death Receptor 5, Cell Death Dis. 12 (2021). https://doi.org/10.1038/S41419-021-03730-8.

[4] A.K. Singh, A. Verma, A. Singh, R.K. Arya, S. Maheshwari, P. Chaturvedi, M.A. Nengroo, K.K. Saini, A.L. Vishwakarma, K. Singh, J. Sarkar, D. Datta, Salinomycin inhibits epigenetic modulator EZH2 to enhance death receptors in colon cancer stem cells, Epigenetics. 16 (2021) 1–18. https://doi.org/10.1080/15592294.2020.1789270.

[5] A. Verma, A. Singh, M.P. Singh, M.A. Nengroo, K.K. Saini, S.R. Satrusal, M.A. Khan, P. Chaturvedi, A. Sinha, S. Meena, A.K. Singh, D. Datta, EZH2-H3K27me3 mediated KRT14 upregulation promotes TNBC peritoneal metastasis, Nat Commun. 13 (2022). https://doi.org/10.1038/S41467-022-35059-X.

[6] M.J. Hangauer, V.S. Viswanathan, M.J. Ryan, D. Bole, J.K. Eaton, A. Matov, J. Galeas, H.D. Dhruv, M.E. Berens, S.L. Schreiber, F. McCormick, M.T. McManus, Drug-tolerant persister cancer cells are vulnerable to GPX4 inhibition, Nature 2017 551:7679. 551 (2017) 247–250. https://doi.org/10.1038/nature24297.

[7] V.S. Viswanathan, M.J. Ryan, H.D. Dhruv, S. Gill, O.M. Eichhoff, B. Seashore-Ludlow, S.D. Kaffenberger, J.K. Eaton, K. Shimada, A.J. Aguirre, S.R. Viswanathan, S. Chattopadhyay, P. Tamayo, W.S. Yang, M.G. Rees, S. Chen, Z. v. Boskovic, S. Javaid, C. Huang, X. Wu, Y.Y. Tseng, E.M. Roider, D.

Gao, J.M. Cleary, B.M. Wolpin, J.P. Mesirov, D.A. Haber, J.A. Engelman, J.S. Boehm, J.D. Kotz, C.S. Hon, Y. Chen, W.C. Hahn, M.P. Levesque, J.G. Doench, M.E. Berens, A.F. Shamji, P.A. Clemons, B.R. Stockwell, S.L. Schreiber, Dependency of a therapy-resistant state of cancer cells on a lipid peroxidase pathway, Nature. 547 (2017) 453–457. https://doi.org/10.1038/nature23007.

[8]   S.J. Dixon, K.M. Lemberg, M.R. Lamprecht, R. Skouta, E.M. Zaitsev, C.E. Gleason, D.N. Patel, A.J. Bauer, A.M. Cantley, W.S. Yang, B. Morrison, B.R. Stockwell, Ferroptosis: An Iron-Dependent Form of Nonapoptotic Cell Death, Cell. 149 (2012) 1060–1072. https://doi.org/10.1016/J.CELL.2012.03.042.

[9]   B.R. Stockwell, Ferroptosis turns 10: Emerging mechanisms, physiological functions, and therapeutic applications, Cell. 185 (2022) 2401–2421. https://doi.org/10.1016/J.CELL.2022.06.003.

[10]   J.P. Friedmann Angeli, M. Schneider, B. Proneth, Y.Y. Tyurina, V.A. Tyurin, V.J. Hammond, N. Herbach, M. Aichler, A. Walch, E. Eggenhofer, D. Basavarajappa, O. Rådmark, S. Kobayashi, T. Seibt, H. Beck, F. Neff, I. Esposito, R. Wanke, H. Förster, O. Yefremova, M. Heinrichmeyer, G.W. Bornkamm, E.K. Geissler, S.B. Thomas, B.R. Stockwell, V.B. Odonnell, V.E. Kagan, J.A. Schick, M. Conrad, Inactivation of the ferroptosis regulator Gpx4 triggers acute renal failure in mice, Nat Cell Biol. 16 (2014) 1180–1191. https://doi.org/10.1038/ncb3064.

[11]   S.J. Dixon, D. Patel, M. Welsch, R. Skouta, E. Lee, M. Hayano, A.G. Thomas, C. Gleason, N. Tatonetti, B.S. Slusher, B.R. Stockwell, Pharmacological inhibition of cystine-glutamate exchange induces endoplasmic reticulum stress and ferroptosis, Elife. 2014 (2014). https://doi.org/10.7554/ELIFE.02523.

[12]   H. Yuan, X. Li, X. Zhang, R. Kang, D. Tang, Identification of ACSL4 as a biomarker and contributor of ferroptosis, Biochem Biophys Res Commun. 478 (2016) 1338–1343. https://doi.org/10.1016/j.bbrc.2016.08.124.

[13]   I. Ingold, C. Berndt, S. Schmitt, S. Doll, G. Poschmann, K. Buday, A. Roveri, X. Peng, F. Porto Freitas, T. Seibt, L. Mehr, M. Aichler, A. Walch, D. Lamp, M. Jastroch, S. Miyamoto, W. Wurst, F. Ursini, E.S.J. Arnér, N. Fradejas-Villar, U. Schweizer, H. Zischka, J.P. Friedmann Angeli, M. Conrad, Selenium Utilization by GPX4 Is Required to Prevent Hydroperoxide-Induced Ferroptosis, Cell. 172 (2018) 409-422.e21. https://doi.org/10.1016/j.cell.2017.11.048.

[14]   W.S. Yang, B.R. Stockwell, Synthetic Lethal Screening Identifies Compounds Activating Iron-Dependent, Nonapoptotic Cell Death in Oncogenic-RAS-Harboring Cancer Cells, Chem Biol. 15 (2008) 234–245. https://doi.org/10.1016/J.CHEMBIOL.2008.02.010.

[15]   P. Koppula, L. Zhuang, B. Gan, Cystine transporter SLC7A11/xCT in cancer: ferroptosis, nutrient dependency, and cancer therapy, Protein Cell. 12 (2021) 599–620. https://doi.org/10.1007/s13238-020-00789-5.

[16]   H. fa Yan, T. Zou, Q. zhang Tuo, S. Xu, H. Li, A.A. Belaidi, P. Lei, Ferroptosis: mechanisms and links with diseases, Signal Transduct Target Ther. 6 (2021). https://doi.org/10.1038/S41392-020-00428-9.

[17]   Y. Xie, W. Hou, X. Song, Y. Yu, J. Huang, X. Sun, R. Kang, D. Tang, Ferroptosis: process and function, Cell Death Differ. 23 (2016) 369–379. https://doi.org/10.1038/CDD.2015.158.

[18]   X. Wu, Y. Li, S. Zhang, X. Zhou, Ferroptosis as a novel therapeutic target for cardiovascular disease, Theranostics. 11 (2021) 3052–3059. https://doi.org/10.7150/THNO.54113.

[19]   G. Wu, Y.Z. Fang, S. Yang, J.R. Lupton, N.D. Turner, Glutathione Metabolism and Its Implications for Health, J Nutr. 134 (2004) 489–492. https://doi.org/10.1093/JN/134.3.489.

[20]   S. Doll, B. Proneth, Y.Y. Tyurina, E. Panzilius, S. Kobayashi, I. Ingold, M. Irmler, J. Beckers, M. Aichler, A. Walch, H. Prokisch, D. Trümbach, G. Mao, F. Qu, H. Bayir, J. Füllekrug, C.H. Scheel, W. Wurst, J.A. Schick, V.E. Kagan, J.P.F. Angeli, M. Conrad, ACSL4 dictates ferroptosis sensitivity by shaping cellular lipid composition, Nat Chem Biol. 13 (2017) 91–98. https://doi.org/10.1038/nchembio.2239.

[21]   Y.S. Lee, D.H. Lee, H.A. Choudry, D.L. Bartlett, Y.J. Lee, 47, Molecular Cancer Research. 16 (2018) 1073–1076. https://doi.org/10.1158/1541-7786.MCR-18-0055.

[22]   D. Ron, P. Walter, Signal integration in the endoplasmic reticulum unfolded protein response, Nat Rev Mol Cell Biol. 8 (2007) 519–529. https://doi.org/10.1038/NRM2199.

[23] S. Wang, R.J. Kaufman, The impact of the unfolded protein response on human disease, J Cell Biol. 197 (2012) 857–867. https://doi.org/10.1083/JCB.201110131.

[24] P. Walter, D. Ron, The unfolded protein response: from stress pathway to homeostatic regulation, Science. 334 (2011) 1081–1086. https://doi.org/10.1126/SCIENCE.1209038.

[25] D. Pincus, M.W. Chevalier, T. Aragón, E. van Anken, S.E. Vidal, H. El-Samad, P. Walter, BiP binding to the ER-stress sensor Ire1 tunes the homeostatic behavior of the unfolded protein response, PLoS Biol. 8 (2010). https://doi.org/10.1371/JOURNAL.PBIO.1000415.

[26] D.T.W. Ng, P. Walter, ER membrane protein complex required for nuclear fusion, Journal of Cell Biology. 132 (1996) 499–509. https://doi.org/10.1083/jcb.132.4.499.

[27] H.P. Harding, Y. Zhang, D. Ron, Protein translation and folding are coupled by an endoplasmic-reticulum-resident kinase, Nature. 397 (1999) 271–274. https://doi.org/10.1038/16729.

[28] H. Yoshida, T. Matsui, A. Yamamoto, T. Okada, K. Mori, XBP1 mRNA is induced by ATF6 and spliced by IRE1 in response to ER stress to produce a highly active transcription factor, Cell. 107 (2001) 881–891. https://doi.org/10.1016/S0092-8674(01)00611-0.

[29] M. Calfon, H. Zeng, F. Urano, J.H. Till, S.R. Hubbard, H.P. Harding, S.G. Clark, D. Ron, IRE1 couples endoplasmic reticulum load to secretory capacity by processing the XBP-1 mRNA, Nature. 415 (2002) 92–96. https://doi.org/10.1038/415092A.

[30] K. Yamamoto, T. Sato, T. Matsui, M. Sato, T. Okada, H. Yoshida, A. Harada, K. Mori, Transcriptional induction of mammalian ER quality control proteins is mediated by single or combined action of ATF6alpha and XBP1, Dev Cell. 13 (2007) 365–376. https://doi.org/10.1016/J.DEVCEL.2007.07.018.

[31] J. Ye, R.B. Rawson, R. Komuro, X. Chen, U.P. Davé, R. Prywes, M.S. Brown, J.L. Goldstein, ER stress induces cleavage of membrane-bound ATF6 by the same proteases that process SREBPs, Mol Cell. 6 (2000) 1355–1364. https://doi.org/10.1016/S1097-2765(00)00133-7.

[32] C. Hetz, F.R. Papa, The Unfolded Protein Response and Cell Fate Control, Mol Cell. 69 (2018) 169–181. https://doi.org/10.1016/j.molcel.2017.06.017.

[33] L. Sisinni, M. Pietrafesa, S. Lepore, F. Maddalena, V. Condelli, F. Esposito, M. Landriscina, Endoplasmic reticulum stress and unfolded protein response in breast cancer: The balance between apoptosis and autophagy and its role in drug resistance, Int J Mol Sci. 20 (2019). https://doi.org/10.3390/ijms20040857.

[34] Y.S. Lee, D.H. Lee, H.A. Choudry, D.L. Bartlett, Y.J. Lee, Ferroptosis-Induced Endoplasmic Reticulum Stress: Cross-talk between Ferroptosis and Apoptosis, Mol Cancer Res. 16 (2018) 1073–1076. https://doi.org/10.1158/1541-7786.MCR-18-0055.

[35] A.M. Martinez, A. Kim, W.S. Yang, Detection of ferroptosis by BODIPY[TM] 581/591 C11, Methods in Molecular Biology. 2108 (2020) 125–130. https://doi.org/10.1007/978-1-0716-0247-8_11/COVER.

[36] A. Ayala, M.F. Muñoz, S. Argüelles, Lipid peroxidation: Production, metabolism, and signaling mechanisms of malondialdehyde and 4-hydroxy-2-nonenal, Oxid Med Cell Longev. 2014 (2014). https://doi.org/10.1155/2014/360438.

[37] H. fa Yan, T. Zou, Q. zhang Tuo, S. Xu, H. Li, A.A. Belaidi, P. Lei, Ferroptosis: mechanisms and links with diseases, Signal Transduct Target Ther. 6 (2021). https://doi.org/10.1038/s41392-020-00428-9.

[38] Z. Zhang, L. Zhang, L. Zhou, Y. Lei, Y. Zhang, C. Huang, Redox signaling and unfolded protein response coordinate cell fate decisions under ER stress, Redox Biol. 25 (2019). https://doi.org/10.1016/j.redox.2018.11.005.

[39] M. Corazzari, M. Gagliardi, G.M. Fimia, M. Piacentini, Endoplasmic Reticulum Stress, Unfolded Protein Response, and Cancer Cell Fate., Front Oncol. 7 (2017) 78. https://doi.org/10.3389/fonc.2017.00078.

[40] C. Hetz, The unfolded protein response: Controlling cell fate decisions under ER stress and beyond, Nat Rev Mol Cell Biol. 13 (2012) 89–102. https://doi.org/10.1038/nrm3270.

[41] D. Shin, E.H. Kim, J. Lee, J.L. Roh, Nrf2 inhibition reverses resistance to GPX4 inhibitor-induced ferroptosis in head and neck cancer, Free Radic Biol Med. 129 (2018) 454–462. https://doi.org/10.1016/J.FREERADBIOMED.2018.10.426.

[42] Krishan K. Saini, Priyank Chaturvedi, Ayushi Verma, Mushtaq A. Nengroo, Abhipsa Sinha, Akhilesh Singh, Sanjeev Meena, Muqtada A. Khan, Manish P. Singh, Dipak Datta. PERK arm of UPR selectively regulates ferroptosis in colon cancer cells by modulating the expression of system x_c^- (SLC7A11) [abstract]. In: Proceedings of the American Association for Cancer Research Annual Meeting 2022; 2022 Apr 8-13. Philadelphia (PA): AACR; Cancer Res 2022;82(12_Suppl):Abstract nr 6249.

[43] Y.H. Shi, Z. bin Ding, J. Zhou, B. Hui, G.M. Shi, A.W. Ke, X.Y. Wang, Z. Dai, Y.F. Peng, C.Y. Gu, S.J. Qiu, J. Fan, Targeting autophagy enhances sorafenib lethality for hepatocellular carcinoma via ER stress-related apoptosis, Autophagy. 7 (2011) 1159–1172. https://doi.org/10.4161/AUTO.7.10.16818.

[44] E. Vladykovskaya, S.D. Sithu, P. Haberzettl, N.S. Wickramasinghe, M.L. Merchant, B.G. Hill, J. McCracken, A. Agarwal, S. Dougherty, S.A. Gordon, D.A. Schuschke, O.A. Barski, T. O'Toole, S.E. D'Souza, A. Bhatnagar, S. Srivastava, Lipid peroxidation product 4-hydroxy-trans-2-nonenal causes endothelial activation by inducing endoplasmic reticulum stress, J Biol Chem. 287 (2012) 11398–11409. https://doi.org/10.1074/JBC.M111.320416.

[45] M.-H. Lin, J.-H. Yen, C.-Y. Weng, L. Wang, C.-L. Ha, M.-J. Wu, Lipid peroxidation end product 4-hydroxy-trans-2-nonenal triggers unfolded protein response and heme oxygenase-1 expression in PC12 cells: Roles of ROS and MAPK pathways., Toxicology. 315 (2014) 24–37. https://doi.org/10.1016/j.tox.2013.11.007.

[46] Y. Chen, Y. Mi, X. Zhang, Q. Ma, Y. Song, L. Zhang, D. Wang, J. Xing, B. Hou, H. Li, H. Jin, W. Du, Z. Zou, Dihydroartemisinin-induced unfolded protein response feedback attenuates ferroptosis via PERK/ATF4/HSPA5 pathway in glioma cells, J Exp Clin Cancer Res. 38 (2019) 402. https://doi.org/10.1186/S13046-019-1413-7.

[47] H. Jiang, C. Wang, A. Zhang, Y. Li, J. Li, Z. Li, X. Yang, Y. Hou, ATF4 protects against sorafenib-induced cardiotoxicity by suppressing ferroptosis, Biomed Pharmacother. 153 (2022). https://doi.org/10.1016/J.BIOPHA.2022.113280.

[48] S.B. Cullinan, J.A. Diehl, PERK-dependent activation of Nrf2 contributes to redox homeostasis and cell survival following endoplasmic reticulum stress, J Biol Chem. 279 (2004) 20108–20117. https://doi.org/10.1074/JBC.M314219200.

[49] J.E. Jang, J.I. Eom, H.K. Jeung, H. Chung, Y.R. Kim, J.S. Kim, J.W. Cheong, Y.H. Min, PERK/NRF2 and autophagy form a resistance mechanism against G9a inhibition in leukemia stem cells, J Exp Clin Cancer Res. 39 (2020). https://doi.org/10.1186/S13046-020-01565-3.

[50] X. Zheng, B. Liu, X. Liu, P. Li, P. Zhang, F. Ye, T. Zhao, Y. Kuang, W. Chen, X. Jin, Q. Li, PERK Regulates the Sensitivity of Hepatocellular Carcinoma Cells to High-LET Carbon Ions via either Apoptosis or Ferroptosis., J Cancer. 13 (2022) 669–680. https://doi.org/10.7150/jca.61622.

[51] R. Zhao, Y. Lv, T. Feng, R. Zhang, L. Ge, J. Pan, B. Han, G. Song, L. Wang, ATF6α promotes prostate cancer progression by enhancing PLA2G4A-mediated arachidonic acid metabolism and protecting tumor cells against ferroptosis, Prostate. 82 (2022) 617–629. https://doi.org/10.1002/PROS.24308.

[52] Y.X. Feng, E.S. Sokol, C.A. del Vecchio, S. Sanduja, J.H.L. Claessen, T.A. Proia, D.X. Jin, F. Reinhardt, H.L. Ploegh, Q. Wang, P.B. Gupta, Epithelial-to-mesenchymal transition activates PERK-eIF2α and sensitizes cells to endoplasmic reticulum stress, Cancer Discov. 4 (2014) 702–715. https://doi.org/10.1158/2159-8290.CD-13-0945/42426/AM/EPITHELIAL-TO-MESENCHYMAL-TRANSITION-ACTIVATES.

[53] Y. Mou, J. Wang, J. Wu, D. He, C. Zhang, C. Duan, B. Li, Ferroptosis, a new form of cell death: Opportunities and challenges in cancer, J Hematol Oncol. 12 (2019) 1–16. https://doi.org/10.1186/s13045-019-0720-y.

[54] J.Y. Cao, S.J. Dixon, Mechanisms of ferroptosis, Cellular and Molecular Life Sciences. 73 (2016) 2195–2209. https://doi.org/10.1007/s00018-016-2194-1.

[55] L. Chen, J. He, J. Zhou, Z. Xiao, N. Ding, Y. Duan, W. Li, L.Q. Sun, EIF2A promotes cell survival during paclitaxel treatment in vitro and in vivo, J Cell Mol Med. 23 (2019) 6060–6071. https://doi.org/10.1111/JCMM.14469.

[56] P. Ye, J. Mimura, T. Okada, H. Sato, T. Liu, A. Maruyama, C. Ohyama, K. Itoh, Nrf2- and ATF4-Dependent Upregulation of xCT Modulates the Sensitivity of T24 Bladder Carcinoma Cells to Proteasome Inhibition, Mol Cell Biol. 34 (2014) 3421. https://doi.org/10.1128/MCB.00221-14.

[57] M.E. Torrence, M.R. Macarthur, A.M. Hosios, A.J. Valvezan, J.M. Asara, J.R. Mitchell, B.D. Manning, The mtorc1-mediated activation of atf4 promotes protein and glutathione synthesis downstream of growth signals, Elife. 10 (2021). https://doi.org/10.7554/eLife.63326.

[58] R. Gao, R.K.R. Kalathur, M. Coto-Llerena, C. Ercan, D. Buechel, S. Shuang, S. Piscuoglio, M.T. Dill, F.D. Camargo, G. Christofori, F. Tang, YAP/TAZ and ATF4 drive resistance to Sorafenib in hepatocellular carcinoma by preventing ferroptosis, EMBO Mol Med. 13 (2021). https://doi.org/10.15252/EMMM.202114351.

[59] V. Vichai, K. Kirtikara, Sulforhodamine B colorimetric assay for cytotoxicity screening, Nat Protoc. 1 (2006) 1112–1116. https://doi.org/10.1038/NPROT.2006.179.

[60] S. Maheshwari, S.R. Avula, A. Singh, L.R. Singh, G.R. Palnati, R.K. Arya, S.H. Cheruvu, S. Shahi, T. Sharma, S. Meena, A.K. Singh, R. Kant, M. Riyazuddin, H.K. Bora, M.I. Siddiqi, J.R. Gayen, K. v. Sashidhara, D. Datta, Discovery of a novel small-molecule inhibitor that targets PP2A–β-catenin signaling and restricts tumor growth and metastasis, Mol Cancer Ther. 16 (2017) 1791–1805. https://doi.org/10.1158/1535-7163.MCT-16-0584/86850/AM/DISCOVERY-OF-A-NOVEL-SMALL-MOLECULE-INHIBITOR-THAT.

[61] K. Roy Choudhury, K.J. Yagle, P.E. Swanson, K.A. Krohn, J.G. Rajendran, A Robust Automated Measure of Average Antibody Staining in Immunohistochemistry Images, 58 (2010) 95–107. https://doi.org/10.1369/jhc.2009.953554.

[62] S. Ram, P. Vizcarra, P. Whalen, S. Deng, C.L. Painter, A. Jackson-Fisher, S. Pirie-Shepherd, X. Xia, E.L. Powell, Pixelwise H-score: A novel digital image analysis-based metric to quantify membrane biomarker expression from immunohistochemistry images, PLoS One. 16 (2021) e0245638. https://doi.org/10.1371/JOURNAL.PONE.0245638.

[63] M.J. Goldman, B. Craft, M. Hastie, K. Repečka, F. McDade, A. Kamath, A. Banerjee, Y. Luo, D. Rogers, A.N. Brooks, J. Zhu, D. Haussler, Visualizing and interpreting cancer genomics data via the Xena platform, Nat Biotechnol. 38 (2020) 675–678. https://doi.org/10.1038/S41587-020-0546-8.